University of Alberta

Steady State and Transient Characterization of a HCCI Engine with Varying Octane Fuel

by

Robert Anthony William Lupul

A thesis submitted to the Faculty of Graduate Studies and Research in partial fulfillment of the requirements for the degree of Master of Science.

Department of Mechanical Engineering

Edmonton, Alberta

Spring 2008

Library and Archives Canada

Published Heritage Branch

395 Wellington Street
Ottawa ON K1A 0N4
Canada

Bibliothèque et Archives Canada

Direction du Patrimoine de l'édition

395, rue Wellington
Ottawa ON K1A 0N4
Canada

Your file Votre référence
ISBN: 978-0-494-45850-1
Our file Notre référence
ISBN: 978-0-494-45850-1

NOTICE:
The author has granted a non-exclusive license allowing Library and Archives Canada to reproduce, publish, archive, preserve, conserve, communicate to the public by telecommunication or on the Internet, loan, distribute and sell theses worldwide, for commercial or non-commercial purposes, in microform, paper, electronic and/or any other formats.

The author retains copyright ownership and moral rights in this thesis. Neither the thesis nor substantial extracts from it may be printed or otherwise reproduced without the author's permission.

AVIS:
L'auteur a accordé une licence non exclusive permettant à la Bibliothèque et Archives Canada de reproduire, publier, archiver, sauvegarder, conserver, transmettre au public par télécommunication ou par l'Internet, prêter, distribuer et vendre des thèses partout dans le monde, à des fins commerciales ou autres, sur support microforme, papier, électronique et/ou autres formats.

L'auteur conserve la propriété du droit d'auteur et des droits moraux qui protège cette thèse. Ni la thèse ni des extraits substantiels de celle-ci ne doivent être imprimés ou autrement reproduits sans son autorisation.

In compliance with the Canadian Privacy Act some supporting forms may have been removed from this thesis.

While these forms may be included in the document page count, their removal does not represent any loss of content from the thesis.

Conformément à la loi canadienne sur la protection de la vie privée, quelques formulaires secondaires ont été enlevés de cette thèse.

Bien que ces formulaires aient inclus dans la pagination, il n'y aura aucun contenu manquant.

Canada

University of Alberta

Library Release Form

Name of Author: Robert Anthony William Lupul

Title of Thesis: Steady State and Transient Characterization of a HCCI Engine with Varying Octane Fuel

Degree: Master of Science

Year this Degree Granted: 2008

Permission is hereby granted to the University of Alberta to reproduce single copies of this thesis and to lend or sell such copies for private, scholarly, or scientific research purposes only.

The author reserves all other publication and other rights in association with the copyright in the thesis, and except as hereinbefore provided, neither the thesis nor any substantial portion thereof may be printed or otherwise reproduced in any material form whatever without the author's prior written permission.

Robert Anthony William Lupul

University of Alberta

Faculty of Graduate Studies and Research

The undersigned certify that they have read, and recommend to the Faculty of Graduate Studies and Research for acceptance, a thesis entitled Steady State and Transient Characterization of a HCCI Engine with Varying Octane Fuel submitted by Robert Anthony William Lupul in partial fulfillment of the requirements for the degree of Master of Science.

Dr. C.R. (Bob) Koch (Advisor)

Dr. R.E. Hayes

Dr. M. David Checkel

Dr. M.G. Lipsett

Abstract

An experimental investigation of Homogenous Charge Compression Ignition (HCCI) on a port fuel injected single cylinder engine equipped with two separate fuel systems is performed in steady state and load transient conditions. A range of intake air temperatures, intake manifold pressures, and engine speeds, are investigated using two fuel systems to separately supply n-heptane and iso-octane. Results show the ability of the two fuels to obtain the load range at a given operating condition with constant combustion timing. The ability to transition from Spark Ignition (SI) mode to HCCI mode (and vice versa) within consecutive cycles using the two fuel system is also shown for cases of constant load as well as constant intake manifold pressure. HCCI engine operation has comparable carbon monoxide and unburned hydrocarbon emissions with lowered fuel consumption and dramatically reduced NO_x production compared to SI mode.

Acknowledgements

I wish to thank my supervisor, Dr. Bob Koch, for his encouragement, guidance, patience and financial support.

Thanks are also due to the Mechanical Engineering machinist/technicians, Bernie Faulkner, Greg Miller, Dave Waege, Ian Buttar, Dave Pape, Rick Bubenko and Terry Nord for their expert skills and advice. Special thanks is due to Bernie Faulkner. His help with the experimental setup was a significant part of my education. Thanks to my colleagues in Room 4-28.

Finally I would like to thank my parents, Gary and Rose. Their support for my endeavors has always seemed limitless.

Table of Contents

1 Introduction **1**

1.1 Organization of Thesis 3

2 Background **5**

2.1 Fundamentals of HCCI 5

2.2 Comparison of HCCI with Conventional SI and CI 9

2.3 Effects of Engine Operating Condition on HCCI 10

2.4 HCCI-SI Mode Switching 13

3 Experimental Setup **16**

3.1 Ricardo Single Cylinder Engine 16

3.2 Data Acquisition System 23

3.3 Combustion Analysis System 25

3.4 Emissions Bench 27

4 Experimental Procedure **29**

4.1 Research Fuels 29

4.2 Operating Region Definition 30

4.3 Test Procedures and Matrix of Test Points 31

4.4 Cylinder Pressure Analysis 40

4.4.1 Cylinder Pressure Signal Filter 40

4.4.2 Engine Cycle Analysis from In-cylinder Pressure 46
4.4.3 Intake Stroke 47
4.4.4 Closed Engine Cycle 47
4.4.5 Exhaust Stroke and Residual Estimation 50
4.4.6 Uncertainty in Analysis 56

5 Experimental Results **60**
5.1 Experimental Uncertainty 60
5.2 Determination of Optimum Combustion Timing 67
5.3 Steady State Results 71
5.3.1 HCCI Load Range 71
5.3.2 Fueling Required for HCCI 73
5.3.3 Estimated Temperature Parameters 85
5.3.4 Brake Specific Emissions and Fuel Consumption 93
5.3.5 HCCI Knock 103
5.4 Transient Results 112
5.5 HCCI to SI Mode Transitions 122
5.5.1 Mode Transitions at Constant MAP 125
5.5.2 SI-HCCI Mode Transitions at Constant Load 127

6 Conclusion **142**
6.1 Conclusions 142
6.2 Future Work 145

Bibliography **147**

A Experimental Data Summary **156**
A.1 HCCI Combustion Timing Test Data 156
A.2 HCCI Steady State Data 158

A.3 HCCI Repeated Trials Data 162
A.4 HCCI Transient Results 166
A.5 Spark Ignition Experimental Data 176

B Experimental Equipment Setup **179**

B.1 Emissions Calculations 179
B.2 Equipment Calibration 181
B.2.1 Determining TDC Offset 181
B.2.2 Fuel Injector Flow Rate Calibration 183
B.2.3 Laminar Air Flow Meter Calibration 185
B.3 Data Collection and Analysis Programs 187
B.3.1 Baseline ADAPT, Baseline CAS, and MicroAutobox Programs 187
B.3.2 Data Analysis Programs 192
B.4 List of Equipment Used 193

List of Tables

3.1 General dimensions of the Ricardo Hydra Engine 17

3.2 ADAPT Baseline DAC Specifications 24

3.3 Emissions Bench Analyzers and Measurement Ranges 28

4.1 Fuel Properties [Owen and Coley, 1990] 30

4.2 Engine Operating Points for Combustion Timing Tests 34

4.3 Engine Operating Points for Steady State Tests 36

4.4 Engine Operating Points for Repeated Trials of Steady State Tests . . 37

4.5 Engine Operating Points for Transient Step and Pulse Tests 39

4.6 Engine Operating Points for Mode Switching tests 40

4.7 Summary of Measured Inputs and Estimated Uncertainty. Parameters with a '*' are estimated. 57

4.8 Summary of Input Error on Analyzed Results. Nominal values are the average of Tests SS16, SS17, and SS18. 59

5.1 Average and Standard Deviation (in brackets) of 5 Repeated Trials for Case N of Table 4.4. 61

5.2 Average and Standard Deviation (in brackets) of 5 Repeated Trials for Case O of Table 4.4. 62

5.3 Average and Standard Deviation (in brackets) of 5 Repeated Trials for Case P of Table 4.4. 63

5.4 Average and Standard Deviation (in brackets) of 5 Repeated Trials for Case Q of Table 4.4. 64

5.5 Average and Standard Deviation (in brackets) of 5 Repeated Trials for Case R of Table 4.4. 65

5.6 Average and Maximum Standard Deviations of Performance Metrics for all Repeated Trials 66

A.4 Operating Conditions for Spark Ignition Engine Tests 176

B.1 PC and RTP Files for Running Engine and Collecting Data 187

B.2 Matlab Files for Post Processing Data and Generating Plots 192

B.3 Instrumentation List 194

B.4 Equipment List 194

List of Figures

1.1 The HCCI Cycle 2

3.1 Schematic of Ricardo Single Cylinder Engine Experimental Setup - sensors, actuators, and data acquisition systems not shown 22

3.2 Schematic of Variables Captured with Data Acquisition 22

3.3 Schematic of Available Actuators 23

4.1 Mode Shapes and Estimated Mode Numbers 42

4.2 Raw and Filtered Pressure Traces for Full Cycle. Test SS27 cycle 155. 43

4.3 Raw and Filtered Pressure Traces Near Combustion Region. Test SS27 cycle 155. 44

4.4 Frequency Spectrum of Cylinder Pressure Trace After Applying High Pass Filter Complementary to Low Pass. Test SS27 cycle 155. 45

4.5 Estimated Exhaust Gas Temperature vs. Measured Exhaust Gas Temperature of Tests SS1-SS75 52

4.6 Cylinder Pressure for Three Loads with Ten Cycles for each Load. Cycles 1-10 of tests SS58-SS60. 53

4.7 Heat Release Rate for Three Loads with Ten Cycles for each Load. Cycles 1-10 of tests SS58-SS60. 54

4.8 Typical Heat Release profile 55

5.1 Effect of Intake Temperature on SOC for Cases A, B, and C in Table 4.2 67

5.2 Effect of average SOC on Combustion Pressure Rise Rate for Cases A, B and C in Table 4.2 68
5.3 Effect of SOC on IMEP for Cases A, B, and C in Table 4.2 70
5.4 IMEP vs BMEP for Cases D, E, F, G, and H of Table 4.3 72
5.5 Load Range in terms of IMEP vs T_{int} for three values of MAP at 1000rpm. Minimum and maximum load limits shown for Cases D, E and F of Table 4.3 74
5.6 Load Range in terms of IMEP vs T_{int} for three values of engine speed with MAP of 125kPa. Minimum and maximum load limits shown for Cases E, G and H of Table 4.3 75
5.7 ON for Minimum and Maximum Load for Different Engine Speed vs. T_{int} with MAP=125kPa. Cases E, G and H of Table 4.3. Dashed lines indicate minimum load cases and dotted lines maximum load cases. . 76
5.8 ON for Minimum and Maximum Load for Different MAP vs. T_{int} with N=1000rpm. Cases D, E and F of Table 4.3. Dashed lines indicate minimum load cases and dotted lines maximum load cases. 77
5.9 HR_{LTR} vs. Heptane Mass per Cycle for Three MAP 79
5.10 HR_{LTR} vs. Heptane Mass per Cycle for Three Engine Speeds 80
5.11 HR_{LTR} normalized for changes in MAP and N. Cases D-H of Table 4.3. 82
5.12 HR_{LTR} vs. T_{int} for Three MAP at N-1000rpm. Cases D, E and F of Table 4.3. Dashed lines indicate minimum load cases and dotted lines maximum load cases. 83
5.13 HR_{LTR} vs. T_{int} for Three Engine Speeds for MAP=125kPa. Cases E, G and H of Table 4.3. Dashed lines indicate minimum load cases and dotted lines maximum load cases. 84

5.14 T_{IVC} vs. T_{int} for three value of MAP at N=1000rpm. Cases D, E and F of Table 4.3. Dashed lines indicate minimum load cases and dotted lines maximum load cases. 87

5.15 T_{IVC} vs. T_{int} for three Engine Speeds at MAP=125kPa. Cases E, G and H of Table 4.3. Dashed lines indicate minimum load cases and dotted lines maximum load cases. 88

5.16 Estimated Convective Heat Transfer Coefficient in the intake port vs T_{int}. Cases D-H of Table 4.3. 89

5.17 T_{max} vs. T_{int} for three value of MAP for N=1000rpm. Cases D, E and F of Table 4.3. Dashed lines indicate minimum load cases and dotted lines maximum load cases. 90

5.18 T_{max} vs. T_{int} for three Engine Speeds for MAP=125kPa. Cases E, G and H of Table 4.3. Dashed lines indicate minimum load cases and dotted lines maximum load cases. 91

5.19 T_{max} vs. λ for Cases D, E, F, G, and H of Table 4.3 92

5.20 Brake Specific CO Emissions vs. T_{max} for Cases D, E, F, G, and H of Table 4.3 94

5.21 Brake Specific CO Emissions vs. λ for Cases D, E, F, G, and H of Table 4.3 95

5.22 Brake Specific UHC Emissions vs. T_{max} for Cases D, E, F, G, and H of Table 4.3 96

5.23 Brake Specific UHC Emissions vs. λ for Cases D, E, F, G, and H of Table 4.3 97

5.24 Brake Specific NO_x Emissions vs. T_{max} for Cases D, E, F, G, and H of Table 4.3 98

5.25 Brake Specific NO_x Emissions vs. λ for Cases D, E, F, G, and H of Table 4.3 99

5.26 BSFC vs. BMEP for Cases D, E, F, G, and H of Table 4.3 100
5.27 BSFC vs. BMEP for SI and HCCI 101
5.28 BSCO vs. BMEP for SI and HCCI 102
5.29 BSUHC vs. BMEP for SI and HCCI 102
5.30 $\frac{\Delta P}{\Delta \theta}$ vs. λ for different MAP at N=1000rpm. Cases D, E and F of Table 4.3 105
5.31 $\frac{\Delta P}{\Delta \theta}$ vs. λ for different Engine Speed, MAP=125kPa. Cases E, G and H of Table 4.3 106
5.32 $\frac{\Delta P}{\Delta \theta}$ time vs. λ for different MAP at N=1000rpm. Cases E, G and H of Table 4.3 107
5.33 $\frac{\Delta P}{\Delta \theta}$ vs. λ for different MAP at N=1000rpm. Cases D-H of Table 4.3 . 108
5.34 Raw Signal from Knock Sensor with In-cylinder Pressure. Test SS27 cycle 155. 109
5.35 Estimated Power Spectral Density of Knock Trace. Test SS27 cycle 155. 110
5.36 Knock Intensity vs. Combustion Pressure Rise Rate. Test Cases D-H. 110
5.37 Knock Intensity vs. Burn Duration. Test Cases D-H. 111
5.38 Knocking Frequency vs. T_{max}. Test Cases D-H. 111
5.39 Combustion Metrics Through a Step Load Transient. Test Cases TR33 and TR34. 116
5.40 Close Up of Figure 5.39. Combustion Metrics Through a Step Load Transient. Test Cases TR33 and TR34. 117
5.41 Perturbation of Iso-octane Fueling in SI Mode 118
5.42 Combustion Metrics Through a Pulse Load Transient. Test points TR59 and TR60. 119
5.43 Combustion Metrics Through a Pulse Load Transient. Test points TR59 and TR60. 120

5.44 Combustion Metrics Through a Pulse Load Transient. Test points TR59 and TR60. 121
5.45 Lookup table of mass of n-heptane required as a function of T_{int} and MAP for HCCI combustion with $CA5_{HTR}$ of 7 CAD aTDC. Tests SS1-SS45. 123
5.46 HCCI-SI Mode Switching with Constant MAP. Test MS8. 132
5.47 Close up of HCCI-SI Mode Switching with Constant MAP. Test MS8. 133
5.48 Last HCCI Cycle and First SI Cycle During a Mode Switch. Test MS8. 134
5.49 Last SI Cycle and First HCCI Cycle During a Mode Switch. Test MS8. 134
5.50 Simulink Block Diagram of HCCI to SI Switching Logic 135
5.51 HCCI-SI Mode Switch with Similar Steady State Loads, HCCI MAP 100kPa. Test MS3. 136
5.52 Close Up of HCCI-SI Mode Switch with Similar Steady State Loads, HCCI MAP 100kPa. Test MS3. 137
5.53 HCCI-SI Mode Switch with Similar Steady State Loads, HCCI MAP 115kPa. Test MS7. 138
5.54 Close Up of HCCI-SI Mode Switch with Similar Steady State Loads, HCCI MAP 115kPa. Test MS7. 139
5.55 HCCI-SI Mode Switch with Similar Steady State Loads, HCCI MAP 120kPa. Test MS4. 140
5.56 Close Up of HCCI-SI Mode Switch with Similar Steady State Loads, HCCI MAP 120kPa. Test MS4. 141

A.1 Combustion Metrics Through a Step Load Transient. Tests TR17 and TR18. 167
A.2 Combustion Metrics Through a Step Load Transient. Tests TR49 and TR50. 168

A.3 Combustion Metrics Through a Step Load Transient. Tests TR57 andTR58. 169
A.4 Combustion Metrics Through a Step Load Transient. Tests TR77 and TR78. 170
A.5 Combustion Metrics Through a Step Load Transient. Tests TR93 and TR94. 171
A.6 Combustion Metrics Through a Pulse Load Transient. Tests TR19 and TR20. 172
A.7 Combustion Metrics Through a Pulse Load Transient. Tests TR39 and TR40. 173
A.8 Combustion Metrics Through a Pulse Load Transient. Tests TR89 and TR90. 174
A.9 Combustion Metrics Through a Pulse Load Transient. Tests TR95 and TR96. 175

B.1 Comparison of Lambda Calculated by UEGO and by Emissions Bench 181
B.2 Raw Data Collected from Oscilloscope from Motored Engine 182
B.3 Octane Fuel Injector Pulse Width vs. Injected Octane Mass per Cycle 184
B.4 Heptane Fuel Injector Pulse Width vs. Injected Heptane Mass per Cycle184
B.5 Air Volume Flow Rate vs. Differential Pressure Across Laminar Flow Element 185
B.6 Error in Linear Fit of Volume Flow Rate Compared with Actual Data vs. Differential Pressure 186
B.7 Screenshot of the ADAPT Software Layout 188
B.8 Screenshot of the CAS Software Layout 188
B.9 Screenshot of Simulink Block Diagram of ECU Software 189
B.10 Screenshot of the dSpace Controldesk Layout 189

B.11 Measured Value of λ vs. Crankshaft Angle for 450 cycles. Test SS54 . 190
B.12 Measured Value of MAP vs. Crankshaft Angle for 450 cycles. Test SS54190
B.13 Measured Value of In-cylinder Pressure vs. Crankshaft Angle for 450 cycles. Test SS54 191
B.14 Measured Value of In-cylinder Pressure near combustion vs. Crankshaft Angle for 450 cycles. Test SS54 191

NOMENCLATURE

Acronyms

AFR	Air to Fuel Ratio on mass basis
BDC	Bottom Dead Centre
BMEP	Brake Mean Effective Pressure [kPa]
BD	Burn Duration
CAS	Combustion Analysis System
CAD	Crankshaft Angle Degree
CI	Compression Ignition
CO	Carbon Monoxide
COV_{IMEP}	Coefficient of Variance in IMEP
ECU	Engine Control Unit
EGR	Exhaust Gas Recirculation
EVC	Exhaust Valve Closing angle
EVO	Exhaust Valve Opening angle

FMEP ..... Friction Mean Effective Pressure [kPa]

HCCI ..... Homogenous Charge Compression Ignition

HR ..... Heat Release [kJ]

HTR ..... High Temperature Reaction

IMEP ..... Indicated Mean Effective Pressure [kPa]

IVC ..... Intake Valve Closing angle

IVO ..... Intake Valve Opening angle

LHV ..... Lower Heating Value [kJ/kg]

LTR ..... Low Temperature Reaction

MAP ..... intake Manifold Absolute Pressure [kPa]

MFB ..... Mass Fraction Burnt

NO ..... Nitric Oxide

NO_x ..... Oxides of Nitrogen

ON ..... Octane Number

PRF ..... Primary Reference Fuel

PSD ..... Power Spectral Density

PW ..... Pulse Width [msec]

RPM ..... Revolution Per Minute

SI ..... Spark Ignition

SOC ..... Start Of Combustion

TDC ..... Top Dead Centre (prefix 'a' for after TDC, 'b' for before TDC)

UEGO ..... Universal Exhaust Gas Oxygen (sensor)

UHC ..... Unburned Hydrocarbons

WOT ..... Wide Open Throttle

Symbols

λ ..... Lambda ($\lambda = \frac{AFR_{actual}}{AFR_{stoich}}$)

θ ..... Crankshaft angle [deg]

$f_{m,n}$ ..... Frequency associated with mode (m,n) [Hz]

$\rho_{m,n}$ ..... Mode number associated with mode (m,n)

B ..... Cylinder Bore [mm]

r ..... Crankshaft throw ($r = Stroke/2$) [mm]

P ..... In-cylinder pressure [kPa]

V ..... Cylinder volume [mm^3]

K_f ..... Fuel Injector Flow Rate Constant [sec/g]

K_{offset} ..... Fuel Injector Opening Time Constant [sec]

K_{int} ..... Knock Intensity [V]

L ..... Connecting rod length [mm]

x ..... Piston wrist pin offset [mm]

T ..... Brake Torque [Nm]

T ..... In-cylinder Temperature [K]

HR ..... Cumulative heat released [kJ]

N ..... Engine speed [rpm]

V_{octane} ..... Volume of iso-octane [L]

$V_{heptane}$ ..... Volume of n-heptane [L]

$PW_{heptane}$ ..... Fuel injector pulse width of n-heptane [sec]

PW_{octane} ..... Fuel injector pulse width of iso-octane [sec]

P_{Brake} ..... Brake power [kW]

Cp ..... Constant pressure specific heat [kJ/kgK]

f_r ..... Residual fraction

γ ..... Polytropic index

m ..... In-cylinder mass per cycle [mg]

$\dot{m}$ ..... Mass flow rate [g/sec]

R ..... Ideal Gas Constant, 0.287kJ/kgK

Q_{HR} ..... Energy of chemical heat released [kJ]

Q_{HL} ..... Energy of heat lost [kJ]

$Q_{HR_{net}}$ ..... Net chemical energy released [kJ]

VE ..... Volumetric Efficiency

Subscripts

air	Of the fresh air entering the engine
octane	Of the iso-octane fuel
heptane	Of the n-heptane fuel
int	At the intake manifold condition
cyl	Of the engine cylinder
stoich	At a stoichiometric AFR
res	Estimated property of the exhaust residual
IVC	At the instant of IVC
exh	At the exhaust condition
LTR	Total during the LTR phase of combustion
HTR	Total during the HTR phase of combustion
max	Maximum during the closed part of the cycle

Chapter 1

Introduction

The most significant prime mover for the past century is the internal combustion (IC) engine. These engines have shaped our cities and countries and directly altered our way of life through the automobile. With the explosive growth in the number of IC engines has also come a likewise growth in the by-product emissions produced. Legislation regulating the emissions produced by automobiles has led to increasingly sophisticated engine control and after-treatment devices to meet these regulations. While, for the long term, alternative powertrain choices may be developed, in the near term, the IC engine is likely to remain the main propulsion system of choice [MacLean and Lave, 2003].

One promising potential technology for reduced fuel consumption and lower emissions is Homogenous Charge Compression Ignition (HCCI) combustion. HCCI uses a homogenous charge preparation with compression ignition to fundamentally change the combustion process compared to traditional spark ignition (SI) or compression ignition (CI) engines. The combustion process is where HCCI differs from SI or CI. SI engines use a prepared homogenous mixture and a spark to initiate combustion via a flame front, whereas CI engines use timed injection of fuel into the cylinder to initiate a diffusion flame. In this way HCCI is a combination of SI and CI attributes, using a homogeneous charge, and compression ignition.

The HCCI combustion process has been given several different names, including: Pre-mixed Charge Compression Ignition (PCCI), Controlled Auto-Ignition (CAI), and active radical combustion. The same fundamental combustion process is behind each different nomenclature.

HCCI engines operate on the same fundamental 4 stroke cycle as both conventional SI and CI engines. This process is shown in Figure 1. The intake stroke is used to introduce fresh air and fuel into the cylinder and mix the two into a homogenous mixture. The compression stroke begins the closed part of the cycle at the instant of IVC. At IVC the mixture begins its compression by the piston, increasing it's temperature and pressure. As the piston approaches Top Dead Center (TDC) the mixture properties near the auto-ignition point of the mixture. As the auto-ignition point is reached, the fuel is oxidized releasing it's stored chemical energy. As the fuel oxidizes the mixture temperature and pressure increases. During the expansion stroke work is done on the piston, producing a net positive torque on the crankshaft. The cycle is completed by the piston ascending on the exhaust stroke, forcing the products of combustion out of the cylinder.

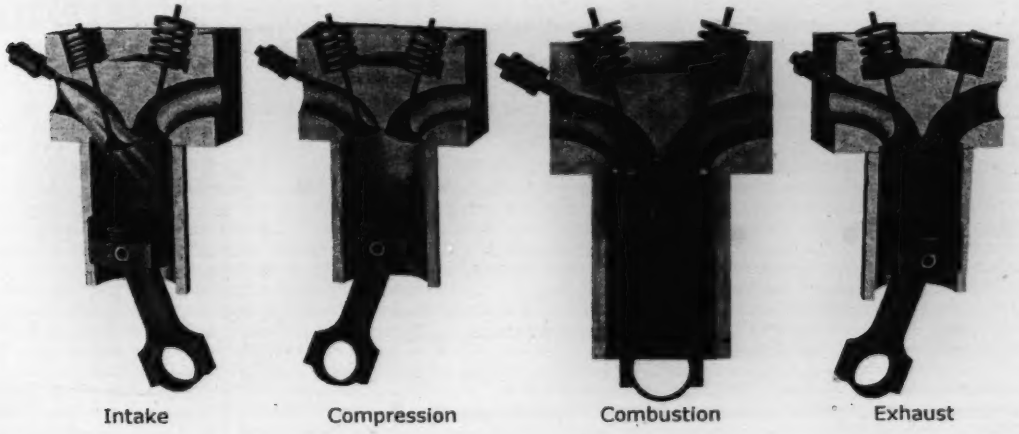

Figure 1.1: The HCCI Cycle

The most significant challenge of HCCI is the lack of a direct means to initiate the combustion process, like the spark in SI engines, or the timed injection of fuel in CI engines. A requirement of HCCI is to create the conditions necessary near TDC of the compression stroke to reliably cause this auto-ignition process to occur with the correct timing.

The goal of this thesis is to provide experimental data to aid in understanding of the HCCI process. Experimental data provides valuable information on the actual natural processes of HCCI. In this work, the steady state operating region for which stable HCCI can be obtained, is examined. The fuel consumption, emissions, and knock characteristics of HCCI are presented. Using dual fuel actuation, load transients are also performed to investigate the potential of this technique. Finally, the dual fuel system is used to show the possibility of performing transitions from HCCI to SI combustion. Knowledge of the actual phenomena also provides data to be used in further investigations by subsequent researchers for validation of numerical models.

1.1 Organization of Thesis

In Chapter 2 a review of the fundamentals of HCCI combustion is presented, and a review of the work of other researchers in the area of HCCI is presented. A comparison of HCCI with traditional SI and CI engines is presented, along with the influences of significant engine parameters on HCCI. The potential for switching between SI and HCCI combustion modes is also presented. Chapter 3 provides a detailed description of the experimental setup used in this thesis. The major mechanical systems of the engine test bed are described, along with the computerized test bed control and data acquisition systems. In Chapter 4 the definition of the stable HCCI operating region is defined. The procedure for collecting data is described for the steady state, transient, and SI-HCCI mode switching tests. The methods for post processing analysis

of the data are included, along with an uncertainty analysis of the post processing techniques. In Chapter 5 the experimental results are presented along with a discussion of the results. Steady state tests, transient tests, and SI-HCCI mode switching tests are all shown. Repeated trials of several experiments are also presented to show the repeatability of the apparatus. Finally, in Chapter 6 conclusions of this work are drawn and possibilities for future work are discussed.

Chapter 2

Background

To realize the potential benefits HCCI combustion offers, an understanding of the fundamental characteristics of HCCI is important. A range of experimental and simulation testing has been done by several researchers. In this chapter, a brief overview of the auto-ignition process that is the basis of HCCI is covered. A review of the important engine operating parameters, and their effects on HCCI is discussed, and finally there is an introduction to SI-HCCI mode switching.

2.1 Fundamentals of HCCI

As originally found in [Najt and Foster, 1983], HCCI is initiated and the combustion progression dominated by the chemical kinetics of the mixture. These kinetic mechanisms result in extremely fast combustion events unless adequately diluted through additional gas supplied to the combustion chamber. To increase the combustion duration to a range suitable for IC engines, either air and/or Exhaust Gas Recirculation (EGR) diluted mixtures must be used. Air-diluted HCCI (as investigated in this thesis) uses excess air to dilute the in-cylinder mixture similar to traditional CI engines. A summary of several air-diluted HCCI engines is shown by [Hyvonen et al., 2006]. EGR dilution can be done by either externally routing EGR into the intake tract [Atkins, 2004], or by using valve timing to maintain additional residual fraction within

the cylinder for the next cycle. This can be done by early closing of the exhaust valve, a process called negative valve overlap, or by opening the exhaust valve a second time during the intake stroke [Babajimopoulos et al., 2003]. Both of these processes are generally termed internal EGR strategies. Using a fully flexible valvetrain, either of these two internal EGR strategies may be more beneficial depending on the operating condition [Kulzer et al., 2007].

Irrespective of the method used to achieve HCCI operation of the engine, a similar auto-ignition process dominates the combustion event. The chemical kinetic mechanisms which are responsible for the auto-ignition process consist of potentially hundreds of reactions, not all of which are fully understood [Turns, 2000].

Fuels tend to exhibit one of two characteristic modes of auto-ignition. The first is a single stage reaction, where all of the fuel is oxidized in a single combustion event. The other mode is a two stage combustion event, with a low temperature reaction (LTR) region of combustion, and a High Temperature Reaction (HTR) region.

Depending on the objectives, several types of simulation models have been developed. Skeletal models [Kirchen et al., 2007, Kongsereeparp and Checkel, 2007], are useful for parameter studies, since only a reduced number of reactions in a single zone are used. For the purposes of realtime control very simple models are needed in order that they can be calculated in realtime [Shahbakhti et al., 2007c]. A simplified hydrocarbon oxidation scheme is presented in [Heywood, 1988]. A similar scheme by Tanaka et al. [Tanaka et al., 2003a, Tanaka et al., 2003b] is summarized here. The base fuel molecule is denoted by RH; in the case of this work, n-heptane or iso-octane.

Conceptual Chemical Kinetic Reaction Mechanism

$$RH + O_2 \rightarrow \dot{R} + H\dot{O}_2 \quad (R1)$$

$$R + O_2 \rightarrow RO_2 \quad (R2)$$

$$RH + O_2 \rightarrow H_2O + OROOH \quad (R3)$$

$$R + O_2 \rightarrow olefin + HO_2 \quad (R4)$$

$$H\dot{O}_2 + HO_2 \rightarrow H_2O_2 + O_2 \quad (R5)$$

$$(M) + H_2O_2 \rightarrow OH + OH + (M) \quad (R6)$$

$$OROOH + olefin \rightarrow H_2O + CO \quad (R7)$$

The oxidation of the hydrocarbon begins with reaction $R1$ where a free hydrogen is abstracted by the O_2 to form an alkyl radical and $H\dot{O}_2$. Reaction $R1$ is slow, and accounts for the long induction time (or ignition delay) typical of long chain hydrocarbon combustion. At low temperatures, reaction $R2$ produces a peroxy alkyl radical. These two reactions initiate a series of reactions, summarized as $R3$. This highly exothermic stage is responsible for the LTR heat release which is prevalent for some fuels, such as n-heptane. This LTR cycle continues until the temperature increases sufficiently where competing reaction $R4$ dominates, thus terminating the first stage of combustion. Reaction $R4$ generates HO_2 for supplying reaction $R5$, where hydrogen peroxide is produced. As the temperature increases above approximately $500°C$, reaction $R6$ decomposes the hydrogen peroxide into two hydroxyl radicals [Heywood, 1988]. This chain branching reaction leads to the thermal explosion phase of combustion leading to reaction $R7$, which produces the products of

combustion, water and carbon monoxide. The carbon monoxide is finally oxidized by the relatively slow CO oxidation kinetics to complete the combustion, [Turns, 2000].

For a given set of these engine operating parameters, intake temperature (T_{int}), intake Manifold Absolute Pressure (MAP), and engine speed (N), there exists a finite range of fueling (fuel quantity and ignition quality) for which stable HCCI exists. At one operating condition there exists both a lean and a rich limit to HCCI combustion. The lean limit is normally defined by the onset of misfires [Oakley et al., 2001], unstable combustion, or zero brake torque (idle) [Hyvonen et al., 2003]. At the rich limit, pressure oscillations occur, similar to knock in an SI engine [Tsurushima et al., 2002]. This knock is undesirable from an Noise Vibration and Harshness (NVH) perspective [Atkins, 2004, Andreae et al., 2007], and could potentially lead to the damage associated with knock in SI engines [Heywood, 1988]. The goal of this work is to look at operating characteristics within the viable operating range between the misfire and knock limits.

With the blended fuel capability of the experimental setup, the fueling is dependant on both the total fuel quantity (in terms of total Lower Heating Value, LHV) as well as the ignition quality of the fuel [Olsson et al., 2001]. The total fuel quantity, along with the mass of air induced into the cylinder, are related to the measured value of λ , while the ignition quality is related to the relative proportions of n-heptane and iso-octane injected, defining the Octane Number (ON).

For a constant ON , reducing the injected fuel quantity results in retarded ignition timing as well as reduced heat release during combustion, which in turn reduces the load of the engine. In the extreme, the reduction in fuel results in ignition timing so late in the cycle that little heat is liberated from the mixture before the descending piston "freezes" the mixture composition. This phenomenon is generally termed a misfire. With normal cycle to cycle variations in the mixture properties, cycles with slightly reduced injected fuel quantity result in misfires as the lean limit is approached.

2.2 Comparison of HCCI with Conventional SI and CI

Compared with traditional nominally stoichiometric SI engines, HCCI engines can improve part load fuel economy by reducing the pumping losses incurred during throttling of the intake air [Kulzer et al., 2007]. This throttling significantly reduces the thermal efficiency of the SI engine, but is necessary to maintain the stoichiometric mixture necessary for a modern three-way catalyst to efficiently operate. Due to the exceptionally low NO_x emissions produced by HCCI combustion, after-treatment to reduce the NO_x is often not necessary except possibly near the high load limit [Cairns and Blaxill, 2007]. Thus HCCI can be run lean of stoichiometric, preserving the carbon monoxide and hydrocarbon oxidation ability of the three-way catalyst, allowing the engine to run un-throttled for a part load condition, improving the engine thermal efficiency.

While HCCI and CI engines share similar benefits over SI engines, including the ability to run un-throttled with high compression ratios, HCCI also enjoys some potential benefits over conventional CI. Since HCCI uses a homogenous mixture, the combustion occurs at a temperature near the average cylinder temperature, while for CI the diffusion flame occurs in regions of near stoichiometric mixture. Thus for CI the combustion occurs at a much higher temperature, increasing the generation of thermal NO_x. Combustion which occurs at the location of a lean mixture (such as HCCI), and thus reducing the peak combustion temperatures, is one method to reduce the thermal production of NO_x. The diffusion flame in CI engines also lends itself to producing particulate emissions, which are typically insignificant in homogenous combustion [Turns, 2000, Stone, 1999].

2.3 Effects of Engine Operating Condition on HCCI

Changes in engine operating condition (T_{int}, MAP, N, EGR, and λ and ON) all influence HCCI combustion. Since the auto-igntion process is dependent on the in-cylinder mixture composition and thermodynamic state, changing each of the operating parameters has a different effect on the combustion.

The fundamental reactions governing the auto-ignition process ($R1 - R7$) are highly dependent on the temperature [Turns, 2000]. By changing the mixture temperature at Intake Valve Closing (IVC), the temperature throughout the compression process is affected. Increasing the mixture temperature at IVC is most easily done by increasing T_{int}. Electrical heating, as done by several researchers [Atkins, 2004, Oakley et al., 2001], as well as exhaust heat recovery [Martinez-Frias et al., 2000, Haraldsson et al., 2004, Iverson et al., 2005], have been used successfully in varying the value of T_{int}. Increasing T_{int} has the ability to advance the combustion timing for an otherwise fixed mixture condition, [Iverson et al., 2005], as the auto-ignition reactions reach the thermal runaway temperature for auto-ignition earlier in the engine cycle.

Along with the direct thermal effect of the value of T_{int} on HCCI combustion, the effect of thermal stratification within the chamber can also play a significant role in the combustion progression. [Sjoberg et al., 2004, Sjoberg et al., 2005] show that the thermal stratification of the in-cylinder mixture has a significant effect on the combustion duration. The thermal gradient within the combustion chamber results from a combination of heat transfer to the cylinder walls during the intake and compression strokes, as well as the magnification of any mixing-related gradient present at IVC by the compression process [Sjoberg et al., 2004]. The thermal gradient within the chamber can also be influenced with the combustion chamber shape by the in-cylinder turbulence generated [Aceves et al., 2005]. Lowering the coolant temperature influ-

ences the thermal stratification by increasing the heat transfer of the in-cylinder mixture to the cylinder walls, [Chang et al., 2005, Sjoberg et al., 2004]. Increasing the thermal gradient within the chamber has the effect of prolonging the combustion duration, as the cooler zones take longer to auto-ignite compared with the relatively hot zones. By increasing the combustion duration sufficiently, the knocking limit of HCCI can be delayed and the effective range of HCCI increased. Using an experimentally validated multi-zone model [Sjoberg et al., 2004] show that increasing the temperature gradient across the cylinder at the start of the compression stroke from 20K to 30K could increase the maximum load by approximately 30% before the onset of knock.

Increasing MAP by supercharging or turbocharging is used to extend the HCCI high load operating range compared to naturally aspirated operation. Both supercharging and turbocharging increase the maximum load obtainable with HCCI in a variable compression ratio engine of typical automotive dimensions with no EGR, [Hyvonen et al., 2003]. The turbocharged version of this engine experiences better brake efficiency compared to the supercharged variation due to the reduction in parasitic losses. A maximum Brake Mean Effective Pressure (BMEP) of 10 bar is achieved by Hyvonen et al. at low engine speeds, which is comparable to the maximum output of a typical SI naturally aspirated engine. Even with the losses of the turbocharger accounted for, Hyvonen et al. show that the engine experiences higher brake thermal efficiency in HCCI mode compared with SI mode. Similar results are reported with an engine equipped with manually variable low lift and duration camshafts designed for HCCI operation [Yap et al., 2005a, Yap et al., 2005b, Xu et al., 2007]. The low lift camshafts are used to keep a large residual fraction within the cylinder to increase the mixture temperature using the hot residual. For a fixed camshaft timing an increase in the Indicated Mean Effective Pressure (IMEP) from 4bar to 7bar is obtainable by increasing the boost pressure from 0.2bar to 1.2bar

[Yap et al., 2005b].

Since the HCCI auto-ignition process is a time-based process, changes in engine speed must be compensated for with changes to the engine operating condition in order to maintain a constant combustion timing. The effect of engine speed on a Diesel engine of 18:1 compression ratio, converted to HCCI operation is shown in [Sjoberg and Dec, 2003, Sjoberg and Dec, 2007]. For each series of tests the value of T_{int} is adjusted to maintain CA50 (see Section Eqn. 4.14 for definition) at TDC [Sjoberg and Dec, 2003]. The type of fuel used has a significant effect on the engine speed sensitivity of combustion. Namely Primary Reference Fuel (PRF) with ON of 60 and 80 were found to require a much larger change in T_{int} with changes in N due to the LTR present with these fuels, compared pure iso-octane which exhibits a single stage combustion. The Heat Release (HR) in the LTR region (HR_{LTR}) increased significantly at engine speeds from 600-1800rpm, requiring a decrease in T_{int} to maintain the combustion timing. By changing the MAP the magnitude of the HR_{LTR} could be adjusted [Sjoberg and Dec, 2007]. Thus to maintain a constant combustion timing for fuels that exhibit a LTR region, coordination of managing T_{int}, MAP, and λ is required.

Using EGR to dilute the in-cylinder mixture can be achieved by using external EGR [Atkins, 2004], internal EGR [Kulzer et al., 2007], or a combination of the two [Cairns and Blaxill, 2007]. EGR proved to be a more effective diluent than excess air in increasing combustion duration [Atkins and Koch, 2005]. Depending on the specific operating condition, and the fuel used, the effects of EGR can be different [Sjoberg et al., 2007]. One difficulty in utilizing EGR for HCCI combustion control is the relatively slow dynamics of externally routed EGR. There is also uncertainty of EGR composition and temperature with changes in operating load. Both internal and external EGR suffer from the difficulty in measuring or estimating the actual amount of EGR delivered, this obstacle becomes particularly prevalent under tran-

sient operation. Since either air or EGR can be used to control dilution and since it is difficult to accurately determine EGR, particularly during transients, only air dilution is used in this study.

Fuel composition plays a significant role in the ability for a given engine to operate in HCCI mode at a given engine operating condition. Fuels that easily auto-ignite, such as commercially available Diesel fuels and n-heptane, require lower compression ratios, and lower intake air temperatures to achieve HCCI. Fuels that resist the auto-ignition process, such as commercially available gasolines, iso-octane, natural gas, and methanol require greater compression ratios and intake temperatures. For a variable compression ratio engine at fixed stoichiometry and engine speed, λ =3 N=1000 rpm, using pure n-heptane, pure iso-octane, commercial gasoline and commercial Diesel can all be run on the same engine with the same combustion timing [Christensen et al., 1999]. Without intake air heating the n-heptane fueling requires a compression ratio of 11:1, while the iso-octane requires a compression ratio of 21.5:1. With intake air heating of $320°C$ an engine with a compression ratio of 11.5:1 can achieve HCCI using ethanol, methanol, and several grades of commercial gasoline [Oakley et al., 2001]. By correctly adjusting the engine configuration and operating condition to the desired fuel, HCCI is possible for a range of typical fuels.

2.4 HCCI-SI Mode Switching

The limited load-speed range of stable HCCI demands the ability to switch from HCCI to traditional SI modes [Milovanovic et al., 2005a]. With an engine capable of both HCCI and SI combustion modes, the benefits of HCCI can be realized for low load operation, while the high specific power density and comparatively robust combustion of SI can be realized at high loads [Kulzer et al., 2007]. With single fuel operation the difficulty in mode-switching is in quickly adjusting the conditions at

IVC from being favorable for SI to those favorable for HCCI for an SI to HCCI transition (and vice versa for an HCCI to SI transition). Due to the high thermal inertia associated with heating of the intake charge, making fast changes to T_{int} is a difficult proposition using electrical heating. With a system dedicated to producing fast changes in T_{int}, the response of T_{int} can be made to have a time constant of 8 engine cycles, with a delay of 4 engine cycles by mixing streams of fresh (cool) air and heated air [Haraldsson et al., 2004]. Although a system of this nature may produce acceptable transient results, the complexity of the system would make it impractical for production applications.

Quickly changing the amount of hot residual fraction remaining in the cylinder to initiate HCCI is another method for which SI-HCCI mode transitions can be made. To achieve this experimentally researchers have mainly used variable valve timing of several forms. By quickly changing the in-cylinder conditions with variable valve timing, a SI-HCCI transitions can be performed. In a series of papers, [Milovanovic et al., 2005a, Milovanovic et al., 2005b] the ability of a hydraulically actuated fully flexible valvetrain to mimic a cam profile switching system with variable phasing, in performing SI-HCCI transitions is shown. This system on a port fuel injected single cylinder engine running nominally stoichiometric in both HCCI and SI modes is demonstrated by using high internal EGR when in HCCI mode. Smooth transitions from SI-HCCI mode with no misfire or knocking for engine speeds of 1700, 2000, and 2700rpm [Milovanovic et al., 2005a]. Constant fueling is maintained through the transients, which results in lean excursions during the transitions (to approximately 16:1 air-fuel ratio) [Milovanovic et al., 2005a]. In performing HCCI-SI transitions, 1-2 misfire cycles occur for each of the tests in this study as a result of unsynchronized throttle and valvetrain movements. In a similar study [Cairns and Blaxill, 2007] a 4 cylinder engine equipped with production cam profile switching and direct injection is used to implement HCCI-SI mode transitions with

internal EGR. As with [Milovanovic et al., 2005a] smooth SI-HCCI mode transitions can be made with minimal load disturbance [Cairns and Blaxill, 2007]. Performance is further improved by including external EGR along with the internal EGR. For HCCI-SI transitions, using the method of [Cairns and Blaxill, 2007], a misfire on the last HCCI cycle (for one cylinder) and an approximately 10% spike in IMEP for several SI cycles following the transition. The difficulties in transition are attributed to the inability to adequately compensate each cylinder for the closing of the throttle while changing cam profiles during the transition. A lean spike from the nominally stoichiometric operation to a λ of 1.5 is also shown during this transition. In a simulation work, [Xu et al., 2004], the authors suggest the load disturbances noticed in the techniques of Milovanovic et a. and Cairns and Blaxill in HCCI-SI transitions could be reduced by preemptively closing the throttle, before implementing the cam profile change.

Utilizing a single cylinder engine with fully flexible electro-hydraulic valvetrain and direct injection [Kulzer et al., 2007], are able to realize smooth SI-HCCI (and HCCI-SI) transitions on a cycle to cycle basis. A physical model based controller is used to control the engine with predefined valve timings and fuel injection (timing as well as number of injections) to achieve residual recompression, residual re-induction, and either stoichiometric or lean HCCI operation.

Chapter 3

Experimental Setup

The experimental setup of the engine testbed is described in this chapter. In Section 3.1 a general engine description is given with overall schematics of the system flow and instrumentation. The data acquisition system is described in Section 3.2. Section 3.3 gives a description of the combustion analysis system and in Section 3.4 the operation of the emissions bench is described. To supplement this chapter, a list of the experimental equipment and a summary of programs used to run the engine and collect data are given in Appendix B.

3.1 Ricardo Single Cylinder Engine

The engine block used in this study is a Ricardo Hydra Mark III single cylinder fitted with a MG Rover K7 series cylinder head. The cast iron Ricardo engine block is adapted to the cylinder head by way of an aluminum cylinder barrel fitted with a wet iron sleeve. The basic engine geometry is shown in Table 3.1. The piston used is a production Rover flat top cast aluminum piston with valve reliefs. The Rover K7 cylinder head includes dual camshafts located in the cylinder head, one operating the two intake valves and the other the two exhaust valves. The camshaft timings in Table 3.1 are the crankshaft angle corresponding to a valve lift of 0.005″ (0.1mm) and can be considered accurate within ±2 Crank Angle Degrees (CAD). The compression

ratio of the engine is measured by dripping oil from a buret into the cylinder head combustion chamber, as well as the cylinder piston top with the engine disassembled. A clear acrylic plate is used to ensure the space has been completely filled with oil. Compensation for the compressed head gasket clearance volume is also made. The error in the compression ratio is estimated at less than 0.1 points of compression. As the cylinder head is originally built for a 4 cylinder engine, it has been shortened to include only the intake and exhaust passages for one cylinder.

The combustion chamber in the Rover K7 cylinder head is a pent-roof design with a centrally located spark plug. Overall the Ricardo engine is representative of a modern light duty automotive SI engine in terms of overall engine geometry as well as intake/exhaust port designs, and combustion chamber geometry.

Bore x Stroke	80 mm x 89 mm
Connecting rod length	159 mm
Displacement	0.45 L
Comp. Ratio	10.0:1
No. of valves	4
Maximum valve lift	8.9 mm
IVO	8 CAD bTDC
IVC	52 CAD aBDC
EVO	69 CAD bBDC
EVC	1 CAD aTDC

Table 3.1: General dimensions of the Ricardo Hydra Engine

An overall engine schematic is shown in Figure 3.1. The flow of fresh air and exhaust into and out of the engine, the fuel systems, and the emissions bench sample locations are shown in Figure 3.1. Fresh air entering the engine is measured with the laminar flow element before passing through the butterfly throttle valve. Using the throttle valve and the variable speed electric motor driving the supercharger, the intake manifold pressure can be adjusted to the value desired. The mixture then enters the intake manifold plenum where a 600W electrical band-type heater is used to increase the mixture temperature to the desired value for HCCI operation.

Immediately downstream of the plenum is a $1/16''$ thick plate with a $3/8''$ hole. This restriction is used to dampen pulsations from the supercharger and intake plenum. Finally the mixture enters the intake runner which leads directly to the cylinder.

As seen in Figure 3.1 the engine is equipped with two separate fuel systems. Each system consists of a storage tank, external fuel pump, fuel pressure regulator, and fuel injector. Both systems operate with a nominal 3 bar fuel pressure relative to engine intake manifold pressure. One fuel system contains n-heptane and the other iso-octane. The n-heptane fuel system also has the Pierburg PLU-4000 fuel measurement system mounted inline for measurement of the fuel mass flow rate. In the Pierburg apparatus, the fuel density is measured with a U-tube resonant frequency sensor, and the flow rate is measured with a positive displacement volume flow meter. The resolution of the density meter is $0.0001 g/cm^3$ and the resolution of the flow meter is $0.4\ \mu L$. An internal processor determines the average fuel mass flow rate as well as the variation in mass flow rate and reports these values to the ADAPT Baseline DAC through an RS-232 serial connection. Fuel flow rate for the iso-octane injector is estimated using the value of PW_{octane} :

$$PW_{octane} = K_f \times m_{octane} + K_{offset} \tag{3.1}$$

The parameters K_f and K_{offset} are determined from a calibration using the Pierburg apparatus to measure fuel flow rate as a function of PW_{octane} , as shown in Appendix B.2.3. Since the constant K_{offset} is a function of the supply voltage, the voltage is held $13.0 \pm 0.2V$. An automotive 12V battery, along with a commercial battery charger are used to supply power for the fuel injectors.

Both fuel injectors are located in the intake port upstream of the intake valves. The iso-octane injector is mounted in the stock Rover position approximately 10cm from the intake valves and aimed directly at the back of the intake valves. Due to

space constraints the n-heptane injector is mounted approximately 25cm from the back of the intake valves and is aimed so the spray axis is approximately coincident with the intake port axis.

A dSpace MicroAutobox 1401/1501 [dSPACE, 2005] is used as the Engine Control Unit (ECU). This controller provides a highly customizable method of engine control. The ECU algorithm is initially coded in Matlab/Simulink which is then automatically compiled to run on the embedded target processor using Matlab Real-Time Workshop. A PC program connected to the MicroAutobox processor through a dedicated bus allows viewing and modification of the Simulink variables online while the engine is running. The logic level signals from the MicroAutobox are amplified with a custom power electronics module in order to drive the fuel injectors and ignition coil [Hitachi North America, 2003]. The MicroAutobox together with the custom power electronics is referred to as the ECU in the following text. Inputs to the MicroAutobox are two hall effect sensors, one located on a 36-1 toothed wheel on the crankshaft, and the other a 1 pulse/engine cycle wheel located on the exhaust camshaft. These two inputs, conditioned to TTL levels by the power electronics module, provide the MicroAutobox with the necessary information for engine angle tracking for correct timing of injection and ignition. In the configuration used for this study, two high impedance port fuel injectors, as well as an ignition coil are controlled by the ECU. The fuel injection pulse width as well as the crankshaft angle for start of injection are controlled. The resolution of $PW_{heptane}$ and PW_{octane} is set at 10μsec. The end of injection timing for all tests is set to TDC on the compression stroke. The ignition system is used only in the SI tests and when warming up the engine to run HCCI tests. During all HCCI tests the ignition system is turned off. An analog input on the ECU is used to measure MAP, while a RS-232 serial connection to the ADAPT RTP provides the ECU with the value of T_{int} at a rate of 100Hz. The background tasks of the Simulink model are run at a rate of 1000Hz, while the values

of $PW_{heptane}$ and PW_{octane} are calculated each engine cycle during the intake stroke, to ensure that the calculations finish before the start of injection on that cycle.

To measure the engine out value of λ, an ECM AFRecorder 1200 Universal Exhaust Gas Oxygen sensor (UEGO) is used. The UEGO is positioned approximately 25cm downstream of the exhaust valve, in the exhaust system. The UEGO is capable of directly measuring the oxygen content of the exhaust with a time constant of <150msec, which gives nearly cycle by cycle resolution for the engine speeds in this study. With the known fuel hydrogen to carbon ratio of a 2.29 for n-heptane and 2.25 for iso-octane, the UEGO is able to output a direct measurement of λ measured in the exhaust. Dynamic changes to hydrogen/carbon ratio of the fuel result in an error of 0.22 AFR units, at an AFR of 60.50:1. The analog output of the UEGO updates at a rate of 100Hz.

Brake torque of the engine is measured with the dynamometer. The dynamometer consists of an AC electrical motor mounted on pillow block bearings, with a load cell used to measure the reaction torque. At a steady engine speed, the reaction torque measured by the load cell is equal to the load placed on the engine by the AC motor. With the dimension of the radial distance of the load cell from the AC motor axis of rotation and a calibrated load cell, engine brake power is calculated with engine speed and brake torque (T) using:

$$\mathrm{P}_{Brake} = 2\pi \mathrm{T} N/60 \tag{3.2}$$

The Brake Mean Effective Pressure (BMEP) can then be calculated using:

$$BMEP = \frac{2\mathrm{P}_{Brake}}{V_{Disp} N/60} = \frac{4\pi \mathrm{T}}{V_{Disp}} \tag{3.3}$$

Here, Eqn. 3.2 is used to determine the brake power without compensation for the inlet air heating or the supercharger work. This is done as the supercharger used in

this study is a commercial supercharger (Eaton Automotive model MP45) and is over sized for this single cylinder application, and as such has an adiabatic efficiency much lower than for a properly sized unit. Use of a turbocharger instead of mechanically driven supercharger has the advantage of minimizing additional pumping losses for the moderate boost levels in this study even with the low exhaust gas temperatures of HCCI [Olsson et al., 2004]. Similarly the intake air heater is not compensated as waste heat from the cooling system or exhaust could partially supply this energy in a production application such [Hyvonen et al., 2003].

Electrical pumps supply the coolant and lubricating oil to the engine. To quickly warm the engine coolant and oil temperature to a constant value, electrical heaters are used to heat both fluids. The fluid temperatures are maintained by heat exchangers in the coolant and oil flow circuits, with regulated amounts of domestic cold water used to maintain the temperatures. Due to the low load of HCCI operation it is often necessary to leave the electrical heaters on during engine operation while using minimal amounts of cooling water to regulate the engine temperature to the desired value.

Two main systems are used for data acquisition in this study. The ADAPT Baseline DAC system from [A&D Technologies, 2001a] is the main real time processor that controls the test cell and is responsible for data logging of all of the testbed sensors. Shown in Figure 3.2 are the locations of the sensors in the test cell. All labeled sensors are sampled by the ADAPT Baseline DAC at a constant sample rate of 100Hz. Also shown in Figure 3.2 is the Baseline Combustion Analysis System (CAS) from A&D Technologies that is used for data logging on a crank angle basis [A&D Technologies, 2001b]. The sensors measured by the CAS system are also shown in Figure 3.2. Details of the ADAPT system are in Section 3.2 and the CAS system setup is further detailed in Section 3.3.

Shown in Figure 3.3 are the actuators used to control the engine. Step responses

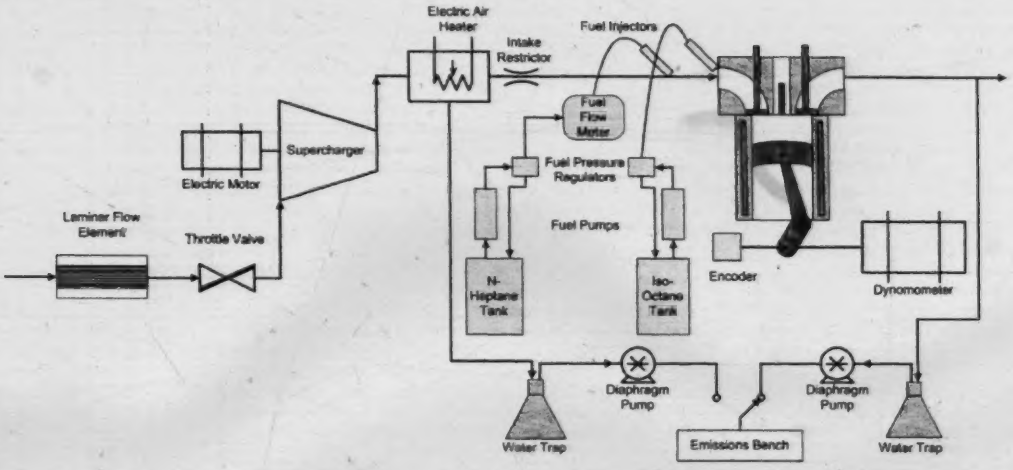

Figure 3.1: Schematic of Ricardo Single Cylinder Engine Experimental Setup - sensors, actuators, and data acquisition systems not shown

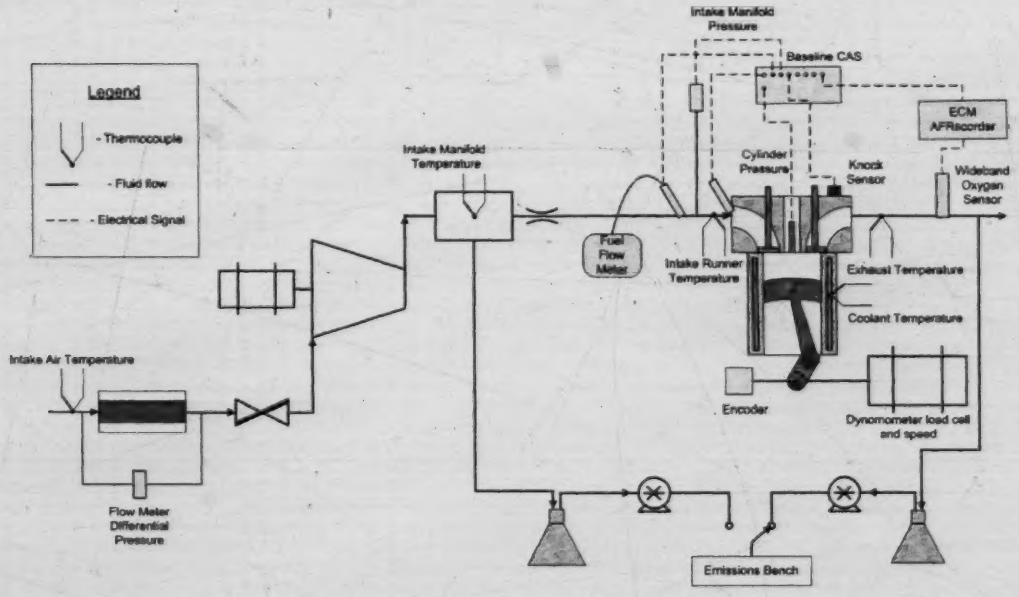

Figure 3.2: Schematic of Variables Captured with Data Acquisition

to the MAP, ON, and fuel quantity are commanded. The Baseline DAC system is used to control the throttle valve and the supercharger drive motor speed to control

the manifold pressure, as well as the intake air heater supplied power. The intake air heater is a band-type heater, which wraps around the outer surface of the intake manifold. With this style of heater the intake air temperature changes very slowly (on the order of minutes) due to the large thermal inertia of heating the intake manifold itself, as well as the volume of air in the manifold. With the available heater, step changes to the intake temperature from cycle to cycle could not be made. Control of the ON and fuel injector PW's are controlled by the dSpace MicroAutobox ECU.

The fuel injector pulse width for each injector can be set independently, using one of two methods: the PW of each injector can be set manually, or the control logic for HCCI to SI mode switching, detailed in Section 5.5, can be used to automatically calculate the PW for each injector.

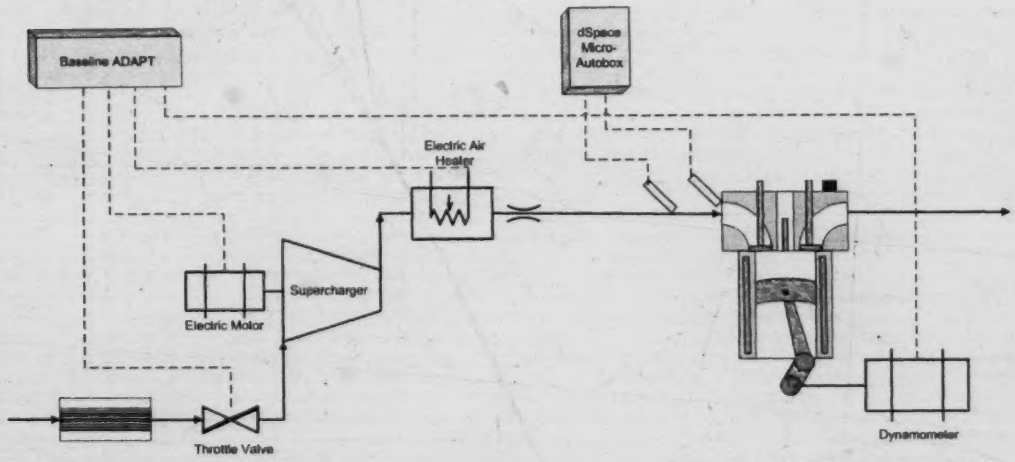

Figure 3.3: Schematic of Available Actuators

3.2 Data Acquisition System

Control of the test cell is done with the MTS Powertrain ADAPT Baseline DAC. The Baseline DAC consists of a real time processor with a TCP/IP connection to a

PC. The ADAPT software on the PC provides a user interface to view the real time variables of the engine as well as initiate data logging on the processor.

Also connected to the processor is an interface to analog, digital, and frequency I/O boards. A summary of the available I/O is shown in Table 3.2. For thermocouple measurements, up to 16 channels of each K-type and J-type can be used by utilizing the analog input channels. Built in amplifiers, voltage to temperature conversion and cold junction compensation is provided within the thermocouple boards and ADAPT software.

Input Type	Quantity	Specifications
Analog Input	48	Range: +/- 10 V,+/- 500 mV, +/-50 mV Input gain: 1,10,100 Resolution: 16 bit Accuracy +/- 450 μV on 10 V range Single pole 35 Hz input filter
Analog Output	4	Range: +/- 10 V Resolution: 14 bit Settling time: 200 μsec to 0.1 % of FS
Digital Input	8	Threshold: 2.4-40 V Input Filter: 10 kHz
Digital Output	8	Max. Current Draw: 1 A
Frequency Input	3	Max. Input Frequency: 500 kHz
Serial	6	RS-232 protocol

Table 3.2: ADAPT Baseline DAC Specifications

A Eurotherm drive is a commercial variable speed drive which is set to hold the AC-dynamometer speed to the setpoint using a feedback controller. To control the dynamometer, the Baseline DAC is connected with the Eurotherm Drives' AC motor controller. Engine speed is set in the ADAPT software and an analog signal is sent to the Eurotherm controller as the speed setpoint. A frequency input is used to monitor engine speed, which is measured at the engine flywheel with a 100 tooth wheel. Another frequency input is used to monitor the dynamometer speed at the opposite side to the engine, using an 256 pulse/rev encoder. Two safety strings are

used to protect the engine and the operator in the event of a failure. If the engine should loose oil pressure, or the fan cooling the AC dynamometer is not enabled, the safety string is activated. Should either of the safety strings be activated, the fuel pumps are automatically disabled and the dynamometer stops the engine.

3.3 Combustion Analysis System

The cylinder head has been modified for an in-cylinder pressure transducer located between the intake and exhaust valves along the centerline of the engine bore. A sleeve for mounting the transducer is used to seal the transducer from engine coolant. Inside the combustion chamber, the Kistler ThermoCOMP model 6043A60 pressure transducer is mounted so the sensing diaphragm is flush with the combustion chamber. The Kistler transducer is a piezoelectric pressure transducer that determines changes in pressure based on a charge produced by a piezoelectric material when a force is applied. Combustion pressures act on a protective diaphragm which in turn impart a force on the piezoelectric crystal. This changing force produces a charge in the crystal. The charge produced by this crystal is sensed by an MTS Powertrain model 1108 charge amplifier located directly next to the sensor and integrated to give a measure of the pressure. This amplifier converts the small charge (19.9 pC /bar) produced by the piezoelectric crystal into an analog voltage.

Since the piezoelectric crystal measures changes in pressure, it is not well suited to measuring steady state pressure. The charge amplifier integrates the charge signal from the transducer so it is susceptible to drift. To overcome this problem, the in-cylinder pressure transducer is reset to (pegged) the absolute pressure measured in the intake manifold by the Setra MAP sensor. Pegging of the in-cylinder pressure signal to the MAP signal is performed by the CAS system so that long term drift of the in-cylinder sensor is eliminated, and the absolute value of the in-cylinder pressure

is determined. For each cycle for the 10 CAD around Bottom Dead Center (BDC) of the intake stroke, the average pressure of the in-cylinder pressure is made to be equal to the pressure measured by the MAP sensor over the same period.

Measurements of the in-cylinder pressure are made at 0.1 CAD intervals as determined by the BEI Industries model XH25D-SS-3600-T2-ABZC-7272-SM18 crankshaft mounted encoder. The encoder produces two signals that are used to determine the relationship of the encoder with the movements of the piston. The first signal, already described, produces a square wave signal at 0.1 CAD intervals for the entire revolution. The second signal produces one signal of 0.1 CAD duration once per revolution. To determine the relationship between the 1 pulse/rev signal and the location of TDC, the engine is motored at a constant speed, and the maximum pressure of the in-cylinder pressure is compared with the location of the 1 pulse/rev signal. As there are heat transfer, blow-by mass losses, and piston dwell effects, the maximum pressure is achieved slightly before TDC. The angular difference between the maximum pressure and the actual location of TDC is referred to as the Thermodynamic Loss Angle (TLA). Measurements of the piston motion with an LVDT displacement transducer mounted in the spark plug hole are initially used to set the encoder offset, and thus determine the TLA for a motored condition. For a fully warm engine at 1000rpm motoring at Wide Open Throttle (WOT), the TLA was found to be 2 CAD. The encoder offset is periodically checked to ensure no physical movement between the relationship of the crankshaft and the encoder. With the relationship of the 1 pulse/rev signal fixed with relation to the piston movements, the measurements of cylinder pressure at 0.1 CAD intervals can be made with respect to absolute crankshaft angle. Further information on this procedure can be found in Appendix B.2.1.

To record the values of the in-cylinder pressure from the charge amplifier, the MTS Powertrain Basline CAS system is used. The CAS system consists of a self contained processor that is connected to a PC with a TCP/IP connection. The CAS

hardware has inputs for the crankshaft encoder, the charge amplifier for cylinder pressure measurement, as well as +/-10 V analog inputs for additional measurements. The CAS system has automatic compensation for the encoder offset with respect to TDC with correction for the TLA. To have crank angle synchronous relationship between cylinder pressure values of MAP, λ measured with the UEGO, the knock sensor and fuel injector pulse widths, these values are also measured with the analog inputs of the CAS system. The value of MAP is measured at intervals of 1 CAD for the entire engine cycle, the value of λ is measured every 5 CAD, and the knock sensor is measured every 0.1 CAD for 100 CAD starting at 10 CAD before TDC on the compression stroke. The signal active time of each fuel injector is measured online for each cycle, and the value recorded in the data logs.

Within the CAS software there is the ability to calculate combustion metrics online, cycle by cycle. Values of: total heat release, location of 50% mass fraction burned (denoted CA50), peak pressure, and indicated mean effective pressure can be viewed online as well as recorded during the data acquisition. The online values are viewed via a dedicated PC which receives the combustion metrics from the CAS system via an ethernet connection. The raw measurements are stored on the CAS system and transferred at the end of the prescribed number of test cycles.

3.4 Emissions Bench

Emissions data is collected with an emissions bench that measures 5 gases. The specifications of the 4 analyzers used are shown in Table 3.3. The emissions are sampled from either the intake manifold or from the exhaust of the engine as shown in Figure 3.1. A three way electronic solenoid valve can be switched to select which source of emissions is sampled. Emissions can be sampled from either the intake manifold, or the exhaust. Before the sampled gases go to the analyzers, they are

drawn through a cooling coil and an Erlenmeyer flask which acts as a water trap. The cooling and water removal is necessary to prevent bias as well as damage to the analyzers. The sampled gases are then filtered to remove any particulate matter that may remain in the samples. To pull the gases from the sample source (i.e. the intake manifold or the exhaust) and to provide the necessary pressure and flow rate for the analyzers, two diaphragm pumps are used to supply gases to the analyzers at a pressure of 3 psig. The emissions equipment is calibrated with a zero and ~90 % span calibration with standard compressed gases on a weekly basis.

Manufacturer	Model	Measurement Gas	Range	Resolution
Horriba	CLA-510SS	NO_x	0-2500 ppm	1ppm
Horriba	FIA-510	THC (as CH_4)	0-10000 ppm	10ppm
Siemens	OXYMAT6	O_2	0-25%	0.01%
Siemens	ULTRAMAT6	CO	0-10%	0.01%
		CO_2	0-25%	0.01%

Table 3.3: Emissions Bench Analyzers and Measurement Ranges

Chapter 4

Experimental Procedure

The experimental procedure for collecting and analyzing data is explained in this chapter. First the fuels used during the experiments, and the operating region for which stable HCCI exists are defined. The procedure for collecting steady state data is covered along with the range of engine operating conditions for which data was collected. Similarly for transient test data, the data collection procedure is explained. Finally the data analysis methods are detailed, along with the performance metrics used to quantify the characteristics of the engine.

4.1 Research Fuels

The ability of a fuel to auto-ignite is a critical property for HCCI engines. This same property is also critical for SI engines to prevent harmful knock, [Heywood, 1988]. The standard rating scale for rating the resistance of a fuel to auto-ignition is the ON. The two fuels which define the ON scale are n-heptane and iso-octane (where the nomenclature Octane Number is derived). These two fuels have very similar physical properties, as shown in Table 4.1 with the exception of their ability to auto-ignite.

The straight chain paraffin, n-heptane is susceptible to auto-ignition (or knock in SI engines), while the branched structure of iso-octane resists the auto-ignition process. These two fuels are by definition the PRF which define the ON scale with

Property	n-heptane	iso-octane
Formula	C_7H_{16}	C_8H_{18}
Molecular Weight [kg/kmol]	100.2	114.2
Higher Heating Value [MJ/kg]	48.07	47.77
Lower Heating Value [MJ/kg]	44.56	44.30
Density [kg/m^3]	686.6	693.8
Octane Number (ON)	0	100
Hydrogen/Carbon ratio	2.29	2.25
Boiling Point [$^\circ C$]	98	99

Table 4.1: Fuel Properties [Owen and Coley, 1990]

n-heptane an ON of 0, and iso-octane 100. Mixtures of these two fuels, measured on a volume basis define the ON (also sometimes called the PRF number) as:

$$ON = \frac{V_{octane}}{V_{octane} + V_{heptane}} \tag{4.1}$$

The PRF's were chosen for this study as they are pure compounds of known composition whereas commercially available fuels can be mixtures of hundreds of different hydrocarbons. The exact chemical constituents of these commercial fuels would not be known, and would depend on the supplier of the fuel. These commercially available fuels are also often seasonal in nature, with variable properties depending on the time of year.

4.2 Operating Region Definition

Acceptable HCCI operation exists between the lean and rich limits, for a given operating condition (T_{int}, MAP, N). Beyond the lean limit the engine excessively misfires leading to the engine not firing on any cycle. Beyond the rich limit knock increases significantly, leading to drastically increased maximum pressures and the potential for engine damage. To quantify the lean limit for each operating point, the point at which the COV_{IMEP} exceeds ~5% is used. Beyond this limit of COV_{IMEP} the engine was found to excessively misfire for the range of operating conditions tested.

As the injected fuel quantity increases, the rate of pressure rise and the potential for knock increases. To prevent potential damage to the engine from excessively rapid combustion or knock, two metries are used to define the rich limit. A limit on the pressure rise rate during the HTR region of combustion, defined by Eqn. 5.6, of 7bar/CAD is imposed, as exceeding this was found to result in dramatically increased audible combustion noise from the engine for all engine speeds tested. The other limit imposed on the rich limit of combustion is the onset of the structural vibrations induced due to knocking combustion. A peak amplitude of 0.5V (equivalent to approximately $250m/s^2$), as measured by the knock sensor, is used as the knocking limit. Depending on the engine operating condition either the pressure rise rate limit, or the knocking limit can be reached independently. Further investigation to the knocking characteristics of this engine can be found in Section 5.3.5. The piston of the Ricardo engine is also limited by the manufacturer to 75bar peak cylinder pressure. This peak cylinder pressure limit is not exceeded in this work.

4.3 Test Procedures and Matrix of Test Points

The matrix of experimental data points, for each of the different types of tests, are shown in this section. The first series of points run are three series of tests to determine the optimum combustion timing to use in HCCI mode for steady state testing. These points are denoted as Combustion Timing (CT) test points. Then the range of Steady State (SS) points is run to determine the range of operating conditions for which HCCI is possible for the experimental setup. To determine the ability of the experimental setup to repeat a given test point, a series of Repeated Trail (RT) tests are taken. The steady state points are also used to form the start and end conditions for the TRansient (TR) test cases. Finally a series of Mode Switching (MS) tests are taken to show the ability of the dual fuel systems to actuate SI-HCCI mode switching are

shown. To refer to a group of tests together, several similar test points are grouped into 'cases' of tests. Unless otherwise specified, reference to a test case includes all tests points within that case.

At the start of each series of tests the ambient barometric pressure, as measured with a mercury manometer, and dry and wet bulb temperatures (to give a relative humidity reading) are recorded. For all tests the engine is run in SI mode to allow the engine coolant temperature to stabilize at the preset value of $80°C$. Once the engine has reached the fully warm condition, the engine speed can be set and the intake air heater turned on to increase the intake air temperature. If higher intake manifold pressures are desired, the throttle is opened and the speed of the supercharger is set to a constant value to maintain the desired pressure using the variable speed electric motor drive. As the air temperature increases the ON is lowered via the two injector fuel system until HCCI operation is obtained. As the supercharger increases intake air temperatures due to compression heating, the electrical heater power can then be reduced to maintain the desired intake air temperature. A combination of electrical heating, and varying the throttle angle to reduce the supercharger's adiabatic efficiency (at a given MAP) are used to maintain the desired intake temperature.

In this investigation the combustion timing for the steady state tests is held constant for three loads at each operating condition. This is done to eliminate the combustion timing as a variable when determining combustion and performance metrics. A constant combustion timing is also useful in transient tests where variations from the set combustion timing can be identified during transients.

To determine the optimum combustion timing for a given condition, a sweep of combustion timing is performed. For the range of tests performed in this work the main factor influencing optimum combustion timing is engine speed. For low load conditions it may be beneficial to advance combustion timing [Hyvonen et al., 2003] to improve combustion efficiency and reduce fuel consumption. However, for this

work the timing over the load range is set constant over all loads in order to directly determine the effect of transients on combustion timing.

Changes in engine speed were found to alter the SOC range for which the largest stable range of HCCI could be obtained. Thus for each engine speed, a combustion timing which results in stable operation of the engine for a range of tests must be found. For each engine speed in this study, a sweep of the combustion timing with constant fueling ($PW_{heptane}$ and PW_{octane}) is done. The fueling for each test in Table 4.2 represents an intermediate load condition for the engine speed, and MAP. The 'optimum' combustion timing for each engine speed represents the optimum for this intermediate load. This is done to have a representative SOC for each engine speed and load. The conditions in Table 4.2 also represent operating conditions away from both the knock and misfire boundaries to ensure the combustion remains stable throughout the combustion timing sweep to maximize the combustion timing range which can be obtained.

To change the combustion timing while keeping a constant fueling, the T_{int} is varied. The increased temperature in the intake port potentially changes the absolute volumetric efficiency of the engine (hence changing the value of λ); however, the constant fueling results in the same fuel energy for combustion. The main contributor to changes in engine load will thus be the effect of combustion timing on the thermodynamic efficiency of the engine. Late combustion timings result in a lower expansion ratio after combustion, and thus reduced power output. Similarly combustion timings which are too early result in increased compression work, as the mixture combusts as the piston ascends. Early combustion timing also results in increased heat transfer to the cylinder walls, resulting in a higher heat losses, reducing the energy available to do work. The range of T_{int} in Table 4.2 represents the range for which stable HCCI exists for each case. The minimum T_{int} represents the misfire limit, while the maximum T_{int} represents the knocking limit. A summary of the conditions at the three

engine speeds is shown in Table 4.2. The cases 'A', 'B', and 'C' are used to identify each series of combustion timing tests. The experimental results of this series of tests is shown in Section 5.2.

Case	N [rpm]	MAP [kPa]	m_f [mg/cycle]	ON	T_{int} [°C]	Test Number
A	800	125	8.1	52	86	CT6
					89	CT7
					94	CT8
					102	CT9
					107	CT10
					111	CT11
					117	CT12
B	1000	125	10.2	35	94	CT13
					96	CT14
					101	CT15
					106	CT16
					110	CT17
					113	CT18
C	1200	125	13.1	17	100	CT19
					102	CT20
					107	CT21
					111	CT22

Table 4.2: Engine Operating Points for Combustion Timing Tests. See Appendix A.1 for details of each test.

To gain insight into the performance characteristics of the Ricardo engine in HCCI mode, steady state tests were run. This series of tests also serves as a basis for the subsequent transient tests, in order to determine the viable range where step transients can be performed. To provide consistency between tests, the fueling of each test point is adjusted to maintain a constant Start of Combustion (SOC), as determined by the CT-series of tests. The setpoint of SOC for the range of operating conditions is further detailed in Section 5.2.

For all of the steady state tests in this study the engine operating parameters are held constant for the duration of a test. The fuel injector PW's as well as intake heater power is kept constant with no closed loop control.

Once the engine operating parameters stabilize to their desired values, the fueling is adjusted to give the minimum load before misfire was encountered. To achieve the minimum load, the $PW_{heptane}$ is adjusted to give the desired SOC with a PW_{octane} of zero. If this pure heptane fueling results in operation below the defined lean limit, PW_{octane} is increased to bring the combustion to the desired stability. An intermediate load case approximately half way between the minimum load and maximum loads is then run by increasing PW_{octane} from the minimum load case, to increase load, and adjusting $PW_{heptane}$ to ensure the SOC remains constant. Finally the maximum load case is run by increasing PW_{octane} until the rich limit is reached, and again adjusting $PW_{heptane}$ to maintain the SOC. As described in Appendix B.2.3 there is a non-linearity in the fuel flow rate versus pulse width for pulse widths of less than ~1.3msec. To mitigate the effect of these small pulse widths, a minimum PW_{octane} of 1.30msec is enforced throughout this work. Thus the fueling can be set to give pure n-heptane fueling, with PW_{octane} of zero, or if iso-octane is desired the minimum value for PW_{octane} is 1.30msec.

Once the desired operating condition has stabilized, and all measurements are reading steady values, the ADAPT and CAS systems are used to record the data at the operating point. For the steady state tests, the ADAPT system is set to record the engine parameters at a sample rate of 100Hz, for 50 seconds. The CAS system is set to record 450 engine cycles with cylinder pressure and the knock sensor measured in 0.1 CAD increments, MAP in 1 CAD increments, and λ every 5 CAD. A summary of all test points is given in Appendix A.

Five cases of steady state tests are examined in this study. The case is used to describe the values of N and MAP . For each case, 15 test points are examined. The 15 test points are the result of 5 values of T_{int} and 3 values of load recorded at each test condition. A summary of the nominal values for these test conditions is shown in Table 4.3. The changing values of T_{int} for each test case are the result of the

minimum temperature which can be obtained at the desired MAP, due to compression heating from the supercharger. If the nominally desired minimal value of T_{int} listed in Table 4.3 could not be obtained for the desired test case, the minimum temperature allowed by the experimental setup is used. The three values of load for each test condition are the minimum load achievable at each test condition, the maximum load achievable, and an intermediate load approximately half way between the minimum and maximum loads called the medium load.

Case	N [rpm]	MAP [kPa]	T_{int} [°C]	Load	Test Number
D	1000	110	60	min, med, max	SS 1, SS 2, SS 3
	1000	110	70	min, med, max	SS 4, SS 5, SS 6
	1000	110	80	min, med, max	SS 7, SS 8, SS 9
	1000	110	90	min, med, max	SS10, SS11, SS12
	1000	110	100	min, med, max	SS13, SS14, SS15
E	1000	125	90	min, med, max	SS16, SS17, SS18
	1000	124	100	min, med, max	SS19, SS20, SS21
	1000	124	110	min, med, max	SS22, SS23, SS24
	1000	125	120	min, med, max	SS25, SS26, SS27
	1000	124	130	min, med, max	SS28, SS29, SS30
F	1000	140	100	min, med, max	SS31, SS32, SS33
	1000	140	110	min, med, max	SS34, SS35, SS36
	1000	140	120	min, med, max	SS37, SS38, SS39
	1000	141	130	min, med, max	SS40, SS41, SS42
	1000	140	140	min, med, max	SS43, SS44, SS45
G	800	125	80	min, med, max	SS46, SS47, SS48
	800	125	90	min, med, max	SS49, SS50, SS51
	800	125	100	min, med, max	SS52, SS53, SS54
	800	125	110	min, med, max	SS55, SS56, SS57
	800	125	120	min, med, max	SS58, SS59, SS60
H	1200	125	90	min, med, max	SS61, SS62, SS63
	1200	126	100	min, med, max	SS64, SS65, SS66
	1200	126	110	min, med, max	SS67, SS68, SS69
	1200	125	120	min, med, max	SS70, SS71, SS72
	1200	126	130	min, med, max	SS73, SS74, SS75

Table 4.3: Engine Operating Points for Steady State Tests. See Appendix A.2 for details of each test.

To determine the ability of the experimental apparatus to repeat a given test

point, several of the SS test cases are repeated an additional 4 times, on separate occasions. For these tests, the values of N, MAP, T_{int} , $PW_{heptane}$, and PW_{octane} are set to the same values as the SS test case being repeated. The matrix of repeated trials of SS test points, along with the engine operating condition at each point are shown in Table 4.4. Results of this series of tests is shown in Section 5.1.

Case	N [rpm]	MAP [kPa]	T_{int} [°C]	Load	Steady State Test Number	Repeated Trials Test Numbers
N	800	125	120	min	SS58	RT1, RT16, RT31, RT46
			120	med	SS59	RT2, RT17, RT32, RT47
			120	max	SS60	RT3, RT18, RT33, RT48
O	1000	124	110	min	SS22	RT4, RT19, RT34, RT49
			110	med	SS23	RT5, RT20, RT35, RT50
			110	max	SS24	RT6, RT21, RT36, RT51
P	1200	125	90	min	SS61	RT7, RT22, RT37, RT52
			90	med	SS62	RT8, RT23, RT38, RT53
			90	max	SS63	RT9, RT24, RT39, RT54
Q	1000	110	100	min	SS13	RT10, RT25, RT40, RT55
			100	med	SS14	RT11, RT26, RT41, RT56
			100	max	SS15	RT12, RT27, RT42, RT57
R	1000	140	140	min	SS43	RT13, RT28, RT43, RT58
			140	med	SS44	RT14, RT29, RT44, RT59
			140	max	SS45	RT15, RT30, RT45, RT60

Table 4.4: Engine Operating Points for Repeated Trials of Steady State Tests. See Appendix A for details of selected tests.

To determine the effect of load transients on the HCCI combustion process, two types of transient fueling tests are performed. The first type of test is a simple step starting at the minimum load condition, and then stepping fueling up to either the intermediate load, or the maximum load. The min, med, and max load points determined by the SS-series of tests. A pulse in fueling, where fueling for the minimum load condition is stepped to the higher load condition for 200 cycles, and then stepped back to the minimum load case is also performed. These two types of tests are selected based on apriori estimates of the dynamic timescale, as per [Chang et al., 2006, Wilhelmsson et al., 2005], and the constraints of the total mem-

ory of the data acquisition equipment of 8 megasamples (~450 cycles at the current sample rates). The step transient is used to evaluate both the relatively short dynamics of the change in fueling, as well as any relatively long effects such as cylinder wall heating. The pulse transient is used to show the effect of both increasing and decreasing fueling on the response.

Step tests are initiated by running the engine with the minimum load fueling derived from the steady state operating tests. Once the engine has achieved the steady operating point logging for the CAS system and the ADAPT system are both started. After approximately 40 engine cycles, the fueling for both injectors is simultaneously switched to the higher load case (either the intermediate load, or the maximum load). For the remainder of logging, the fueling is maintained at this level.

Pulse tests are started in a similar fashion to the step tests, by running the engine to the steady state minimum load condition. The data logging for the CAS system and the ADAPT system are initiated, and the fueling is then increased to the intermediate or the maximum load condition after approximately 40 cycles. However rather than maintaining this fueling, after 200 engine cycles the ECU automatically returns the fueling to the minimum load case.

The two fuel injectors supplying different fuels on the Ricardo engine are used for SI-HCCI mode transitions. The mode switching tests are performed in a similar manner to that of the transient tests, where the data logging is started with the engine running in steady state HCCI. Throughout the tests the engine is either manually switched from SI-HCCI and HCCI-SI, or the logic implemented in the ECU for mode switching is utilized (see Section 5.5 for further details). For the mode switching tests the timing of the mode transitions are made manually and arbitrarily; however, several engine cycles are allowed in each mode before another transition in order to characterize the dynamics.

The matrix of transient test points is shown in Figure 4.3. For each load sweep of

steady state points (min, med, and max loads) there are a total of four corresponding transient tests. Step tests going from the minimum load to the medium and maximum load, and Pulse tests going from the minimum load to the medium and maximum loads (and then back down to the minimum load) are performed.

Case	N [rpm]	MAP [kPa]	T_{int} [°C]	Initial State	Transition to State	Step Test Test Number	Pulse Test Number
I	1000	110	63	SS 1	SS 2, SS 3	TR 1, TR 2	TR 3, TR 4
	1000	110	70	SS 4	SS 5, SS 6	TR 5, TR 6	TR 7, TR 8
	1000	110	80	SS 7	SS 8, SS 9	TR 9, TR10	TR11, TR12
	1000	110	90	SS10	SS11, SS12	TR13, TR14	TR15, TR16
	1000	110	100	SS13	SS14, SS15	TR17, TR18	TR19, TR20
J	1000	125	90	SS16	SS17, SS18	TR21, TR22	TR23, TR24
	1000	124	100	SS19	SS20, SS21	TR25, TR26	TR27, TR28
	1000	124	110	SS22	SS23, SS24	TR29, TR30	TR31, TR32
	1000	125	120	SS25	SS26, SS27	TR33, TR34	TR35, TR36
	1000	124	130	SS28	SS29, SS30	TR37, TR38	TR39, TR40
K	1000	140	100	SS31	SS32, SS33	TR41, TR42	TR43, TR44
	1000	140	110	SS34	SS35, SS36	TR45, TR46	TR47, TR48
	1000	140	120	SS37	SS38, SS39	TR49, TR50	TR51, TR52
	1000	141	130	SS40	SS41, SS42	TR53, TR54	TR55, TR56
	1000	140	140	SS43	SS44, SS45	TR57, TR58	TR59, TR60
L	800	125	77	SS46	SS47, SS48	TR61, TR62	TR63, TR64
	800	125	90	SS49	SS50, SS51	TR65, TR66	TR67, TR68
	800	125	100	SS52	SS53, SS54	TR69, TR70	TR71, TR72
	800	125	110	SS55	SS56, SS57	TR73, TR74	TR75, TR76
	800	125	120	SS58	SS59, SS60	TR77, TR78	TR79, TR80
M	1200	125	90	SS61	SS62, SS63	TR81, TR82	TR83, TR84
	1200	126	100	SS64	SS65, SS66	TR85, TR86	TR87, TR88
	1200	126	110	SS67	SS68, SS69	TR89, TR90	TR91, TR92
	1200	125	120	SS70	SS71, SS72	TR93, TR94	TR95, TR96
	1200	126	130	SS73	SS74, SS75	TR97, TR98	TR99, TR100

Table 4.5: Engine Operating Points for Transient Step and Pulse Tests. See Appendix A.4 for details of selected tests

To show the ability of a dual fuel system actuation system to allow SI-HCCI mode transitions, a series of mode switching tests is taken. The series of test points is shown in Table 4.6. Tests are performed at both constant load between both SI and HCCI modes, as well as constant MAP, where MAP is held constant across the mode

transitions. Test case MS12 is a strictly SI test point to show the effect of stepping fueling to observe the effects of fueling dynamics. This test point is analyzed in Section 5.4 with the transient test cases.

N [rev/min]	MAP - HCCI [kPa]	MAP - SI [kPa]	T_{int} [°C]	Test Number	Comment
1000	120	65	80	MS1	Constant load
1000	100	65	80	MS2	Constant load
1000	100	65	80	MS3	Constant load
1000	100	100	80	MS4	Constant MAP
1000	115	65	80	MS5	Constant MAP
1000	120	65	90	MS7	Constant load
1000	100	100	90	MS8	Constant MAP
1000	-	85	75	MS12	SI Only test

Table 4.6: Engine Operating Points for Mode Switching tests. See Appendix A.4 for details of selected tests

4.4 Cylinder Pressure Analysis

The in-cylinder pressure measurement provides the most direct information about the combustion performance in this engine. Analysis on the in-cylinder pressure trace along with other external measurements are used to determine metrics of the physical processes in the engine. A post-processing program is used to analyze the in-cylinder pressure. A summary of the important programs in performing the analysis are given in Appendix B.3.

4.4.1 Cylinder Pressure Signal Filter

The raw in-cylinder pressure signal is subject to both process and measurement noise. Since the in-cylinder pressure is a critical measurement parameter a clean signal is desired. In particular for the heat release analysis, where the numerical derivative of this signal is taken, even small amounts of noise can drastically alter the result. To attenuate this noise a 7th order low pass Butterworth filter is used. To eliminate any

phase lag associated with the filtering process, the filter is run through the data in the forward and reverse directions. Since the data is collected in the crankshaft angle domain the filtering is also done in this domain.

The main contributor to the process noise is knock. The high frequency pressure oscillations associated with knock are measured by the pressure transducer, but do not reflect the actual average cylinder pressure, which is the quantity desired. To design the low pass filter, the frequency content of the desired processes and the undesirable noise must be characterized. A complete cycle of the measured in-cylinder pressure trace is shown in Figure 4.2, for a cycle with a fast combustion event with knock. The intake and exhaust strokes have relatively slow processes, occurring over 180CAD. The compression and exhaust strokes are slightly faster processes, but again occur over 180CAD. The main combustion event itself represents the highest frequency process of a non-knocking cycle, occurring over a minimum span of ~5CAD. A close up of the combustion is shown in Figure 4.3. The pressure oscillations due to knock can also be seen in Figure 4.3. These oscillations can be seen to occur faster than the combustion event itself.

For combustion analysis the goal of the pressure signal filter is to attenuate the signal noise (namely the knock and high frequency electrical noise), but limit attenuation of the actual process, most importantly of which, the combustion event itself. A reduction of the knocking portion of the pressure signal by a factor of 1000, and <1% attenuation of the combustion process were taken as the design criteria. To determine the filter cutoff frequency and necessary order an estimate of the knocking frequency and combustion frequency is required for the worst case scenario. An estimate of the knocking frequency can be determined using [Draper, 1935, Andreae et al., 2007]:

$$f_{m,n} = \frac{\rho_{m,n}\sqrt{\gamma RT}}{\pi B} \tag{4.2}$$

Previous investigators, such as [Andreae et al., 2007], have found that knock in engines most significantly excites the first circumferential mode, $\rho_{1,0}$, as shown in Figure 4.1. Using the estimated values from [Andreae et al., 2007] of $T = 1600K$, $\gamma = 1.22$, $R = 287J/kgK$, along with the engine bore of 0.080m, the knocking frequency is estimated at $\rho_{1,0}$ =~5kHz. Further analysis of knock is shown in Section 5.3.5.

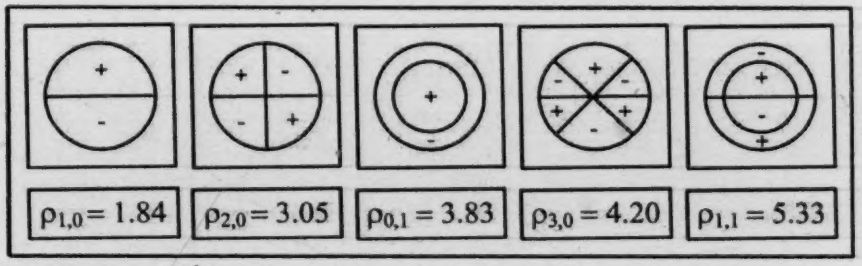

Figure 4.1: Mode Shapes and Estimated Mode Numbers

The main combustion event occurs over a minimum crankshaft angle of ~5CAD, this results in a different time domain frequency depending on the engine speed. The critical design paramter for choosing a filter cutoff frequency is at the highest engine speed of 1200rpm, where the combustion and the knock occur at the closest frequencies. At 1200rpm, 5CAD occurs in a time of 6.94×10^{-4} sec, or a frequency of 0.72kHz. The cutoff frequency must then be between 0.72kHz, and 5kHz. The value of 0.04 times the sample rate, or 2.88kHz at 1200rpm, was chosen as the cutoff frequency. To give the necessary attenuation at the knock frequency a 7th order filter is used since filtering the data in both directions effectively doubles the filter order. The cutoff frequency of the filter is maintained at 0.04 times the sample rate for all engine speeds, maintaining the same filter order. Lower engine speeds result in a widening between the frequency of the combustion event and the first knocking mode. The unfiltered and filtered pressures traces are shown in Figures 4.2 and 4.3. The frequency spectrum of the knocking pressure signal is shown in Figure 4.4. This

is determined by applying the complementary high pass filter (to the low pass filter designed in this section) to the cylinder pressure trace shown in Figure 4.2. The Power Spectral Density of the signal is taken by using Welch's method, a 512 point FFT with a Hamming window with 50% overlap is used. The frequency of the first several modes are also shown for reference.

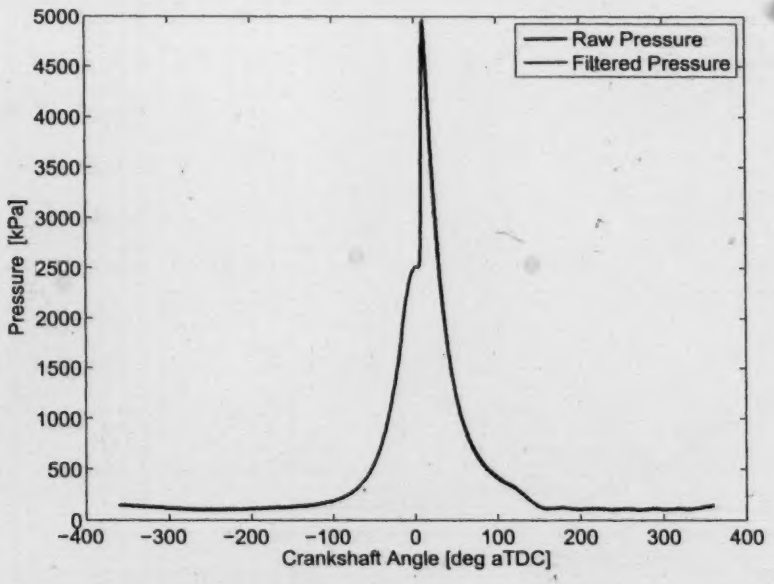

Figure 4.2: Raw and Filtered Pressure Traces for Full Cycle. Test SS27 cycle 155.

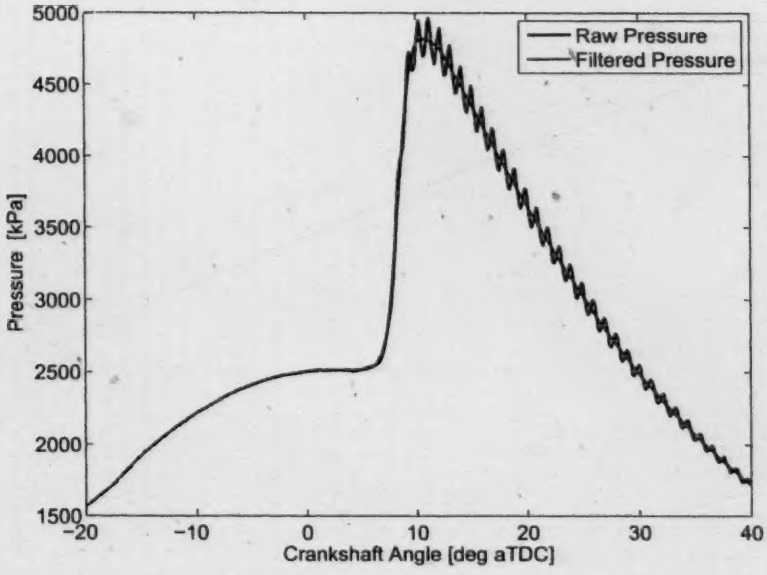

Figure 4.3: Raw and Filtered Pressure Traces Near Combustion Region. Test SS27 cycle 155.

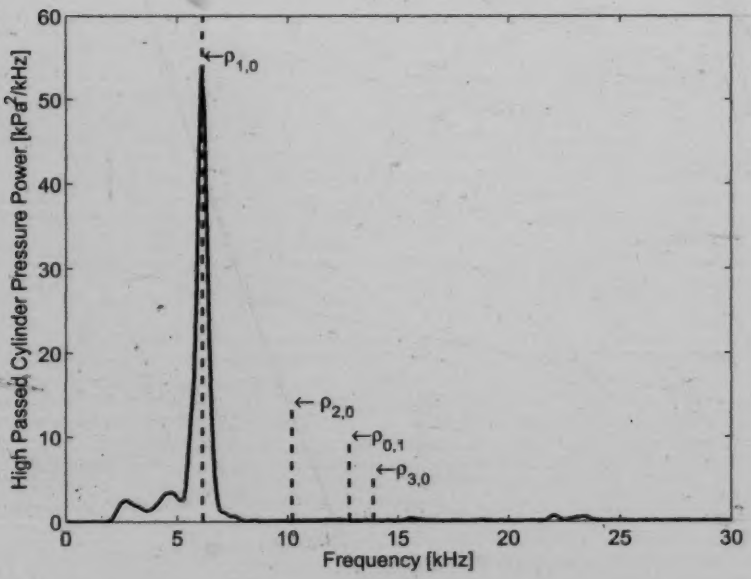

Figure 4.4: Frequency Spectrum of Cylinder Pressure Trace After Applying High Pass Filter Complementary to Low Pass. Test SS27 cycle 155.

4.4.2 Engine Cycle Analysis from In-cylinder Pressure

Each stroke of the 4 stroke cycle is analyzed to estimate the conditions throughout the closed part of the cycle. As the temperature of the cylinder contents is particularly important for HCCI, attention is focused on estimating temperature throughout the cycle. Each individual process in the analysis is detailed below. All processes assume the process as a single zone, with constant temperature and pressure throughout the engine cylinder. Although more complex multi-zone models have been used to estimated temperature, charge, and combustion stratification throughtout the cylinder, [Kongsereeparp and Checkel, 2007, Berntsson and Denbratt, 2007, Sjoberg et al., 2005] these models are beyond the scope of this thesis. The following equations are all solved numerically with the experimental 0.1CAD resolution. The derivatives are estimated with a first order forward difference scheme.

The volume of the engine cylinder throughout the engine cycle is determined from the slider crank mechanism equation, [Heywood, 1988]:

$$V_{cyl} = V_{TDC} + \frac{\pi \times B^2}{4} \times (L + r - r \times \cos(\theta) - \sqrt{L^2 - (r \times \sin(\theta) - x)^2}) \quad (4.3)$$

An engine performance metric that can be obtained with strictly the raw measured in-cylinder pressure trace, along with the cylinder volume, is the IMEP. IMEP is defined as the pressure, which applied to the piston over the engine cycle, would produce the same total work output, as the measured cycle. IMEP is taken over the entire cycle to include any work done to (or by) the piston during the intake and exhaust strokes, giving a complete measure of the indicated work:

$$IMEP = \frac{\oint P dV_{cyl}}{V_{disp}} \quad (4.4)$$

4.4.3 Intake Stroke

The intake stroke is the process from TDC of the exhaust stroke to the point of IVC where the fresh air-fuel mixture is drawn into the cylinder and mixes with residual remaining from the previous cycle. The compositional changes due to the residual are neglected. The effect of neglecting the residual compositional effects in the thermodynamic properties is assumed small, as with the boosted intake manifold pressure, the residual fraction is <10% of the total charge.

To determine the mass of air-fuel charge drawn into the cylinder, the time averaged flow rate of air and the value of λ measured with the UEGO are used. The inducted mass per cycle is:

$$m_{int} = \dot{m}_{air} \frac{120}{N} * \times \left(1 + \frac{1}{(AFR_{stoich}\lambda)}\right) \tag{4.5}$$

Rather than use the measured and estimated fuel flow rates of n-heptane and iso-octane, respectively, Eqn. 4.5 is used as the UEGO can provide a measurement of the Air-Fuel Ratio (AFR) with cycle to cycle response (response time of ~150msec). Since the air-fuel ratios are in the 45-60:1 range, any error associated with the estimation of the fuel mass is assumed to be small as it represents <2% of the total intake flow rate. The mass of mixture trapped in the cylinder at IVC is the sum of m_{int} and m_{res}:

$$m_{cyl} = m_{int} + m_{res} \tag{4.6}$$

4.4.4 Closed Engine Cycle

From IVC to EVO the mass inside the cylinder is considered to be constant. Blowby past the engine piston rings is assumed to be small. The in-cylinder temperature throughout the closed part of the cycle is estimated using Eqn. 4.7:

$$T = \frac{PV_{cyl}}{m_{cyl}R} \tag{4.7}$$

The cylinder mass for each cycle is affected by the residual mass left over from the previous cycle, by Eqn. 4.6. Thus the temperature for each cycle is affected somewhat by this estimated residual mass. This model of the engine cylinder does not take into account any thermal stratification that occurs near the wall surfaces throughout the cylinder, but rather gives a spatially averaged value of the temperature.

To determine the heat energy released by the chemical reactions during the combustion from the in-cylinder pressure the First Law of Thermodynamics is applied to the engine cylinder for the closed part of the cycle:

$$\delta Q_{HR} + \delta Q_{HL} = dU + \delta W + \sum_i h_i dm_i \tag{4.8}$$

Simplifying Eqn. 4.8, by neglecting any mass flow into or out of the cylinder, lumping the heat release term together with the heat loss term, and assuming the only work is boundary work on the piston, the relationship simplifies to:

$$\delta Q_{HR_{net}} = \delta Q_{HR} + \delta Q_{HL} = \frac{\gamma}{\gamma - 1} P \, dV + \frac{1}{\gamma - 1} V \, dP \tag{4.9}$$

Since the heat release and heat loss terms are lumped together, this equation estimates the heat release that does work on the piston, rather than the total heat released from the burned fuel. This form of the First Law is typically called heat release analysis, and is typical of other investigators, [Blair, 1999, Heywood, 1988, Chang et al., 2004].

To estimate the polytropic exponent throughout the engine cycle the fit for highly

diluted mixtures in HCCI engines is used [Chang et al., 2004]:

$$\gamma = -9.967e^{-12}T^3 + 6.207e^{-8}T^2 - 1.436e - 4T + 1.396 \tag{4.10}$$

The authors claim a +/-0.005 error in predicting γ over a range of temperatures (600-2000K) and air-fuel ratios (18-23:1) when compared with a 14 species equilibrium solver. The value of the specific heat of the mixture is calculated as:

$$Cp = \frac{\gamma R}{\gamma - 1} \tag{4.11}$$

Due to the highly air-diluted mixtures used in this study, the mixture is assumed to be air, so the value of $R = 287kJ/(kg \cdot K)$ is used. An empirical fit of the ideal gas constant for lean AFR mixtures is given by [Stone, 1999]. There an error of less than 3% with this empirical fit compared with the ideal gas constant for air, for λ =2.5 for temperatures up to ~1500K. The error is reduced further for increased values of λ as more of the mixture is indeed air.

By taking a cumulative sum of the incremental net heat release throughout the combustion process, the total net heat released during the combustion event can be determined. The total cumulative energy released from the fuel can be found.

$$HR(\theta) = \sum_{\theta=a}^{\theta=b} \delta Q_{HR_{net}} \tag{4.12}$$

The value for 'a' of 20 CAD bTDC is used as no detectable combustion could be seen before this angle in any test. The value of 'b' of 40 CAD aTDC was used as the as no significant combustion past this angle could be seen for any experimental point. Due to the two stage combustion found in this engine, Eqn. 4.12 is also used to determine HR_{LTR} and HR_{HTR}. To determine HR_{LTR}, 'a' is 20 CAD bTDC, and 'b' is taken 5 CAD bTDC. To determine HR_{HTR} 'a' is 5 CAD bTDC and 'b' is 40

CAD aTDC. Thus the heat release for each stage of the combustion, as well as the total combustion process are determined separately.

Since the net heat release estimates the progression of chemical energy released from the fuel, it can also be used to determine the combustion timing. The fractional heat release curve can be determined using:

$$MFB(\theta) = \frac{HR(\theta)}{max(HR)} \tag{4.13}$$

The crankshaft angle for any point along this curve can be then determined using:

$$CAx = \hat{\theta} \quad where : MFB(\hat{\theta}) = x \tag{4.14}$$

The total heat released during the cycle, HR_{tot}, is the maximum of the heat release profile, the denominator of Eqn. 4.13. Similarly this can be applied for the HR_{LTR} and HR_{HTR} heat release curves. In this work $CA5_{HTR}$ is used as the metric for SOC.

4.4.5 Exhaust Stroke and Residual Estimation

To estimate the residual mass and temperature for the proceeding cycle, the in-cylinder temperature and mass must be estimated throughout the blow down process and exhaust strokes. From EVO to BDC of the expansion stroke, where the blowdown process is assumed to be complete, the cylinder temperature is assumed to follow an isentropic expansion [Heywood, 1988]. The temperature thus follows the in-cylinder pressure as:

$$\frac{T(\theta + \Delta\theta)}{T(\theta)} = \left(\frac{P(\theta + \Delta\theta)}{P(\theta)}\right)^{\frac{\gamma-1}{\gamma}} \tag{4.15}$$

The mass of exhaust gas during the exhaust stroke, from BDC to EVC, is estimated using:

$$m_{exh} = \frac{PV_{cyl}}{RT} \tag{4.16}$$

The temperature in Eqn. 4.16 is estimated using the relationship in:

$$\Delta T = \frac{\Delta Q_{HT}}{m_{exh} Cp} \tag{4.17}$$

The residual mass for the next cycle, m_{res} is then estimated as the value of m_{exh} at the point of EVC. The value of ΔQ_{HT} is estimated using the Woschni heat transfer correlation as shown in Heywood, [Heywood, 1988].

The preceding series of equations provide an estimate of the in-cylinder temperature throughout each engine cycle. To provide validation for the analyzed data, a direct comparison with an experimentally measured temperature is necessary. The exhaust gas temperature measured in the exhaust port provides a means of validating the estimated temperature. In Figure 4.5 the test average of 450 cycles of the mean exhaust gas temperature during the blowdown and exhaust strokes (as estimated by the post processing analysis) is compared with the measured exhaust gas temperature. As shown in Figure 4.5, for exhaust gas temperatures of 370°C the mean in-cylinder exhaust gas temperature is estimated to be approximately 80°C higher. For exhaust gas temperatures near 200°C the estimated mean in-cylinder temperature is nearly equivalent. In [Heywood, 1988], Heywood suggests that the time averaged in-cylinder temperature, during the blowdown and exhaust strokes is approximately 100°C greater than the measured exhaust gas temperature for an SI engine, with exhaust gas temperatures of 500-800°C. With the reduced exhaust gas temperatures of HCCI operation, heat transfer from the exhaust gases to the exhaust port is reduced. This effect becomes even more apparent at the lowest exhaust gas temperatures, which show similar values between the measured exhaust gas temper-

ature, and the in-cylinder average temperature. The linear fit between the estimated temperature and the measured temperature shown in Figure 4.5 has an average error of $13°C$ and a maximum error of $40°C$.

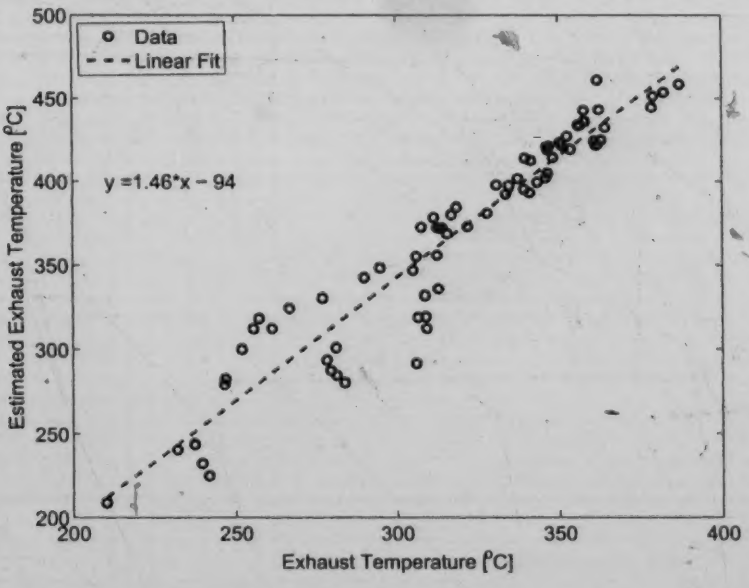

Figure 4.5: Estimated Exhaust Gas Temperature vs. Measured Exhaust Gas Temperature of Tests SS1-SS75

Examples of the pressure traces and heat release rates typical for this engine are shown in Figure 4.6 and 4.7. Figure 4.6 shows 10 consecutive pressure traces for each of 3 loads at a given operating condition. In Figure 4.7 the heat release rates for each of pressure traces in Figure 4.7 is presented. A typical heat release profile with the relevant combustion timing metrics used in this study is shown in Figure 4.8. The LTR and HTR reaction zones are also labeled in both Figure 4.7 and 4.8. Throughout this study the metric used for SOC is $CA5_{HTR}$ as using the value of $CA10$ as in [Atkins, 2004], results in SOC being predicted sporadically in the LTR zone due to the high HR_{LTR}. This is caused by the low octane number

used in several of the tests. This can be seen visually in Figure 4.8, as in several cases the flat region of heat release between the end of the LTR zone and the start of the HTR zone, occurs at nearly 10% of the total heat release. The metric used to determine the end of combustion is $CA90$ as in [Oakley et al., 2001, Atkins, 2004] as it generally predicts the end of the fast combustion processes before heat transfer effects, and slowing reaction rates sharply decline the heat release rate.

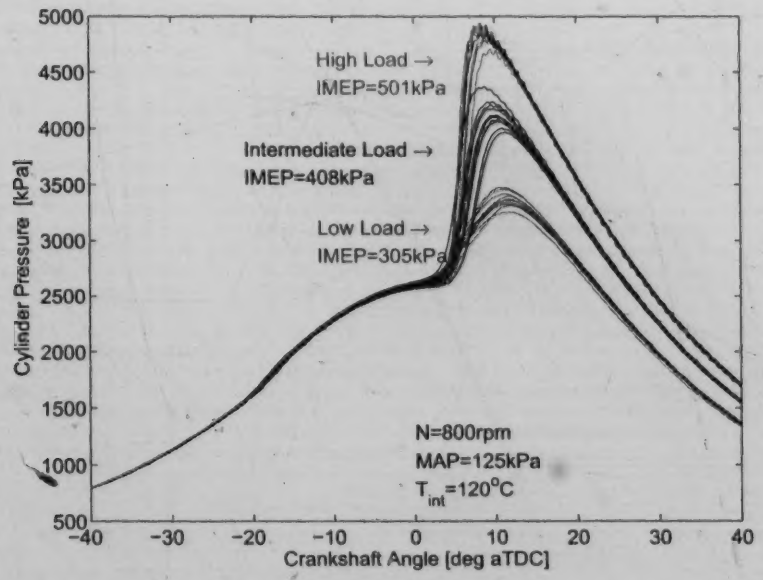

Figure 4.6: Cylinder Pressure for Three Loads with Ten Cycles for each Load. Cycles 1-10 of tests SS58-SS60.

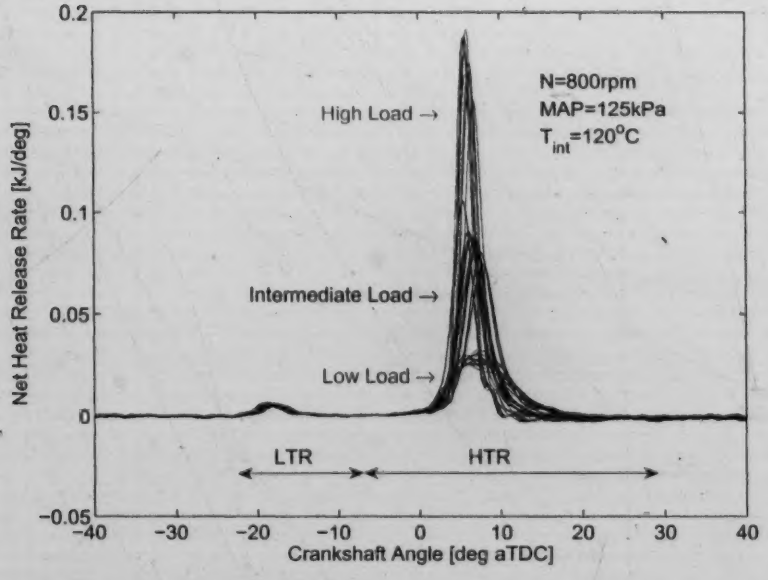

Figure 4.7: Heat Release Rate for Three Loads with Ten Cycles for each Load. Cycles 1-10 of tests SS58-SS60.

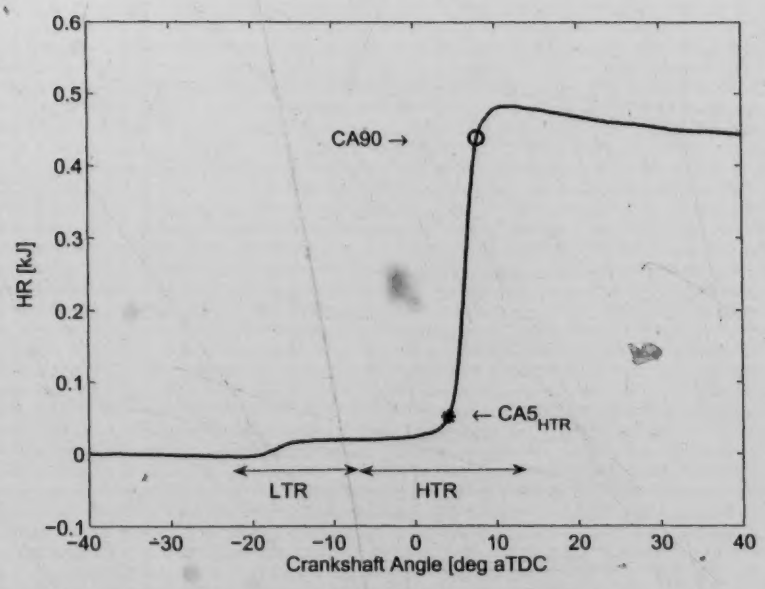

Figure 4.8: Typical Heat Release profile

4.4.6 Uncertainty in Analysis

To understand the effects of uncertainty of the measured and estimated values on the results of the post processing presented in this chapter, an uncertainty analysis is performed on the collected experimental data. As the main measurement of interest for this study is a selection of metrics based on the in-cylinder pressure trace, so the focus of this section will mainly be on these parameters. The parameters evaluated from the cycle analysis based on the pressure trace can be summarized into heat release parameters, combustion timing parameters (derived from the HR analysis), estimated temperatures, and IMEP. To evaluate these parameters the required inputs are the geometric properties of the engine and measured thermodynamic states of the intake, in-cylinder, and exhaust conditions of the engine.

Based on the procedure of a systematic perturbation of the inputs necessary in calculating the result is done in order to determine the effect of each input error on the output [Moffat, 1988]. Each measured input parameter has some error associated with its value. A list of the necessary input parameters in calculating the results presented in this chapter is shown in Table 4.8 along with the estimated uncertainty associated with that parameter. Parameters marked with an '*' are parameters which are estimated during the analysis or before the analysis.

To reduce the number of inputs to be evaluated, a previous analysis is used to eliminate insignificant sources of error [Payri et al., 2006]. The authors found that the errors associated with the dimensional measurements, and deformation of these dimensions due to combustion pressures to be negligible, even for a high compression ratio diesel engine. As the engine in this thesis uses a relatively low compression ratio, the effects of inaccuracy of these dimensions is ignored. While the valve event angles are critical to engine performance, they have little effect on the analysis techniques used in this work, as air and fuel flow rates are measured, rather than estimated using

Parameter	Value	Uncertainty (±)
B [m]	0.080	0.001
S [m]	0.089	0.001
L [m]	0.159	0.001
V_{TDC} [m^3]	4.98e-5	0.05e-5
IVO [CAD bTDC]	8	2
IVC [CAD aBDC]	52	2
EVO [CAD bBDC]	69	2
EVC [CAD aTDC]	1	2
T_{int} [°C]	64-141	2
N [rpm]	800-1200	10
λ [-]	1.8-3.5	1%
$\dot{m}_{air}$ [g/sec]	3.1-4.2	5%
$\dot{m}_{fuel}$ [g/sec]	0.054-0.134	3%
m_{res} [mg/cycle]*	44-58	10%
T [Nm]	5.2-16.9	0.1
O_2 [%]	9.1-15.1	0.01
CO_2 [%]	2.3-7.0	0.01
CO [%]	0.08-1.21	0.01
UHC [ppm]	2.0e3-4.7e3	10
NO_x [ppm]	0-23	1
T_{wall} [°C]*	110	30
γ [-]*	1.27-1.35	0.005

Table 4.7: Summary of Measured Inputs and Estimated Uncertainty. Parameters with a '*' are estimated.

a flow model based on valve events. The emissions measurements have no influence on the estimated combustion parameters, however their resolution is shown in Table 4.8 for completeness.

The error in $\dot{m}_{air}$ is estimated from the laminar airflow measurement technique's individual error sources. The uncertainty in $\dot{m}_f$ is derived from the average standard deviation of measured n-heptane flow rate for each test case. The value of m_{res} is determined from the estimated in-cylinder conditions at EVC for each cycle. Since it is not a measured quantity, the error associated with it is given a relatively large, 10% uncertainty. Combining these errors to give the total uncertainty in the cylinder mass, is done using:

$$\delta m_{cyl} = \delta m_{air} + \overline{AFR}\delta m_{fuel} + \overline{f_r}\delta m_{res} \tag{4.18}$$

Note: in this equation, the values of the flow rates $\dot{m}_{fuel}$ and $\dot{m}_{air}$ are converted to a mass/cycle basis, m_{fuel} and m_{air}, using an engine speed of 1000rpm. Since the total uncertainty in $\dot{m}_{fuel}$ and m_{res} only contribute to the total cylinder mass through the AFR and f_r, respectively, their effects are reduced. Here the average values of AFR and f_r of 35:1, and 10% are used. Combining the errors, the total error in m_{cyl} is estimated at 7%. This estimated error is similar to the 6% error in m_{air} estimated by [Payri et al., 2006].

Pertinent to this study, the main factors which contribute the errors in the evaluation of combustion metrics, according to [Payri et al., 2006], are the estimates of in-cylinder mass during the closed cycle, the cylinder pressure pegging pressure, and the crankshaft encoder offset error. Also included, is the effect of the estimation of the ratio of specific heats, γ as this is estimated using a fit [Chang et al., 2004]. The only factor which effects evaluation of IMEP from the cylinder pressure trace is the accuracy of the relationship between the crankshaft angle encoder and the actual angle of TDC [Payri et al., 2006]. Offsetting this value from the true value results in an offset of the cylinder volume calculation shown in Eqn. 4.4.

To evaluate the influence of error in these parameters, three test points are evaluated with each of the inputs perturbed by the uncertainty shown in Table 4.8. Parameter θ_{offset} is used to show the effect of improperly estimating the actual relationship of the crankshaft with the in-cylinder pressure trace. Input parameter $P_{pegging}$ is used to show the effects of a bias in the pegging of the relative in-cylinder pressure to an absolute pressure source. The tests SS16, SS17, and SS19 are from the steady state tests shown in Table 4.3 at an engine speed of 1000rpm, MAP of 125kPa, T_{int} of 90°C for min, med and max loads are used as a representative set of tests. The

results shown in Table 4.8 are the average of the values of the three test points. The average of the nominal cases, where the input values use their as measured values, is also shown for reference. Of the input parameters to this uncertainty test, Table 4.8 shows that m_{cyl} has the greatest effect on properly estimating temperature, though other sources of error can contribute significantly as well. The only parameter which significantly affects determining the combustion timing, $CA5_{HTR}$ and $CA90$, is the direct offset of the encoder through θ_{offset}. The other parameters have a negligible effect (less than the 0.1CAD resolution of the analysis) on the MFB curve. It should be noted that all of the input parameters have an effect on $\frac{\Delta P}{\Delta \theta}$, but the effect is typically under 5%. The only factor investigated which contributes to an error in estimating IMEP is crankshaft encoder offset. Even the relatively small change in offset of 0.5CAD results in an average error of about 4% in the IMEP.

	Nominal Values	m_{cyl} +7%	θ_{offset} +0.5CAD	γ +0.005	$P_{pegging}$ +20kPa
T_{IVC} [K]	386.9	386.2	387.0	386.9	388.8
T_{max} [K]	1586	1484	1566	1586	1575
$CA5_{HTR}$ [CAD]	6.1	6.1	6.3	6.1	6.1
$\frac{\Delta P}{\Delta \theta}$ [kPa/CAD]	161	166	194	168	186
IMEP [kPa]	482	482	466	482	482

Table 4.8: Summary of Input Error on Analyzed Results. Nominal values are the average of Tests SS16, SS17, and SS18.

Chapter 5

Experimental Results

The analysis of the experimental data is presented in this chapter. First the repeatability of the experiment is investigated. Then the process for determining the optimum combustion timing for the range operating conditions is explained. Then performance metrics of the steady state operating conditions are shown. These metrics include global engine parameters, emissions characteristics, and HCCI knock characteristics. Finally the results of the transient tests and SI to HCCI mode switching tests are presented.

5.1 Experimental Uncertainty

To determine the repeatability of the experimental apparatus, 15 of the 75 steady state tests were taken on 5 separate occasions. The 15 tests represent a range of the experimental test conditions shown in Table 4.3. The tests for which additional trials were taken are shown in Table 4.4. Compared with the full matrix of steady state points of Table 4.3, the repeated trials cover the same range of conditions, with the exception of one value of T_{int} for each test condition.

To determine the repeatability of the experimental setup, the performance metrics of each of the 5 trials for the 15 repeated tests are calculated. Several of the important metrics of the engine are summarized in terms of their mean and standard deviation

within the repeated trials. The results for each test case are shown in Tables 5.1 -5.5. A summary of the results of these 5 tables is shown in Table 5.6. The average standard deviation is the average (either absolute value or percentage) from each of the 15 test cases. The maximum standard deviation is the maximum of the standard deviation from each of of the 15 test cases.

Parameter	Min. Load	Med Load	Max. Load
T_{int} [K]	120.8 (0.5)	120.5 (0.8)	120.5 (1.0)
MAP [kPa]	125.0 (0.18)	125.0 (0.17)	125.2 (0.19)
$CA5_{HTR}$ [CAD]	3.4 (0.43)	4.2 (0.52)	4.2 (0.66)
HR_{tot} [kJ]	0.287 (0.028)	0.402 (0.018)	0.522 (0.019)
IMEP [kPa]	314 (27.7)	429 (17.7)	531 (16.8)
λ [%]	3.4 (0.11)	2.75 (0.067)	2.19 (0.05)
$\dot{m}_{air}$ [g/sec]	3.08 (0.033)	3.08 (0.034)	3.07 (0.037)
$\dot{m}_{heptane}$[%]	0.037 (0.001)	0.036 (0.001)	0.035 (0.001)
T_{IVC} [K]	394.6 (0.1)	395.2 (0.3)	395.8 (0.4)
T_{max} [K]	1321 (68)	1572 (53)	1835 (57)
$BSFC$ [g/kWhr]	380 (53)	286 (12)	270(4)
CO [% of CO]	0.41 (0.28)	0.14 (0.05)	0.06 (0.02)
UHC [ppm]	2105 (1081)	1710 (839)	1409 (769)
NO_x [ppm]	1.3 (0.3)	1.2 (0.3)	2.8 (2.6)

Table 5.1: Average and Standard Deviation (in brackets) of 5 Repeated Trials for Case N of Table 4.4.

The first two parameters in Table 5.6, T_{int} and MAP, represent the ability to repeat the operating condition of the engine for each trial. Of the parameters of Table 5.6 the SOC, as measured by $CA5_{HTR}$, is a parameter that is sensitive to the overall similarity of the engine operating condition from trial to trial. Variations in fuel delivered, T_{int} , MAP, N, and residual fraction will all influence the SOC. This relatively small variation in $CA5_{HTR}$ is promising as even this sensitive parameter can be reliably repeated. One of the major reasons for the repeatability of $CA5_{HTR}$, is the relatively small variation in T_{IVC} from trial to trial. As the auto-ignition process is highly sensitive to temperature, having a low variation in T_{IVC} means there is likely low variation in temperature throughout the compression process. The results show

Parameter	Min. Load	Med Load	Max. Load
T_{int} [K]	109.7 (1.5)	109.2 (1.5)	108.9 (1.4)
MAP [kPa]	124.8 (0.14)	124.7 (0.18)	124.9 (0.23)
$CA5_{HTR}$ [CAD]	4.0 (0.85)	5.0 (0.70	6.1 (0.15)
HR_{tot} [kJ]	0.334 (0.028)	0.452 (0.023)	0.565 (0.013)
IMEP [kPa]	362 (30)	477 (20)	571 (10)
λ [%]	3.0 (0.11)	2.5 (0.07)	2.0 (0.02)
$\dot{m}_{air}$ [g/sec]	3.71 (0.030)	3.71 (0.024)	3.69 (0.022)
$\dot{m}_{heptane}$[%]	0.066 (0.002)	0.064 (0.001)	0.060 (0.001)
T_{IVC} [K]	392.7 (0.4)	393.8 (0.5)	393.9 (0.5)
T_{max} [K]	1417 (96)	1677 (74)	1917 (46)
$BSFC$ [g/kWhr]	309 (35)	249 (8)	244 (2)
CO [% of CO]	0.35 (0.23)	0.12 (0.05)	0.06 (0.02)
UHC [ppm]	2130 (1044)	1721 (686)	1395 (547)
NO_x [ppm]	1.5 (0.2)	1.5 (0.2)	13.7 (5.9)

Table 5.2: Average and Standard Deviation (in brackets) of 5 Repeated Trials for Case O of Table 4.4.

that the deviation of T_{IVC} is considerably smaller than that of T_{int}. As T_{int} directly influences T_{IVC}, the heat transfer during the intake stroke appears to play a role in reducing these variations. Heat transfer between the fresh intake charge, at T_{int}, and the intake port, intake valve, and in-cylinder surfaces during the intake stroke appear to regulate the variations in the intake temperature. The variations in T_{max} represent a relatively small variation on the average peak combustion temperatures of 1300-1900K.

The variability of HR_{tot} and IMEP are both of similar magnitude, as should be expected, as they are both measures of the energy release associated with the combustion process. The variation in HR_{tot} is slightly higher than IMEP, as it also influenced by variations in the estimated temperature, which in turn influences the estimated value of γ, while the IMEP is only reliant on the pressure signal. The variations in HR_{tot} and IMEP are at least partially caused by the variation in fuel flow rate, measured by the changes in $\dot{m}_{heptane}$, as changes in fuel flow rate directly influence the energy available for combustion. The variability of total fuel flow rate

Parameter	Min. Load	Med Load	Max. Load
T_{int} [K]	91.4 (1.7)	91.9 (1.6)	92.2 (1.6)
MAP [kPa]	124.9 (0.33)	124.9 (0.39)	125.0 (0.39)
$CA5_{HTR}$ [CAD]	6.6 (0.31)	7.0 (0.48)	7.5(0.81)
HR_{tot} [kJ]	0.411 (0.009)	0.470 (0.022)	0.555 (0.021)
IMEP [kPa]	442 (10)	499 (21)	568 (133)
λ [%]	2.6 (0.05)	2.3 (0.09)	2.0 (0.05)
$\dot{m}_{air}$ [g/sec]	4.32 (0.034)	4.31 (0.031)	4.29 (0.031)
$\dot{m}_{heptane}$[%]	0.108 (0.002)	0.107 (0.001)	0.105 (0.001)
T_{IVC} [K]	388.2 (0.7)	388.8 (0.5)	389.4 (0.5)
T_{max} [K]	1545 (23)	1686 (46)	1878 (60)
$BSFC$ [g/kWhr]	279 (5)	263 (13)	250 (7)
CO [% of CO]	0.19 (0.06)	0.13 (0.05)	0.08 (0.03)
UHC [ppm]	1887 (683)	1681 (644)	1391 (586)
NO_x [ppm]	1.7 (0.2)	1.7 (0.2)	5.4 (5.2)

Table 5.3: Average and Standard Deviation (in brackets) of 5 Repeated Trials for Case P of Table 4.4.

(including both n-heptane and iso-octane) can only be estimated, as the flow rate of only n-heptane is measured, and the flow rate of iso-octane estimated from PW_{octane}. Since the pulse width's are maintained constant for all trials, the variations in flow rate are likely due to changes in injector flow constants (for example due to changes in supplied voltage to the fuel injectors), and fuel pressure. Assuming equal flow rates and variability of n-heptane and iso-octane flow rates, the error associated with the total fuel flow rate, $\dot{m}_{fuel}$, is 2.8% by taking the root sum of squares of the errors. This total error in fuel flow rate assumes that the errors of n-heptane and iso-octane flow rates are assumed to be random and uncorrelated with each other. The value of variation in λ , as measured by the UEGO, can be determined to be a combination of the variations in $\dot{m}_{air}$ and $\dot{m}_{fuel}$ (as determined previously), by determining the sum of these errors in a root sum of squares, [Moffat, 1988]. As the AFR is related directly to λ through the AFR_{stoich} (which is assumed to have no error, and thus has no effect in the total error), the total error can be determined by a root sum of squares for a purely multiplicative equation. The total average error associated with

Parameter	Min. Load	Med Load	Max. Load
T_{int} [K]	99.6 (1.3)	98.6 (1.7)	98.1 (2.2)
MAP [kPa]	109.8 (0.17)	109.9 (0.26)	101.0 (0.33)
$CA5_{HTR}$ [CAD]	4.3 (0.92)	4.9 (0.72)	6.2 (0.50)
HR_{tot} [kJ]	0.360 (0.016)	0.419 (0.027)	0.505 (0.015)
IMEP [kPa]	375 (15)	429 (24)	498 (16)
λ [%]	2.6 (0.05)	2.3 (0.12)	1.9 (0.04)
$\dot{m}_{air}$ [g/sec]	3.25 (0.022)	3.24 (0.023)	3.23 (0.026)
$\dot{m}_{heptane}$[%]	0.077 (0.002)	0.077 (0.001)	0.075 (0.001)
T_{IVC} [K]	390.6 (0.6)	390.7 (0.8)	391.1 (0.9)
T_{max} [K]	1575 (59)	1716 (67)	1915 (36)
$BSFC$ [g/kWhr]	293 (9)	312 (29)	258 (7)
CO [% of CO]	0.16 (0.07)	0.11 (0.05)	0.06 (0.02)
UHC [ppm]	1780 (747)	1655 (700)	1308 (510)
NO_x [ppm]	1.5 (0.3)	1.5 (0.3)	7.6 (3.3)

Table 5.4: Average and Standard Deviation (in brackets) of 5 Repeated Trials for Case Q of Table 4.4.

the mass and fuel flow rates is 3.0%, which accounts for the majority of the variation associated with the mean variation in the measurement of λ .

Variability in the emissions measurements is also shown in Table 5.6. The results are shown in absolute terms, rather than on a percentage of the mean value, as this result could be misleading. The average standard deviation of the mean value over the repeated trials of the CO measurement is 0.09% CO on a mean value of CO of 0.16% CO. While this represents a larger percentage variation (56%) in absolute terms, the absolute error is relatively small, as 0.09% error is only a small fraction of the range of the analyzer (0-10%). Also, as the CO produced by the engine changes nearly two orders of magnitude over the range of λ of this study, even a small change in λ from test to test results in a significant change in CO. Similarly for the NO_x measurement, the average standard deviation of the mean value over the repeated trials is 2.1ppm, with a mean value of 3.7ppm. In percentage terms this is a large variation (57%), although in absolute terms this is a very small quantity, especially over the 0-2500ppm range of the analyzer. The measurement of unburned

Parameter	Min. Load	Med Load	Max. Load
T_{int} [K]	140.0 (0.9)	140.0 (1.2)	140.1 (0.9)
MAP [kPa]	140.1 (0.23)	139.9 (0.37)	139.2 (1.31)
$CA5_{HTR}$ [CAD]	4.0 (0.83)	5.0 (0.71)	6.1 (0.47)
HR_{tot} [kJ]	0.326 (0.026)	0.477 (0.016)	0.573 (0.026)
IMEP [kPa]	365 (29)	513 (15)	589 (23)
λ [%]	3.3 (0.09)	2.5 (0.06)	2.1 (0.03)
$\dot{m}_{air}$ [g/sec]	3.99 (0.050)	3.98 (0.062)	3.96 (0.065)
$\dot{m}_{heptane}$[%]	0.045 (0.001)	0.044 (0.001)	0.042 (0.001)
T_{IVC} [K]	402.9 (0.3)	403.9 (0.4)	404.4 (0.1)
T_{max} [K]	1386 (67)	1702 (30)	1885 (58)
$BSFC$ [g/kWhr]	297 (33)	242 (8)	245 (5)
CO [% of CO]	0.43 (0.2)	0.11 (0.04)	0.07 (0.02)
UHC [ppm]	2626 (1253)	2319 (852)	2270 (783)
NO_x [ppm]	1.4 (0.3)	1.4 (0.5)	9.2 (5.9)

Table 5.5: Average and Standard Deviation (in brackets) of 5 Repeated Trials for Case R of Table 4.4.

hydrocarbons (UHC) has an average standard deviation over the repeated trials of 864ppm with an mean value of 1.82e+3ppm. This does represent a significant amount of variation in the measurement, of 47%. The large variation in UHC is likely coupled with the variation in CO, as a small decrease in the in-cylinder temperature, from trial to trial, could significantly reduce oxidation of the CO as well as the UHC. This effect is the strongest near the misfire limit, when in-cylinder temperatures are low and especially near the cylinder walls, where gas temperatures are reduced even further by heat transfer to the wall. As the engine is operated at the misfire and knock limits to determine the minimum and maximum load output of the engine, at a given operating condition, the combustion is near its limit in both cases. As the misfire limit is approached, CO and UHC emissions increase significantly, especially if a partial or complete misfire occurs on any particular cycle. Thus even a small change in the operating condition leads to a large variation in the measured quantity. Similarly for the knock limit, a small change in operating condition from one trial to another can lead to a large increase in NO_x emissions. This is particularly true, as the

Parameter	Average Std. Dev.	Maximum Std. Dev.
T_{int} [K]	1.5	2.5
MAP [%]	0.2	0.3
$CA5_{HTR}$ [CAD]	0.68	1.0
HR_{tot} [%]	5.6	11
IMEP [%]	5.1	9.9
λ [%]	3.4	10.2
$\dot{m}_{air}$ [%]	1.1	1.8
$\dot{m}_{heptane}$[%]	2.0	3.2
T_{IVC} [K]	0.54	1.1
T_{max} [K]	64	107
$BSFC$ [%]	5.7	15.7
CO [% of CO]	0.09	0.29
UHC [ppm]	$8.6x10^2$	$1.4x10^3$
NO_x [ppm]	2.1	6

Table 5.6: Average and Maximum Standard Deviations of Performance Metrics for all Repeated Trials

value of T_{max} approaches the threshold for production of thermal NO_x, which happens to coincide with the knock limit of this engine. At the knock limit, an increase in the average T_{max} of the 107K shown in Table 5.6 results in approximately an order of magnitude increase in the rate of initial NO formation according to [Heywood, 1988]. It should be noted that while the sensitivity of the emissions parameters are high at the limits of combustion, the absolute values, the absolute values remain relatively small.

5.2 Determination of Optimum Combustion Timing

Shown in Figure 5.1 is the average combustion timing as a function of intake temperature for the three engine speeds. The error bars in Figure 5.1 show ±1 standard deviation of the combustion timing for the 450 cycles collected. The trend line through the data points is a quadratic fit to the mean combustion timing. For each engine speed, as the intake temperature increases, the combustion timing advances. The variation of the combustion timing, in CAD, is reduced as combustion advances toward TDC for $CA5_{HTR}$ aTDC. A more complete analysis of the variations of combustion timing for this engine can be found in [Shahbakhti et al., 2007a, Shahbakhti et al., 2007b].

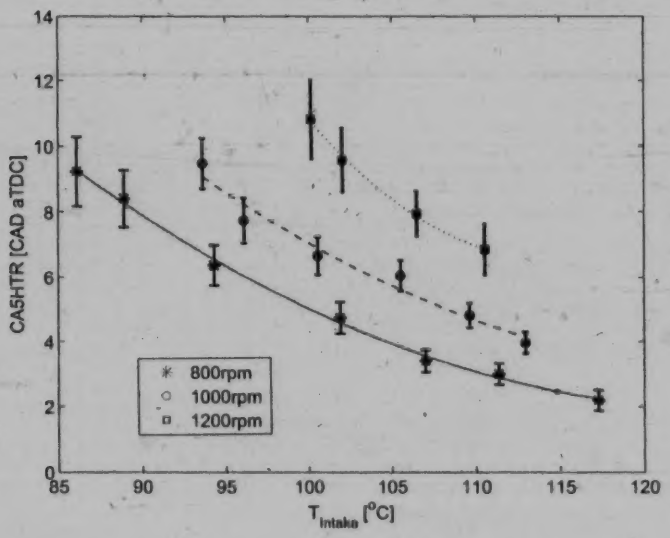

Figure 5.1: Effect of Intake Temperature on SOC for Cases A, B, and C in Table 4.2

In Figure 5.2 the value of $\frac{\Delta P}{\Delta \theta}$ (see Eqn. 5.6) is shown as a function of the SOC. As the combustion timing advances, the value of $\frac{\Delta P}{\Delta \theta}$ increases as engine speed increases. The error bars in this plot show ±1 standard deviation of the value of $\frac{\Delta P}{\Delta \theta}$, with the fitted line a quadratic fit through the data. As knock and mechanical engine damage

can occur for high values of $\frac{\Delta P}{\Delta \theta}$, retarding the combustion timing can be used to prevent this damage. As the high load limit is generally defined by the onset of knock, retarding the combustion timing is one way to achieve higher load, before the onset of knock.

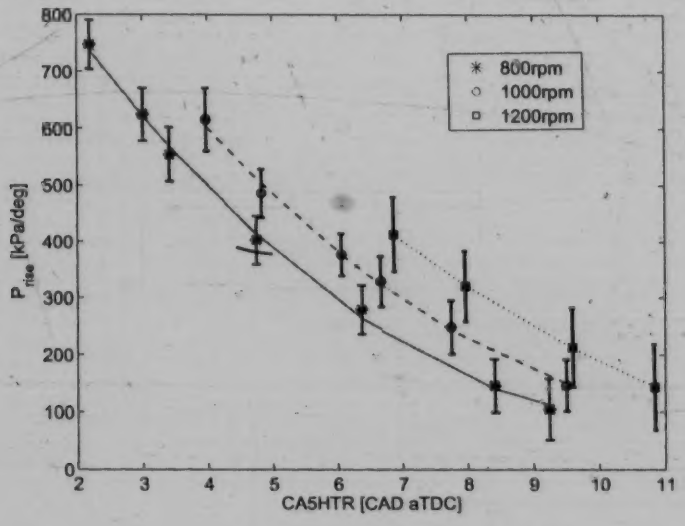

Figure 5.2: Effect of average SOC on Combustion Pressure Rise Rate for Cases A, B and C in Table 4.2

The optimum combustion timing is defined to maximize the power output of the engine. As the fuel input is the same throughout each sweep, the SOC that gives the highest IMEP is therefore the optimum. In Figure 5.3 the value of IMEP is shown as a function of SOC for each engine speed. The error bars are ± 1 standard deviation of IMEP for the 450 cycles of each test. The trend line is a quadratic fit to the data to determine combustion timing which achieves a maximum IMEP. For each engine speed IMEP reaches a maximum at a different combustion timing. As engine speed advances the optimum combustion timing retards from TDC. From these data, the setpoint for combustion timing for each engine speed is set at 5CAD aTDC for

800rpm, 7CAD aTDC for 1000rpm, and 9CAD aTDC for 1200rpm. One possible reason the optimum combustion retards with increasing engine speed is a combination of increased negative work induced by the LTR (caused by the increased n-heptane required at higher engine speed) and the effect of knocking combustion. The knocking combustion increases the heat transfer to the cylinder walls, reducing the work extracted during the expansion stroke [Atkins, 2004, Tsurushima et al., 2002]. The variations in IMEP can also be seen to increase significantly as the combustion is retarded, for all engine speeds.

The mechanism for this increased variation can be explained as follows: as the piston compresses the air-fuel mixture the mixture temperature increases, causing the cylinder contents begin to reacting near TDC. As the piston passes TDC, the piston begins to expand the mixture (since all combustion timings in this work occur aTDC the main combustion event always beings aTDC) and the temperature beings to decrease. The decreasing temperature slows the rate of the auto-ignition process, lengthening the time for the mixture to enter the thermal runaway stage of combustion. As the rate of the chemical kinetics decrease exponentially with reduced temperature, any cycle to cycle differences in the mixture temperature at TDC, result in significantly varying reaction rates as the piston descends. A cycle with a relatively high mixture temperature at TDC, will be somewhat less unaffected by the piston descending. However, a cycle with a relatively low temperature at TDC, will have its rate of reaction significantly reduced by the reduced temperatures aTDC.

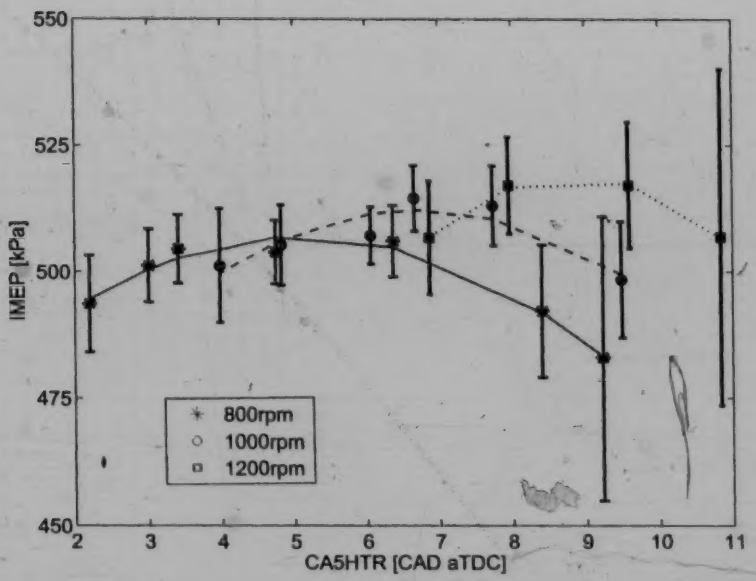

Figure 5.3: Effect of SOC on IMEP for Cases A, B, and C in Table 4.2

5.3 Steady State Results

5.3.1 HCCI Load Range

The steady state engine operating points shown in Table 4.3 are analyzed using the methods described in Section 4.4 and presented here. The test cases in this section are divided into two categories. Cases E, G, and H from Table 4.3 are used in instances where three engine speeds are compared. Cases D, E, and F from Table 4.3 are used to compare three values of MAP. Unless otherwise noted, the values presented in this section are the mean value of 450 engine cycles at one operating point.

The brake work of the engine is the indicated work done on the piston by the combustion pressures minus the frictional losses, and is measured by the engine torque output on the dynamometer. A comparison of IMEP (Eqn. 4.4) vs BMEP (Eqn. 3.3)is shown in Figure 5.4, as is a linear fit to the data. The error bars represent ± 1 standard deviation of the IMEP for each test case. The average value of the standard deviation in BMEP, for tests SS1-SS75, is 27kPa. As the load decreases toward the misfire (low load) limit, the variation in IMEP increases (size of error bars increases). For these low load cases the likelihood of a misfire, or a partial burn cycle increases, increasing the variability of energy released during combustion on any given cycle. The offset between the IMEP and BMEP is the average Frictional Mean Effective Pressure (FMEP). The slope of the linear regression line is not exactly 1, as would be expected if the frictional work were constant through all tests. As the linear fit in Figure 5.4 does not take into account this change in FMEP from test case to test case, deviations from the linear fit result.

The value of the average FMEP of 126kPa is comparable to the estimate by [Blair, 1999], of 135kPa which is typical for an engine of this displacement. Motoring tests over the same range of conditions of the steady state tests result in FMEP of 132kPa. The differences in the two frictional estimates are that the thermodynamic

properties of the gases present in the cylinder during the motoring tests change, [Heywood, 1988]. In particular during the blow down and exhaust phases of the cycle, the pumping work is changed. Different component temperatures during motoring or firing operation (piston and cylinder liner) result in different frictional characteristics between the components.

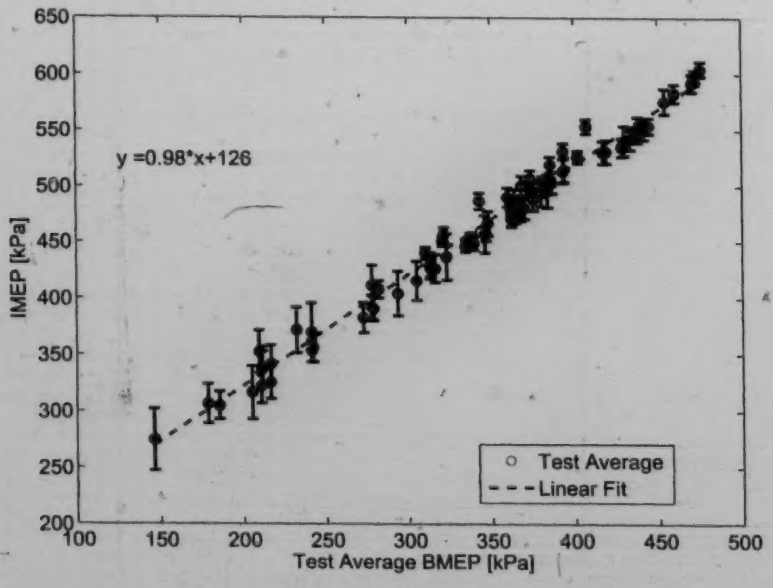

Figure 5.4: IMEP vs BMEP for Cases D, E, F, G, and H of Table 4.3

The load range which can be obtained by varying the fueling (both ON and fuel quantity) in steady state operation are shown in Figures 5.5 and 5.6. The lower line for each MAP indicates the low load limit, the upper line represents the high load limit, and the vertical lines are shown to visually distinguish the individual ranges. In Figure 5.5 the load range for the three values of MAP can be seen, as a function of T_{int}. Increasing the MAP increases the possible load range, extending the maximum load possible. The low load limit can be seen to vary most significantly with the T_{int}, increasing significantly for lower values of T_{int}. For this engine the low load limit is

expanded considerably by increasing the T_{int} from $63°C$ to $100°C$. A similar trend is shown in [Dec and Sjoberg, 2003].

The load range is plotted versus engine speed in Figure 5.6 and the main shift in the load range is to the low load limit. The minimum load which can be obtained increases with engine speed; this result is different from the work presented by other investigators, such as [Hyvonen et al., 2003, Chang et al., 2006], which show decreasing minimum load as engine speed increases. This is attributed to the other investigators using internal EGR [Chang et al., 2006], or variable compression ratio [Hyvonen et al., 2003] to maintain combustion timing with increasing engine speed, rather than changing fuel composition as done here. As engine speed increases the time available for the auto-ignition process to occur decreases; however, the ignition delay time of the fuel remains the same. The most direct way to get reasonable combustion timing as engine speed increases is to decrease the ignition delay time by increasing the compression temperatures. By using a progressively higher internal residual with higher engine speed, as in [Hyvonen et al., 2003], or by increasing compression ratio, as in [Chang et al., 2006], the average in-cylinder temperature during compression is increased, and thus the combustion timing can be advanced sufficiently. Since in this work the residual fraction is relatively small, the method of getting the desired combustion timing as engine speed increases, is to increase the fuel concentration, namely n-heptane. Increasing the fueling reduces the fuel ignition delay by increasing the fuel concentration; however, increased fuel quantity directly results in a higher load.

5.3.2 Fueling Required for HCCI

For the range of operating conditions tested the ON required to maintain stable HCCI operation within the defined operating region of Section 4.2 is shown in Figures 5.7 and 5.8. The points for minimum and maximum load are shown in each figure.

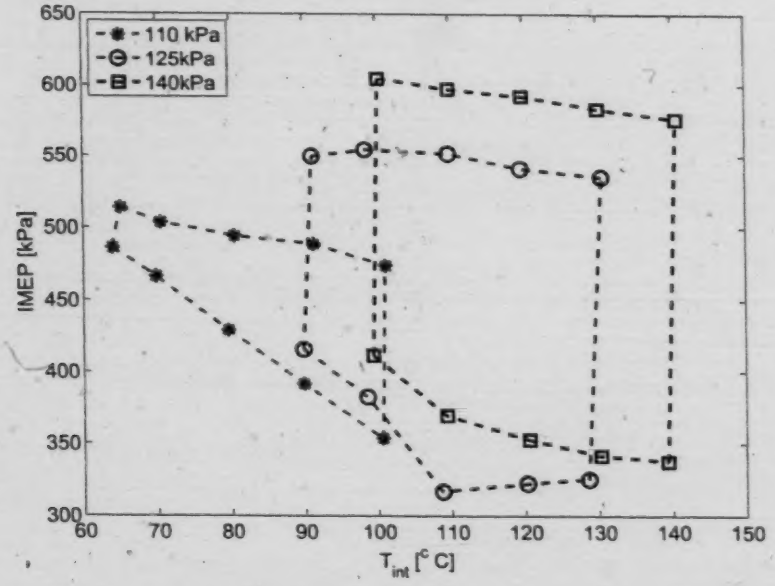

Figure 5.5: Load Range in terms of IMEP vs T_{int} for three values of MAP at 1000rpm. Minimum and maximum load limits shown for Cases D, E and F of Table 4.3

The dashed lines represent the minimum load cases, while the dotted lines represent the maximum load case. To maintain constant combustion timing, as engine speed increases, the ON decreases. This is due to the reduced time available for combustion as the engine speed increases, thus decreasing the available time for the fuel to auto-ignite during compression. As the kinetics of the fuel are based on the time available at the elevated compression temperatures near TDC, a higher engine speed means there is less time for the reactions leading to auto-ignition to occur. Thus a fuel which more easily auto-ignites is required as engine speed increases. The jump in octane in Figure 5.7 between 100-110 $°C$ for the 1200rpm case is due to the imposed threshold of PW_{octane} of 0 to 1.3msec due to the injector. Similarly in Figure 5.8 for MAP of 110kPa the minimum load condition is achieved at an ON of 0, while the increased load for the lowest temperature is made by moving to the minimum

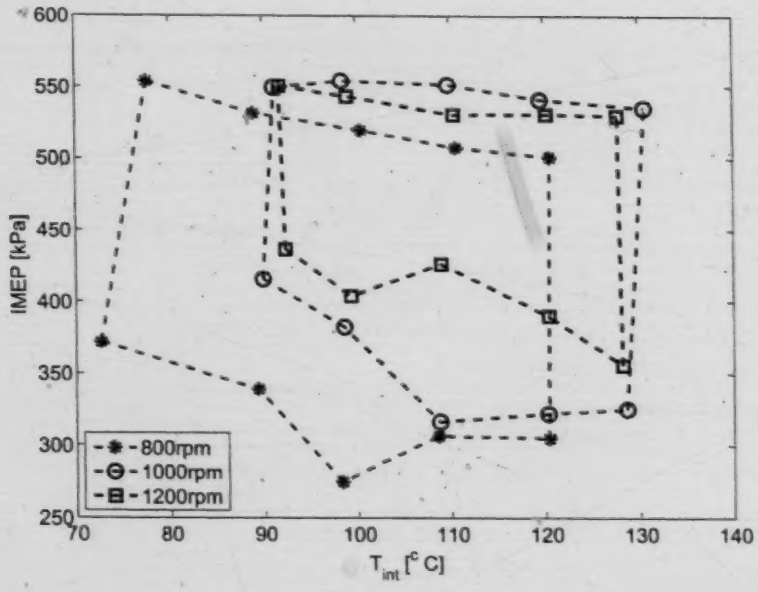

Figure 5.6: Load Range in terms of IMEP vs T_{int} for three values of engine speed with MAP of 125kPa. Minimum and maximum load limits shown for Cases E, G and H of Table 4.3

PW_{octane} of 1.3msec. This point represents the limiting case for which the minimum change in ON which can be achieved using the dual fuel technique. As expected, ON must increase to maintain combustion timing as T_{int} rises, for all cases shown.

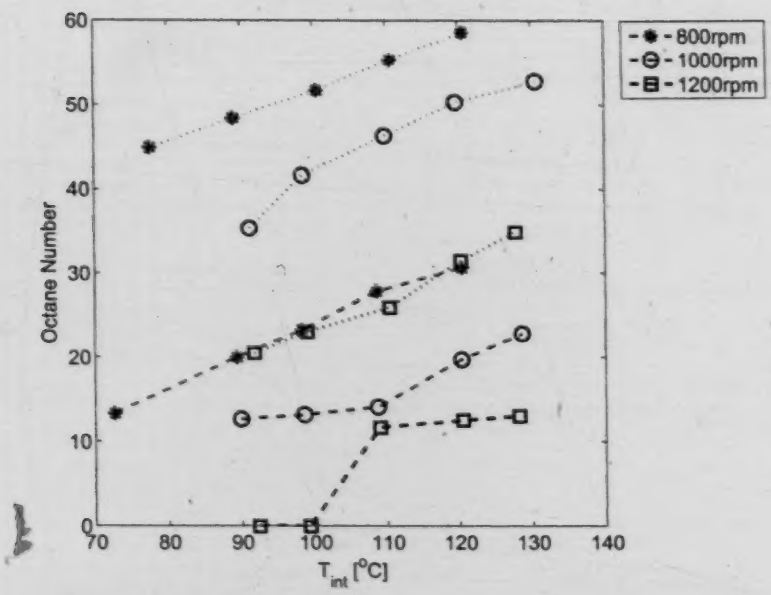

Figure 5.7: ON for Minimum and Maximum Load for Different Engine Speed vs. T_{int} with MAP=125kPa. Cases E, G and H of Table 4.3. Dashed lines indicate minimum load cases and dotted lines maximum load cases.

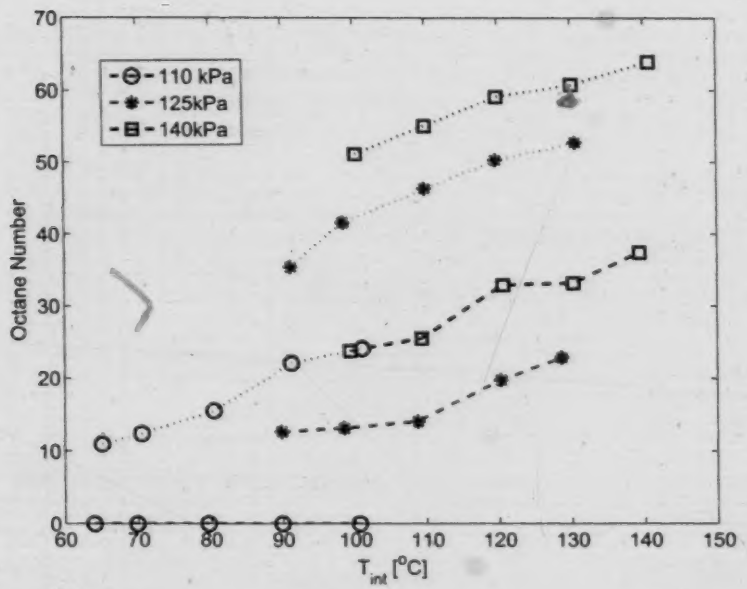

Figure 5.8: ON for Minimum and Maximum Load for Different MAP vs. T_{int} with N=1000rpm. Cases D, E and F of Table 4.3. Dashed lines indicate minimum load cases and dotted lines maximum load cases.

The low ON fuels used result in the LTR region being an important feature of the combustion as shown in Figures 4.7 and 4.8. The heat release in the LTR is an important area to investigate, as these reactions form the precursors of the HTR reactions [Tanaka et al., 2003a, Kirchen et al., 2007]. In particular, the heat released in the LTR region increases the in-cylinder temperature for the HTR region. Engine operating parameters that change the amount of HR_{LTR} require a different mixture condition in order to maintain combustion timing.

The average value of HR_{LTR} for all cycles of a test is compared with the mass of n-heptane injected per cycle, in Figures 5.9 and 5.10. HR_{LTR} is compared with the mass of n-heptane for change in MAP in Figure 5.9, and for changes in engine speed in Figure 5.10. For both figures, the dashed line represents the case of minimum load, and the dotted line the case for maximum load. It is noteworthy that a relatively small change in n-heptane mass is required to maintain combustion timing when going from the minimum load to the maximum load condition. The average reduction in n-heptane from the minimum load condition to the maximum load condition is 5.3%, while the maximum reduction is 15.3%. The initiation of the HTR combustion in PRF blends is dominated by the LTR and HTR kinetics of the n-heptane while the total heat released during combustion is dependent on the total fuel quantity [Tanaka et al., 2003a, Tanaka et al., 2003b]. The decrease in n-heptane required to maintain a constant SOC in these tests is due to the increase in T_{IVC} going from the minimum load case to the maximum load case. If this effect is not compensated for, the SOC would advance from the desired setpoint.

The HR_{LTR} is strong function of the n-heptane mass, as even small increases in the mass result in dramatic increases in the HR_{LTR}, as shown in Figure 5.9 and Figure 5.10. In Figure 5.9 the HR_{LTR} for a given amount of n-heptane can be seen to increase dramatically with increased MAP. For example, at 7mg/cycle of n-heptane, going from 125kPa MAP to 140kPa, results in an approximately 50% increase in the

HR_{LTR}. The range of HR_{LTR} for which stable combustion occurs in this engine is however limited to a range of HR_{LTR} of 0.020-0.045kJ. In Figure 5.10 the HR_{LTR} can also be seen to be a strong function of engine speed. For low engine speeds, the additional time of the mixture in a thermodynamic state conducive to the LTR's results in a higher HR_{LTR}. This engine speed dependence may also account for the lower ON required as engine speed increases, in order to maintain the HR_{LTR} required for the desired SOC.

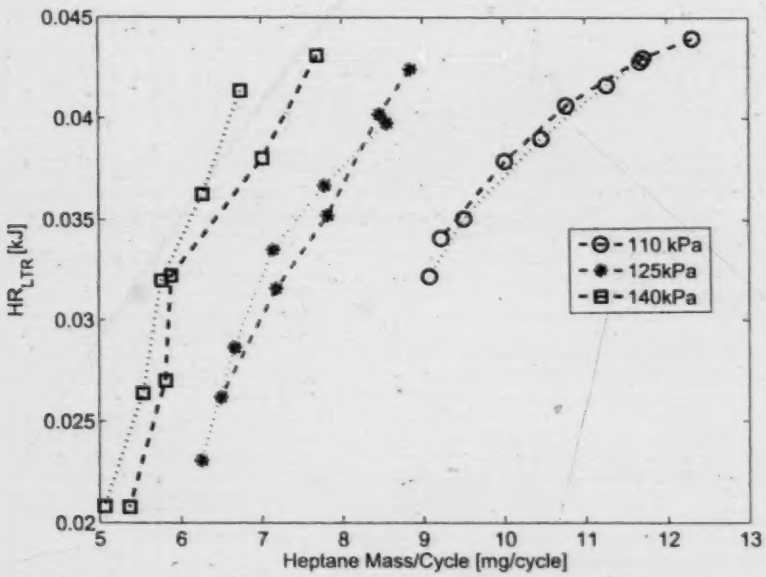

Figure 5.9: HR_{LTR} vs. Heptane Mass per Cycle for Three MAP, N=1000rpm. Cases D, E and F of Table 4.3. Dashed lines indicate minimum load cases and dotted lines maximum load cases.

To understand the effects of changing MAP and N on the HR_{LTR} a correlation based on the overall combustion mechanism for the LTR region (reaction $R3$ of Section 2.1 is performed. The rate of production of either product of this equation can be written as:

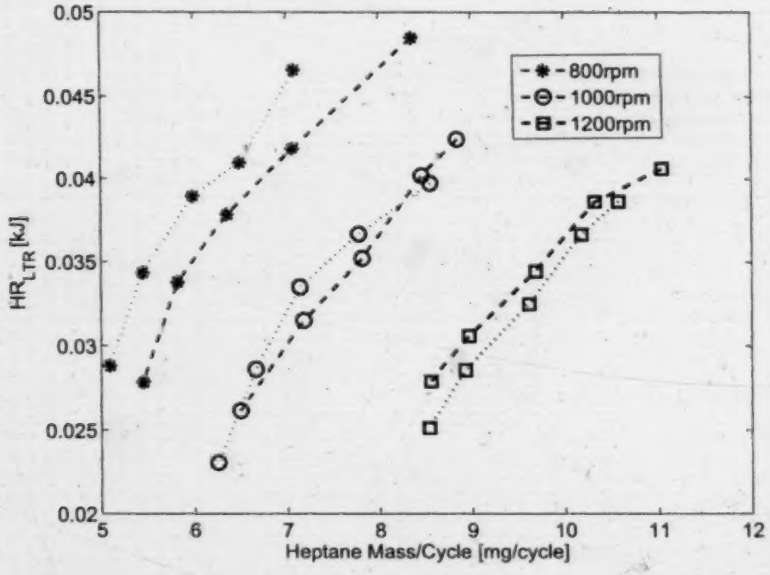

Figure 5.10: HR_{LTR} vs. Heptane Mass per Cycle for Three Engine Speeds, MAP=125kPa. Cases E, G and H of Table 4.3. Dashed lines indicate minimum load cases and dotted lines maximum load cases.

$$\frac{d[p]}{dt} \propto [C_7H16][O_2]^2 \tag{5.1}$$

Where p can be either product. Although this is not an elementary reaction, and thus the order of the reaction is not equivalent to the stoichiometric coefficients, it is used here as the complete evaluation of the relevant equations is beyond the scope of this work. Since the source of O_2 is ambient air, the concentrations of both are proportional. With constant cylinder volume and molecular weights of n-heptane and air for all test cases, the volume concentrations in Eqn. 5.1 can be converted to mass. With this and since the heat released by this combustion reaction is proportional to the products produced

$$\frac{dQ_{HR_{net}}}{dt} \propto m_{heptane} m_{O_2}^2 \tag{5.2}$$

To determine the effects on the total heat release in the LTR region, Eqn. 5.1 is integrated assuming negligible change in the concentrations of C_7H16 and O_2 during the LTR period:

$$HR_{LTR} \propto m_{heptane} m_{O_2}^2 t \propto \frac{m_{heptane} m_{O_2}^2}{N} \tag{5.3}$$

The characteristic time available for combustion is proportional to the inverse of engine speed, so this is also included in Eqn. 5.3. The results of this normalization are shown in Figure 5.11. Although the normalization procedure is not able to linearize the relationship between the HR_{LTR} and $m_{heptane}$, MAP and N, it is able to collapse all of the operating points in this investigation into a similar curve. A power function fit to the experimental data is also shown in Figure 5.11.

The dependence of the HR_{LTR} on T_{int} is shown in Figure 5.12 and Figure 5.13 for changes in MAP and engine speed, respectively. In Figure 5.12 the HR_{LTR} can be seen to decrease with increasing T_{int}. This is effect is most intimately linked with the fact that as intake temperatures increase, the ON required to maintain a constant SOC increases, requiring a lower mass of n-heptane to maintain the same SOC. The reduction in HR_{LTR} with T_{int} can be seen to follow a similar trend for each engine speed tested, as shown in Figure 5.13.

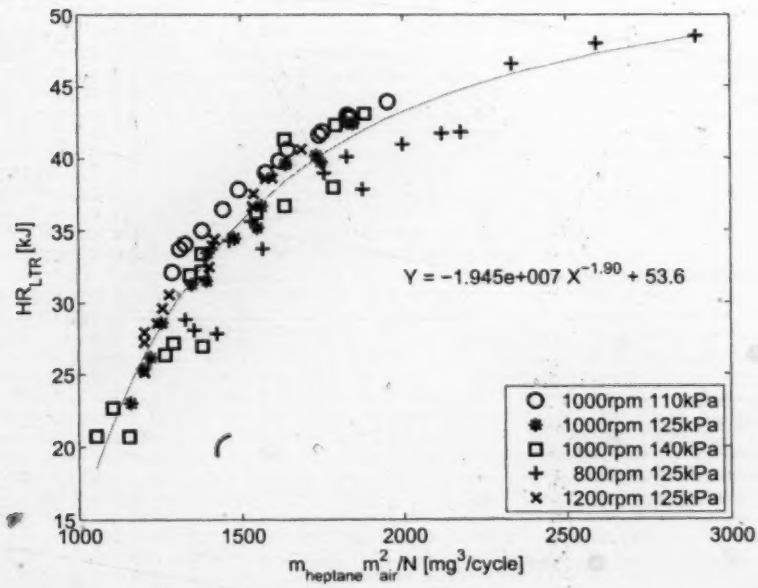

Figure 5.11: HR_{LTR} normalized for changes in MAP and N. Cases D-H of Table 4.3.

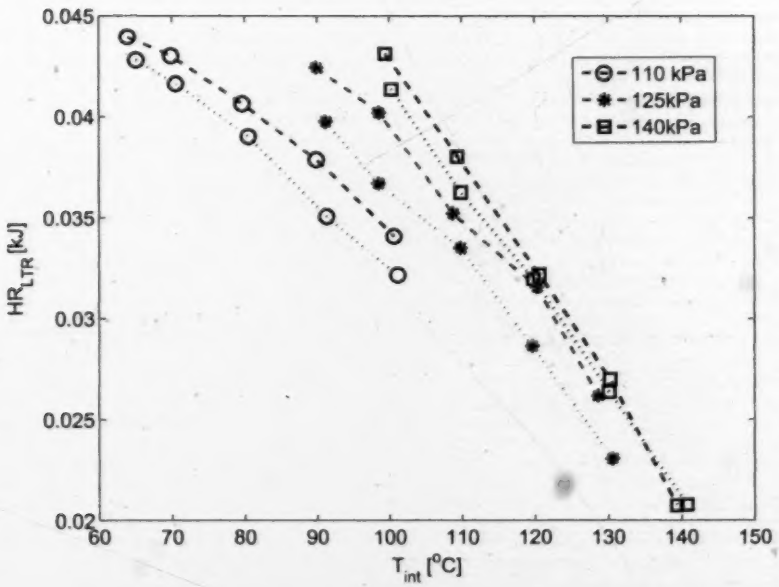

Figure 5.12: HR_{LTR} vs. T_{int} for Three MAP at N-1000rpm. Cases D, E and F of Table 4.3. Dashed lines indicate minimum load cases and dotted lines maximum load cases.

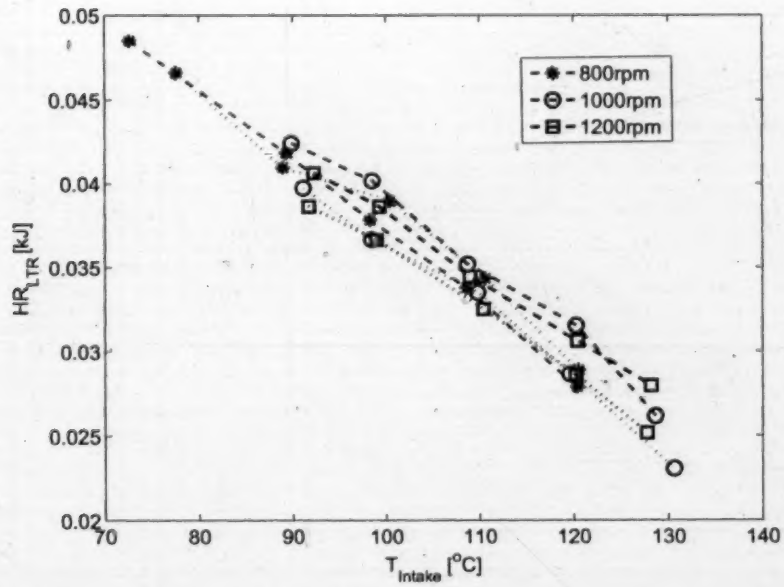

Figure 5.13: HR_{LTR} vs. T_{int} for Three Engine Speeds for MAP=125kPa. Cases E, G and H of Table 4.3. Dashed lines indicate minimum load cases and dotted lines maximum load cases.

5.3.3 Estimated Temperature Parameters

The point of IVC represents the start of the closed portion of the engine cycle (assuming no blow-by past the piston rings). The in-cylinder temperature at IVC is an important metric, as it effectively determines the initial condition for the temperature path during compression. Here the method of estimating the in-cylinder mass at IVC described in Section 4.4 for determining the value of T_{IVC} based on the Ideal Gas Law is used. The estimated value of T_{IVC} is compared to T_{int} for various values of MAP and engine speed in Figure 5.14 and Figure 5.15, respectively. The dashed lines represent the case of minimum load, and the dotted lines the maximum load case. In both figures, the T_{IVC} can be seen to increase with T_{int} with an average slope of about 0.4. Convective heat transfer between the intake charge and the intake manifold, intake port, intake valve, and cylinder surfaces all influence the value of the charge temperature from the intake manifold condition T_{int}, to the value at IVC, T_{IVC}. For relatively low values of T_{int} heat transfer from the port and cylinder surfaces increase the temperature of the incoming charge. As T_{int} increases the temperature gradient between the intake port and cylinder surfaces, and the intake charge is reduced, lowering the total heat transfer.

To estimate the convective heat transfer coefficient in the intake port, a steady, turbulent pipe flow correlation is used [Heywood, 1988]. The correlation used is the is the Dittus-Boelter equation [Incropera and DeWitt, 2002]:

$$h = 0.023 \frac{k_{int}}{d_{int}} Re_d^{0.8} Pr^{0.4} \tag{5.4}$$

Where d_{int} is the diameter of the intake port, k_{int} is the thermal conductivity of the mixture in the intake port, Re_d is the Reynolds number in the intake port, and Pr is the Prandtl number. Properties of air at T_{int} are used for evaluating Eqn. 5.4. Using this equation, the heat transfer coefficient for the intake port is found assuming

steady flow in the intake port. Evaporation due to fuel is neglected. The estimated heat transfer coefficient is shown in Figure 5.16 as a function of T_{int}. The average convective heat transfer coefficient changes by $\pm 10\%$ for each case, however the value is relatively constant with changes in T_{int}, changing by 1-7% over the range tested. Increasing MAP increases the estimated heat transfer coefficient, as higher mass flow rates through the intake port are seen. Similarly for higher engine speeds, the mass flow rate increases, increasing the Reynolds number.

For the cases of a constant MAP, increasing T_{int} reduces the mass of charge in the intake manifold, increasing the temperature change due to heat transfer, assuming a constant convective heat transfer coefficient. The increased heat transfer for lower T_{int} results in a unifying effect on the T_{IVC}. One effect that is not investigated here, is the effect of thermal stratification in the intake charge during the intake and compression strokes. In [Sjoberg et al., 2005] the authors show that thermal stratification of the in-cylinder charge can play an important role in the combustion duration. For a Diesel engine of 18:1 compression ratio, converted to air-diluted HCCI operation Sjoberg et al. show that the spatial temperature variation of the core of the charge at BDC of the intake stroke is approximately 20K.

In Figure 5.14 the effect of increasing MAP on the T_{IVC} can be seen. Dashed lines represent the minimum load condition, while dotted lines the maximum load condition. Increased manifold pressure results in a slightly reduced T_{IVC}, given the same T_{int}. This is attributed to the increased cylinder mass for this case, reducing the effect of the heat transfer during the intake stroke. Assuming a constant heat transfer coefficient between the incoming charge, and the port and cylinder surfaces, an increased mass of intake charge (due to increasing the MAP and thus the density) will result in a smaller change in temperature. The increased intake charge at higher MAP acts as a larger thermal mass, reducing the temperature fluctuation with changing T_{int}. Combined with this effect is the reduced influence of the temperature of the residual

fraction, with increasing MAP. Thus as MAP increases, the temperature influence of a constant amount of residual is reduced.

In Figure 5.15, with dashed lines indicating the minimum load condition, and dotted lines the maximum load condition, as engine speed increases, the T_{IVC} increases for a given T_{int}. This is attributed to increased cylinder surface temperatures and/or the increased heat transfer due to higher average intake charge fluid velocities acting to increase the convective heat transfer coefficient at higher engine speeds, see Figure 5.16.

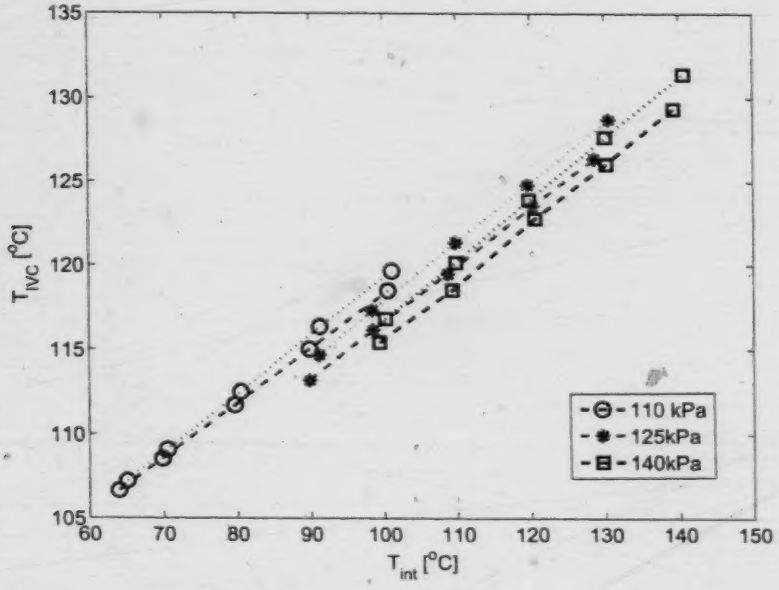

Figure 5.14: T_{IVC} vs. T_{int} for three value of MAP at N=1000rpm. Cases D, E and F of Table 4.3. Dashed lines indicate minimum load cases and dotted lines maximum load cases.

As the temperature rise due to combustion is a function of λ (as λ is effectively a ratio of the fuel energy available to the amount of diluent, namely air) the maximum in-cylinder temperature changes significantly over the range of operating conditions. In Figure 5.17 and Figure 5.18 the value of T_{max} is compared with T_{int} for three values

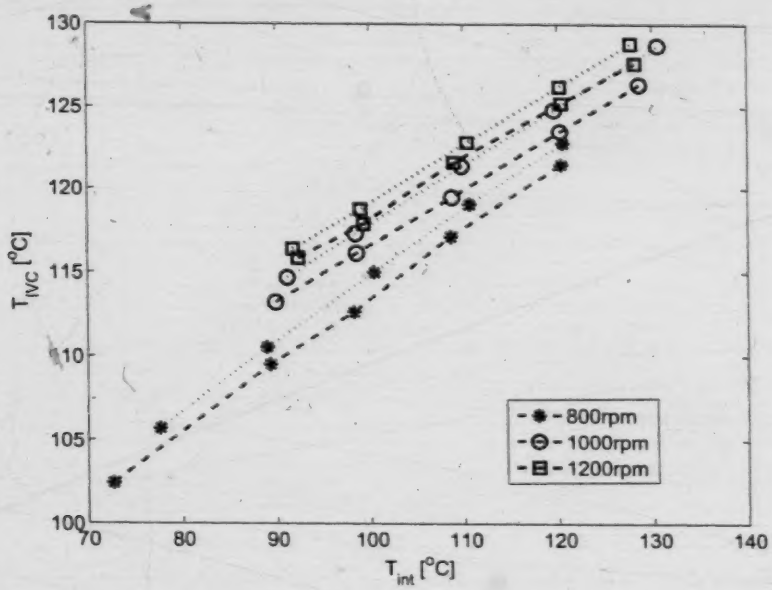

Figure 5.15: T_{IVC} vs. T_{int} for three Engine Speeds at MAP=125kPa. Cases E, G and H of Table 4.3. Dashed lines indicate minimum load cases and dotted lines maximum load cases.

of MAP, and three values of engine speed, respectively. T_{max} is determined by finding the maximum value of the estimated temperature during each cycle, using Eqn. 4.7. The dashed lines indicate the minimum load cases, and the dotted lines the maximum load cases. For each series of tests points (ie. a constant MAP, or N) the mass of air entering the cylinder remains relatively constant (the value of T_{int} has some effect), as the MAP and valve timings remain fixed. Thus the value of T_{max} is dependent on fuel quantity, λ, for each point.

The T_{max} of the minimum load condition can be seen to decrease significantly for increasing MAP, as shown in Figure 5.17. The additional temperature generated by the increased HR_{LTR} for the higher values of MAP, allows leaner mixtures to auto-ignite, than would be possible without the HR_{LTR}. With the increased λ the temperature rise due to combustion is reduced, leading to lower maximum temper-

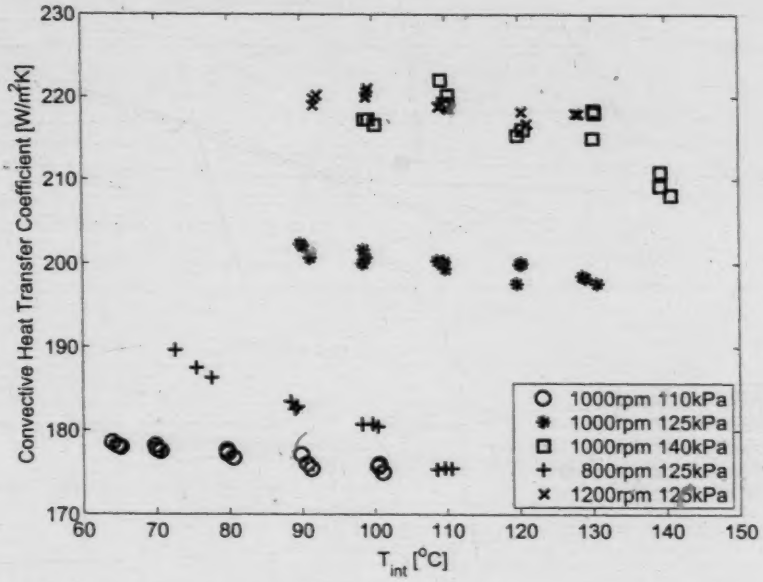

Figure 5.16: Estimated Convective Heat Transfer Coefficient in the intake port vs T_{int}. Cases D-H of Table 4.3.

atures. To be able to oxidize the fuel during the combustion process, a minimum temperature of approximately $800°C$ is required for the relatively slow CO oxidation kinetics enough time to complete, [Turns, 2000, Heywood, 1988]. In Figure 5.18 for an engine speed of 800rpm, the value of T_{max} achieved is very near this minimum temperature. Similarly for the two increased values of MAP in Figure 5.17, a minimum temperature of approximately $900°C$ is approached for several cases. The increase in the CO emissions at these large values of λ are caused by the low maximum in-cylinder temperatures. This is further shown in Figures 5.20 and 5.21.

In Figure 5.17 the T_{max} for the high load cases can be seen to be nearly consistent for all three values of MAP. This limit of approximately $1600°C$ is maintained for all three maximum load cases. This maximum temperature also coincides with the temperature at which thermal NO_x begins to form in significant amounts, according

to the Zeldovich kinetic mechanism, [Turns, 2000, Heywood, 1988]. As the maximum temperature that is achieved during the cycle is bordering the temperature at which thermal NO_x is formed in significant amounts even a small decrease in λ results in a large increase in the amount of NO_x generated. Further investigations into the emissions aspects of the engine are shown in the following section.

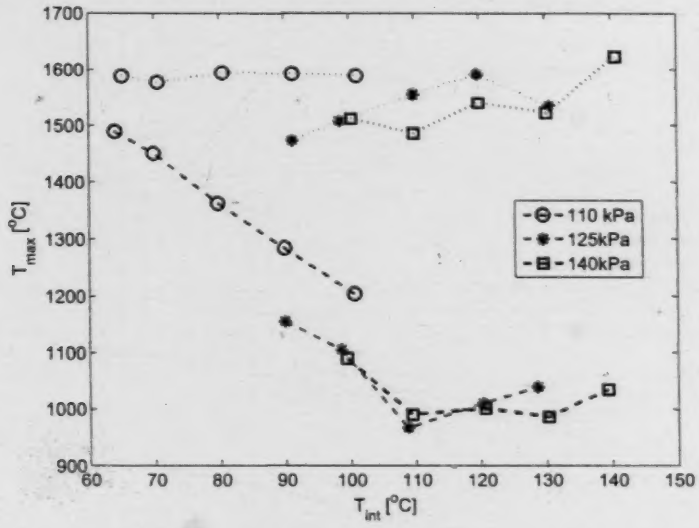

Figure 5.17: T_{max} vs. T_{int} for three value of MAP for N=1000rpm. Cases D, E and F of Table 4.3. Dashed lines indicate minimum load cases and dotted lines maximum load cases.

For the air-diluted HCCI studied here, the value of λ represents a ratio of not only a relative measure of the AFR, but also a measure of the mass of air diluent to the quantity of energy available for release. As the majority of the dilution of the fuel comes from the mass of air charge (with a small fraction coming from the residual fraction), while the energy available for combustion comes from the mass of fuel inducted, the relative ratio of these two quanties, λ, is significant. For a given value of λ, the fuel is able to raise the temperature of the air charge by a given quantity, due to the amount of heat released. Increasing λ (leaner) will reduce the

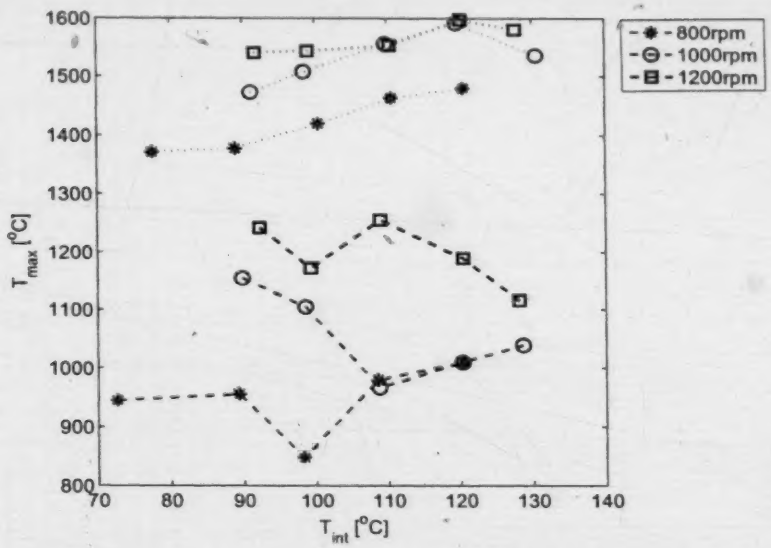

Figure 5.18: T_{max} vs. T_{int} for three Engine Speeds for MAP=125kPa. Cases E, G and H of Table 4.3. Dashed lines indicate minimum load cases and dotted lines maximum load cases.

temperature rise due to combustion, as there is less fuel to heat a given amount of air. In Figure 5.19 the test average value of T_{max} is compared with the average λ for all of the steady state test cases. The value of T_{max} can be seen to be indeed a strong function of λ. The error bars in Figure 5.19 represent ± 1 standard deviation of the 450 engine cycles in the estimated value of T_{max} for each test case. The data scatter is attributed to changes in the fuel conversion efficiency of each individual cycle in each test case, and to small variations in λ from cycle to cycle throughout the test case.

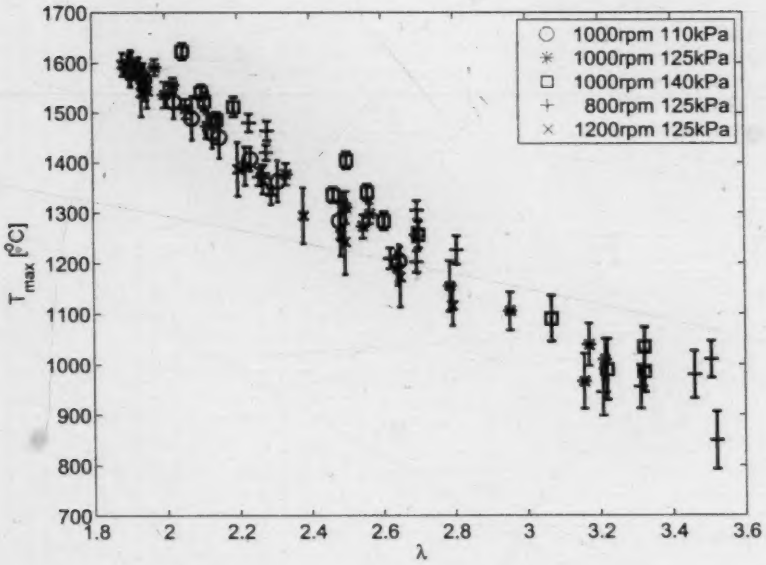

Figure 5.19: T_{max} vs. λ for Cases D, E, F, G, and H of Table 4.3

5.3.4 Brake Specific Emissions and Fuel Consumption

One of the major benefits of HCCI combustion is the potential reduction in emissions, namely NO_x [Stanglmaier and Roberts, 1999]. The emissions in this study are measured on a dry basis, after the water has been removed by a cooler, as described in Section 3.4. To determine the engine out emissions, the procedure shown in [Atkins, 2004] is used and a description of this analysis can be found in Appendix B. As in the previous Section, the results presented in this Section are from the steady state tests found in Table 4.3. All 75 steady state points, shown in Table 4.3, are used in each Figure unless noted otherwise.

Although emissions are measured on a volumetric basis, either in % or ppm, a standardized method of reporting emissions is a brake specific measurement. This metric is calculated by using Eqn. 5.5, where 'yy' indicates the species considered, CO, UHC, NO_x , or fuel consumption.

$$BSyy = \frac{\dot{m}_{yy}}{\mathrm{P}_{brake}} \tag{5.5}$$

The brake specific emissions of CO as a function of T_{max} is shown in Figure 5.20 and as a function of λ is shown in Figure 5.21. The error bars in each figure represent ± 1 standard deviation of the values obtained in the cases where multiple trials of the same point are run. In Figure 5.20 the BSCO can be seen to increase by a factor of 10 as the peak combustion temperature decreases from $1400°C$ to $1000°C$. This is attributed to the engine entering the partial burn regime where the kinetics are unable to completely react the mixtures before the piston descends on the expansion stroke, quenching the mixture. For peak combustion temperatures of less than ~1500K (for an engine operating at 1200rpm) a significant increase in CO emissions occur because of this bulk gas quenching [Dec and Sjoberg, 2003]. They also show that slightly boosting the engine (MAP of 101kPa to 120kPa) has no significant effect

on changing this characteristic temperature when intake temperature is adjusted to maintain combustion timing. In Figure 5.21 the BSCO can be seen to be a strong function of the directly measured value of λ, where significant increases in CO occur for λ above approximately 3. A very similar trend is shown in [Bhave et al., 2005] for a slightly different experimental setup and operating range with PRF of ON 95 as a fuel. In [Bhave et al., 2005], the CO emissions rise dramatically at approximately λ of 4. Similarly in this work, λ is the only factor found which significantly affects the emissions of BSCO.

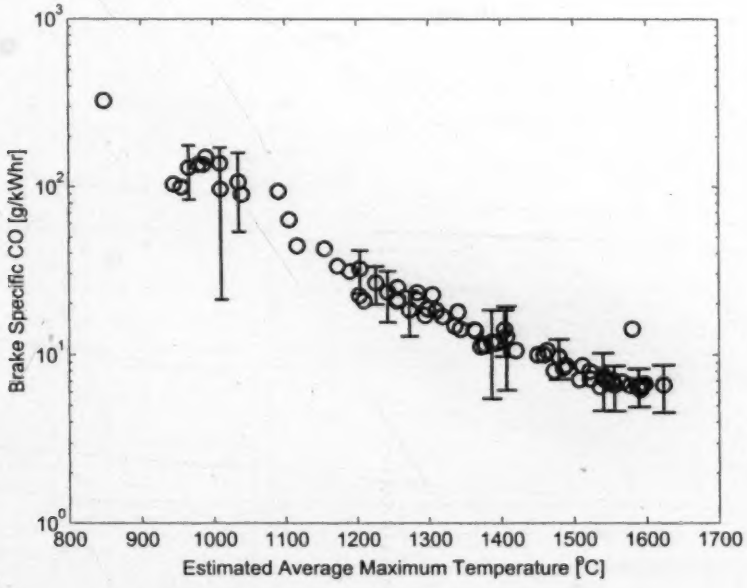

Figure 5.20: Brake Specific CO Emissions vs. T_{max} for Cases D, E, F, G, and H of Table 4.3

The BSUHC emissions are shown as a function of T_{max} is shown in Figure 5.22. The error bars represent ± 1 standard deviation of the values of BSUHC obtained for the cases where multiple trials of the same point are run. As with BSCO emissions, as combustion temperatures decrease, the BSUHC emissions rise as shown in Figure 5.22.

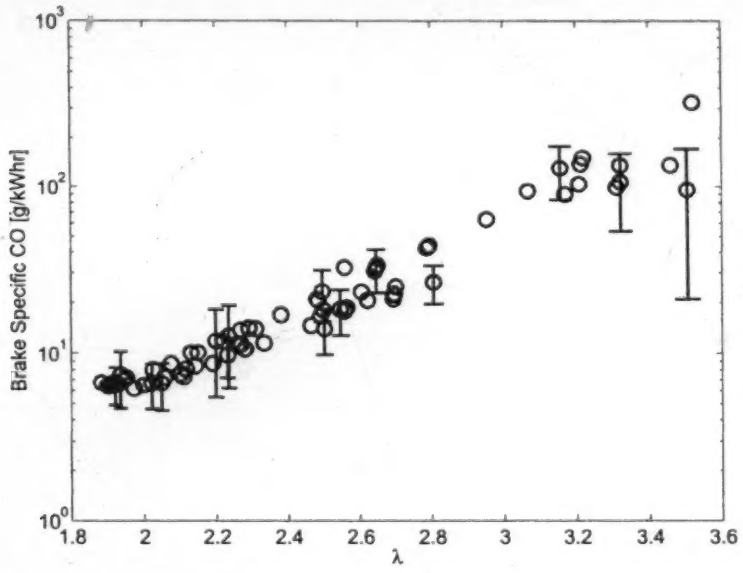

Figure 5.21: Brake Specific CO Emissions vs. λ for Cases D, E, F, G, and H of Table 4.3

The reduced combustion temperatures are less able to oxidize the partially burned hydrocarbons with decreasing combustion temperatures. BSUHC is compared with λ in Figure 5.23, with the ± 1 standard deviation of cases where multiple trials are run. Despite increasing values of λ having reduced amounts of injected fuel quantity (and thus one might expect reduced UHC emissions due to lower fuel quantity), the BSUHC emissions increase with λ. As with BSCO, as λ increases T_{max} typically decreases, resulting in reduced combustion temperatures. While higher combustion temperatures during the exhaust stroke would typically oxidize the hydrocarbons, the low temperatures inhibit these reactions. A very similar trend of UHC emissions for this range of λ appears in [Bhave et al., 2005]. A series of experimentally validated modeling investigation in [Aceves et al., 2001, Aceves et al., 2002] shows that for low load HCCI conditions the major contributor of UHC is crevice sources. The quenching

of air-fuel mixture in space between the piston crown and the top piston ring was found to be responsible for the majority of UHC emissions. As the thermal boundary layer surrounding the piston and cylinder liner significantly reduce the gas temperature near the wall during combustion, the combustion kinetics are dramatically slowed in being able to oxidize the fuel in these zones.

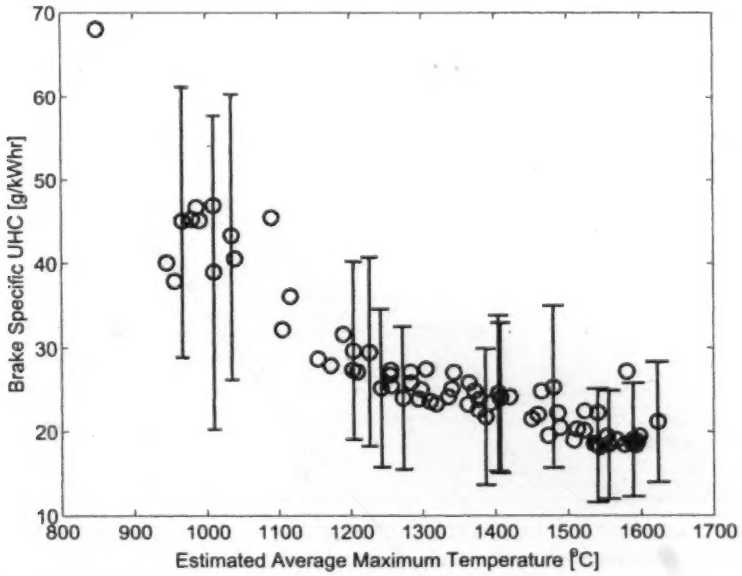

Figure 5.22: Brake Specific UHC Emissions vs. T_{max} for Cases D, E, F, G, and H of Table 4.3

The BSNO$_x$ emissions are shown in Figure 5.24 and in Figure 5.25 as a function of T_{max} and λ respectively. Error bars indicate ± 1 standard deviation of BSNO$_x$ for tests with repeated trials. It should also be noted that the error bars are centered around the one steady state test, and not the average of the repeated trials. For the majority of cases tested, the measured value of NO$_x$ is <5ppm with several cases reading near zero within the accuracy of the analyzer. In Figure 5.24, as T_{max} increases above approximately $1500°C$, the dramatic increase in NO$_x$ production can be attributed

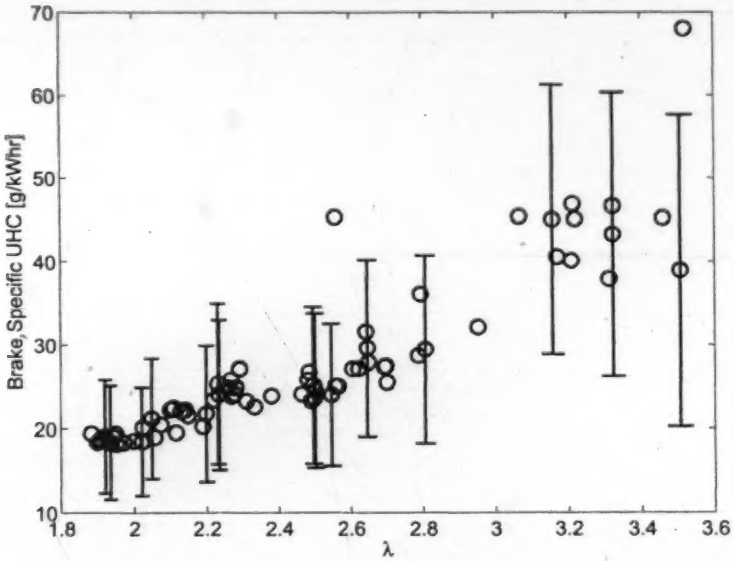

Figure 5.23: Brake Specific UHC Emissions vs. λ for Cases D, E, F, G, and H of Table 4.3

to thermal NO_x production by the Zeldovich mechanism [Turns, 2000]. The large variation in $BSNO_x$ with $T_{max} > 1500\ ^\circ C$ is attributed to the in-cylinder temperature variations from trial to trial. A trial with even slightly increased peak combustion temperatures will result in a significant increase in NO_x production, as the threshold level for NO_x production is approached. When the value of T_{max} is plotted against λ, as shown in Figure 5.19, the drastic increase in NO_x can be explained by the increased T_{max} encountered as λ is decreased. As the value of λ decreases, there is a distinct increase in the emissions of NO_x , as shown in Figure 5.25. The increasing trend in $BSNO_x$ for $\lambda > 2.4$ is mainly due to the decrease in brake power output rather than an increase in the NO_x flow rate. Just as with the CO and UHC emissions, a nearly identical trend in NO_x is shown by [Bhave et al., 2005], with $BSNO_x$ in the range of 0.05-0.2 g/kWhr.

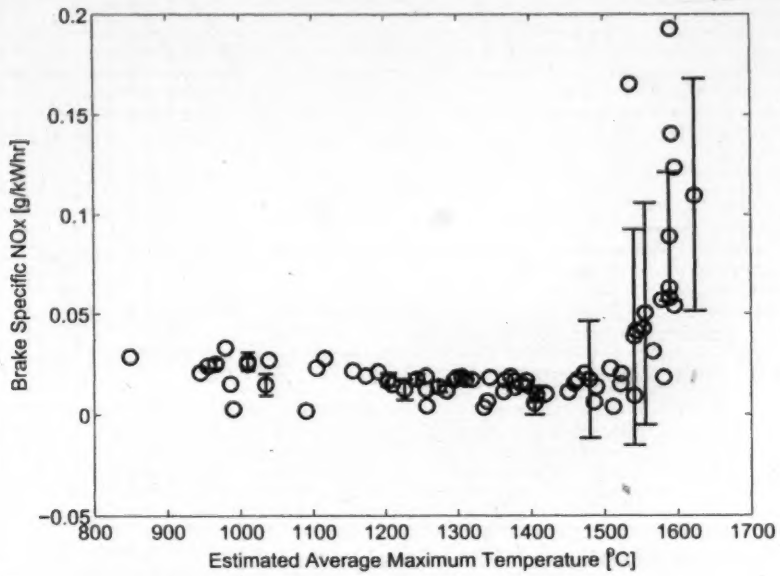

Figure 5.24: Brake Specific NO_x Emissions vs. T_{max} for Cases D, E, F, G, and H of Table 4.3

The BSFC of an engine is an important performance metric, which is inversely related to the thermal efficiency of the engine. In Figure 5.26 the BSFC is shown against BMEP for all of the steady state test cases. The relationship between BSFC vs. BMEP shows little change with engine speed, for the speeds tested in this work. The BSFC can be seen to decrease with increasing BMEP, as the fraction of work that goes to FMEP is reduced with increasing BMEP. As a basis of comparison, Figure 5.27 shows the difference of BSFC vs. BMEP for this engine run in SI mode (see Appendix A.5 for a detailed list of experimental points in SI mode), and in HCCI mode. The inability to run SI tests at all loads similar to the HCCI points is due to not being able to throttle the engine sufficiently to reduce the load. However, for a load of 400kPa BMEP, the BSFC in SI mode is approximately 310g/kWhr, while in HCCI mode the BSFC is approximately 250g/kWhr. This is a reduction of fuel

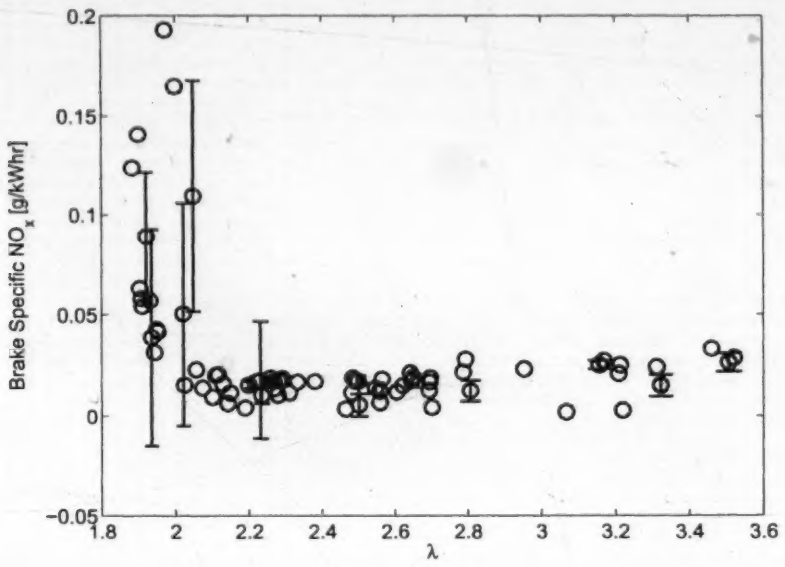

Figure 5.25: Brake Specific NO_x Emissions vs. λ for Cases D, E, F, G, and H of Table 4.3

consumption of approximately 20%. The reduction in fuel consumption of HCCI compared with SI is due to the reduced pumping losses (higher MAP) in HCCI, as well as the faster combustion rate during HCCI which is able to more closely emulate the ideal Otto cycle,[Heywood, 1988].

A comparison of the brake specific emissions output of the Ricardo engine in SI and HCCI modes are shown in Figures 5.28 and 5.29. The BSCO emissions of the engine in HCCI and SI modes can be seen in Figure 5.28. The most significant difference in emissions from SI and HCCI modes, can be seen at low load operation in HCCI, where BSCO increases dramatically. In SI mode the measured value of *CO* is of the range of 0.3-1% by volume. These values are close to the values typical of an SI engine [Heywood, 1988]. As the engine is operated in stoichiometric mode for all SI tests, a small shift to the rich side results in a significant increase in *CO*.

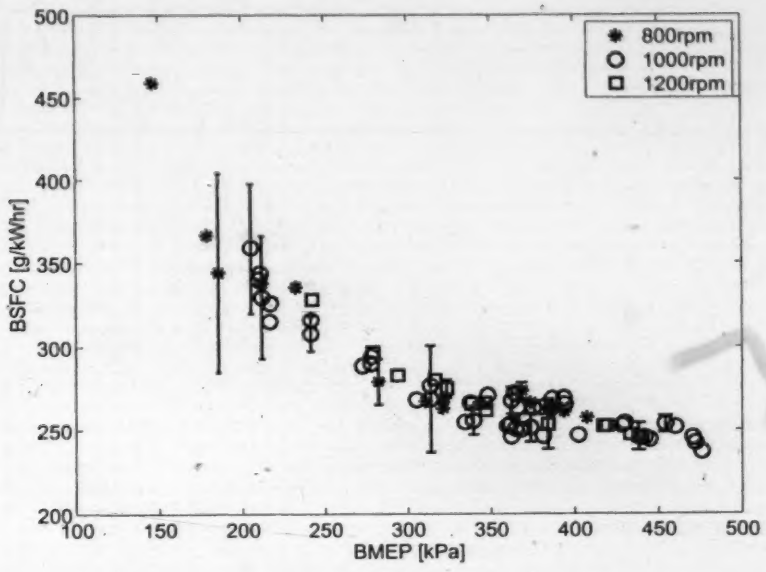

Figure 5.26: BSFC vs. BMEP for Cases D, E, F, G, and H of Table 4.3

BSCO is higher in HCCI than those of SI mode at low loads. At higher loads, where the load ranges of the two combustion modes overlap, HCCI mode actually produces considerably lower *CO* than SI.

The values of BSUHC in SI and HCCI modes is shown in Figure 5.29. The average engine out UHC emissions for this engine in SI mode are $3x10^3$ppm. While this value is somewhat high for an SI engine, it is within the range of values expected by Heywood, of 1000-3000ppm. The cause of these high UHC could be caused by the regular use of the Ricardo engine. [Heywood, 1988] shows an approximately 25% reduction in UHC emissions after removing combustion deposits from the combustion chamber. Although the UHC emissions in SI are somewhat high, the condition of engine is similar for both SI and HCCI tests, so the results are comparable. The spread in UHC emissions for SI mode is due to the changes in engine speed, over the tests of SI operation.

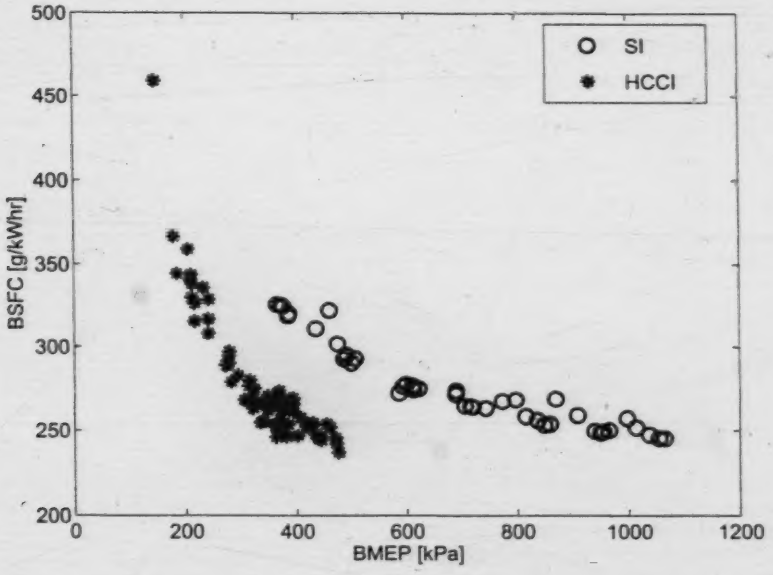

Figure 5.27: BSFC vs. BMEP for SI and HCCI

The values of $BSNO_x$ are not compared for SI and HCCI modes, as for the majority of cases in SI, the NO_x concentrations were in excess of the range of the analyzer (2500ppm). This is telling, however, of the significant difference in NO_x production between SI and HCCI modes. For all HCCI cases, NO_x was present in volume concentrations of <25ppm, with the majority of cases reading <5ppm. All SI cases generated NO_x volume concentrations of >2500ppm. Thus a reduction of two to three orders magnitude of NO_x is possible with HCCI compared to SI.

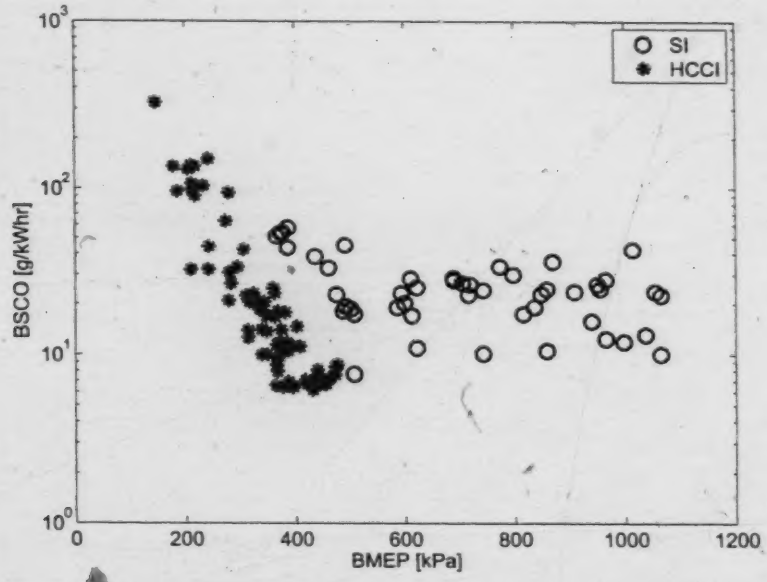

Figure 5.28: BSCO vs. BMEP for SI and HCCI

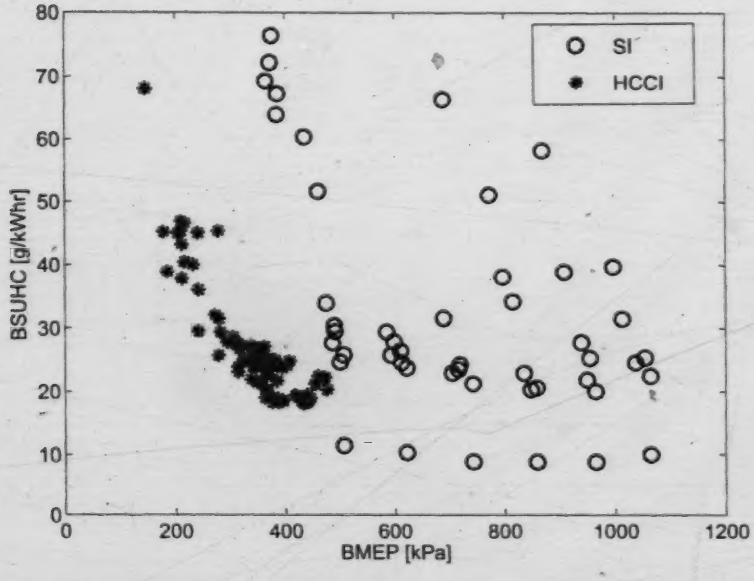

Figure 5.29: BSUHC vs. BMEP for SI and HCCI

5.3.5 HCCI Knock

The limiting factor for high load operation in all tests in this thesis is the onset of excessive pressure rise rates or knocking combustion. While HCCI itself is similar to knock in an SI engine, the process of knock in HCCI engines is thought to be caused by a different source. In [Yelvington and Green, 2003] the onset of knock in HCCI engines is defined to be when a local over-pressure can occur in a parcel of mixture undergoing combustion. This occurs when the local rate of heat release exceeds the ability of the reacting volume to maintain its pressure with the surroundings. If the rate of heat release were to exceed the parcel's ability to expand, at its local speed of sound, a pressure gradient will be created between the parcel and its surroundings. This then causes a pressure wave to be formed and eventually reflect throughout the chamber. A similar description is proposed by in [Andreae et al., 2007].

As the onset of knock can be associated with increasing pressure rise rates within the cylinder, a metric to capture the speed of the combustion is desired. Here the average pressure rise rate of the high temperature combustion region is used, as shown in Eqn. 5.6.

$$\frac{\Delta P}{\Delta \theta} = \frac{P_{CA90} - P_{CA5_{HTR}}}{CA90 - CA5_{HTR}} \tag{5.6}$$

Another commonly used metric of combustion is the Burn Duration (BD):

$$BD = CA90 - CA5_{HTR} \tag{5.7}$$

A comparison of the test average value of $\frac{\Delta P}{\Delta \theta}$ as a function of λ is shown in Figure 5.30 for variations in intake manifold pressure, and in Figure 5.31 for variations in engine speed. In both plots the error bars indicate ± 1 standard deviation of the 450 engine cycles of the experimental data. Similar trends and absolute values

of pressure rise rate are shown in [Oakley et al., 2001] for a range of fuels at a constant engine speed of 1500rpm. Decreasing λ results in a greater value of $\frac{\Delta P}{\Delta \theta}$ as the combustion kinetics decrease the combustion duration, thus reducing the denominator of Eqn. 5.6, while simultaneously the decrease in λ results in a greater rise in pressure of combustion due to increased fuel energy release. These two effects compound to increase the value of $\frac{\Delta P}{\Delta \theta}$. In Figure 5.30 the value of $\frac{\Delta P}{\Delta \theta}$ increases with MAP for a given λ. This indicates that although λ has an influence on $\frac{\Delta P}{\Delta \theta}$, there are other effects involved. While keeping a fixed λ with increasing MAP maintains a fixed energy release for a given mass, the kinetic mechanisms that oxidize the fuel are dependent on the volume concentrations of fuel and oxygen [Turns, 2000], which increase for these conditions. The increased volumetric concentrations may be decreasing the combustion duration even though the λ remains constant.

In Figure 5.31 the effect of engine speed on $\frac{\Delta P}{\Delta \theta}$ is shown with changes in λ. Increasing engine speed has the effect of reducing $\frac{\Delta P}{\Delta \theta}$ for a given λ. Since the kinetics of HCCI are fundamentally time-based phenomena, the lower $\frac{\Delta P}{\Delta \theta}$ may be attributed to the increased duration in CAD, which occurs for a fixed combustion time. Converting $\frac{\Delta P}{\Delta \theta}$ to a time-based parameter $\frac{\Delta P}{\Delta t}$, by using the test average value for engine speed to transform the angle-based parameter to time-based parameter, results in Figure 5.32. In a strictly time-based sense the values of $\frac{\Delta P}{\Delta t}$ with λ come to a much closer agreement. The remaining difference between the curves of Figure 5.32 may come from the slightly different combustion timings used for each engine speed. The delayed SOC at higher engine speed causes the piston to be further down in the bore compared with an earlier SOC. This difference results in a change in the rate of cylinder volume change throughout the combustion process. The result is a lower value of $\frac{\Delta P}{\Delta t}$ given otherwise similar conditions. The relationship between BD_{time}, made to be a function of time with the known engine speed, is shown in Figure 5.33 compared against λ. For the range of test points in this investigation, the relationship between BD_{time} and λ shows

little good agreement.

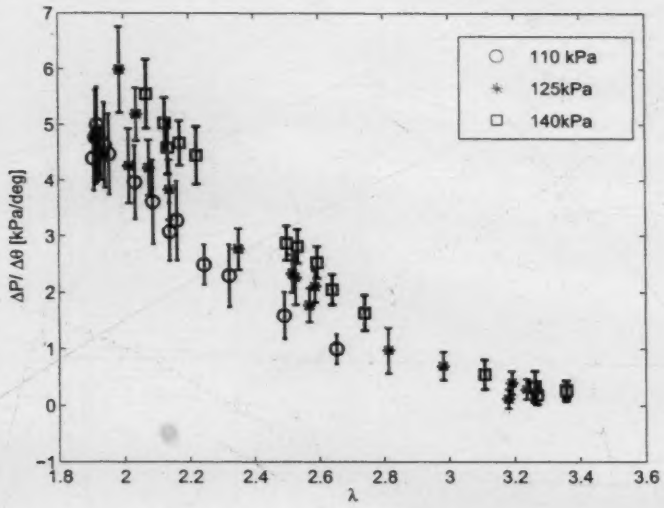

Figure 5.30: $\frac{\Delta P}{\Delta \theta}$ vs. λ for different MAP at N=1000rpm. Cases D, E and F of Table 4.3

An automotive production accelerometer used for sensing engine block vibrations is used for detecting knock in this study. This sensor is often termed a knock sensor, and that terminology is used here. A knock sensor signal of a single HCCI cycle showing "light" knock is shown in Figure 5.34 along with the unfiltered in-cylinder pressure trace for that cycle. In Figure 5.34 as the combustion pressure rapidly rises a distinct correlation with the increase in amplitude of the knock sensor signal can be seen.

To analyze the frequency content of the knock sensor signal, a power spectrum estimate is performed using Welch's method [Press et al., 1992]. A 512 point FFT with a Hamming window with 50% overlap is used. The raw knock signal shown in Figure 5.34 has a PSD shown in Figure 5.35. The modes $\rho_{1,0}$ and $\rho_{3,0}$ (see Figure 4.1) can be seen in this cycle, along with the mode frequency estimated using Eqn. 4.2,

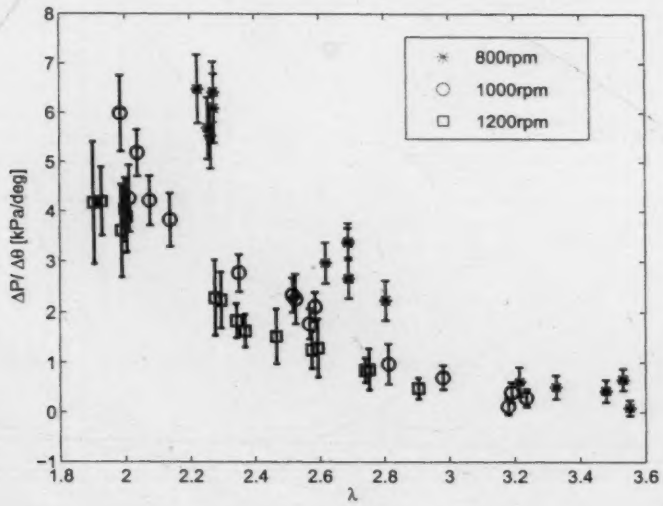

Figure 5.31: $\frac{\Delta P}{\Delta \theta}$ vs. λ for different Engine Speed, MAP=125kPa. Cases E, G and H of Table 4.3

with the temperature in the equation evaluated at the estimated maximum cylinder temperature for this cycle. The first circumferential mode $\rho_{1,0}$, with a frequency of approximately 6kHz, can be seen to be the dominant mode of oscillation in the chamber, with higher frequency modes also present.

To characterize the knock intensity, K_{int}, the magnitude of $\rho_{1,0}$, the first circumferential mode of the knock sensor signal is analyzed. As the characteristic knocking frequency is a function of the in-cylinder temperature, the knocking frequency changes not only with the engine operating condition and increasing load, but also within the cycle as the piston descends, lowering the temperature. To reduce the sensitivity of the evaluation of K_{int} on these factors, the average power estimated in the frequency range of 5-7kHz is used to determine K_{int}. Since the PSD estimates the signal power in units of V^2, while the signal itself is directly proportional to the pressure oscillations measured in the engine block, the square root of the average PSD in the relevant

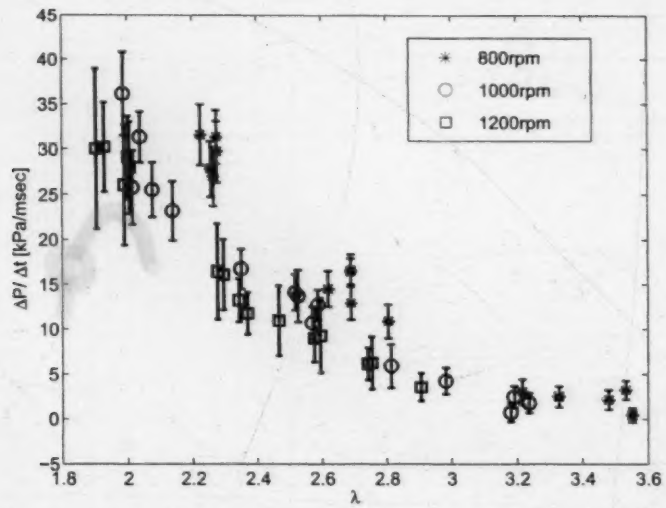

Figure 5.32: $\frac{\Delta P}{\Delta \theta}$ time vs. λ for different MAP at N=1000rpm. Cases E, G and H of Table 4.3

frequency range is taken. The equation for evaluating K_{int} is:

$$K_{int} = \sqrt{\frac{1}{7000 - 5000} \int_{5000Hz}^{7000Hz} PSD_{knock} df} \tag{5.8}$$

The value of K_{int} evaluated using Eqn. 5.8 is compared with the test averaged value of $\frac{\Delta P}{\Delta \theta}$ for three engine speeds, in Figure 5.36. The K_{int} is compared against BD_{time} in Figure 5.37. Decreasing combustion durations result in a larger value of the K_{int} as determined by the knock sensor. The shortened combustion event results in a greater stimulation of the pressure oscillations, and greater accelerations detected by the knock sensor.

As shown in Eqn. 4.2 the knocking frequency is a function of the in-cylinder temperature. To evaluate the knocking frequency, K_{freq}, the maximum of the PSD in the 5-7kHz range is found. A comparison of the estimated maximum cylinder temperature averaged over the cycles of a test, compared with the average value of K_{freq} is shown

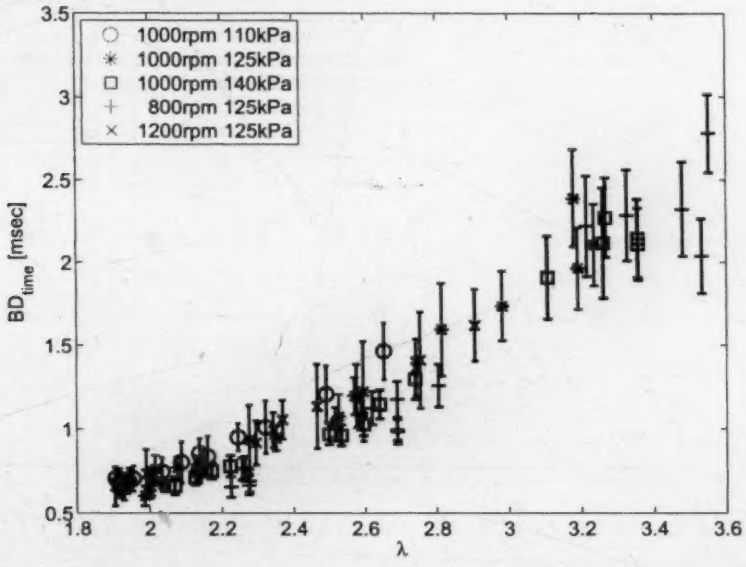

Figure 5.33: $\frac{\Delta P}{\Delta \theta}$ vs. λ for different MAP at N=1000rpm. Cases D-H of Table 4.3

in Figure 5.38. At low loads, the maximum cylinder temperature decreases significantly due to reduced temperature rise of combustion. The value of $\frac{\Delta P}{\Delta \theta}$ also decreases significantly for values of λ (and hence generally low loads due to the lean mixture), as shown in Figure 5.30. This reduction in $\frac{\Delta P}{\Delta \theta}$ results in a reduction in the vibrations induced to the engine block. With these low levels of vibration, the signal to noise ratio of the knock sensor is reduced, reducing the ability of this frequency estimation technique due to the lower signal to noise ratios. Also shown in Figure 5.38 with the dashed line, is the result of combining Eqn. 4.2 with Eqn. 4.10 to determine the estimated frequency for each value of T_{max}. While the general trend of the theoretical value is followed, a bias remains, especially for low values of T_{max}. In this analysis, the peak amplitude of the knocking is assumed to occur at the frequency associated with T_{max}. The bias between the estimated and experimental values may be due to the fundamental estimation of the mode number, which is derived for a cylindrical

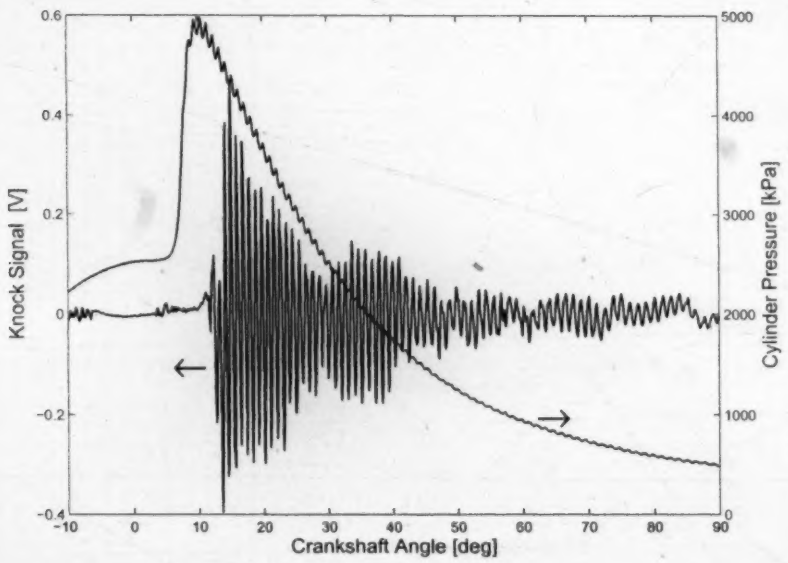

Figure 5.34: Raw Signal from Knock Sensor with In-cylinder Pressure. Test SS27 cycle 155.

combustion chamber. A difference of up to 10% of the mode number of a perfectly cylindrical chamber compared with the value derived from a finite element model of a typical pent-roof combustion chamber [Scholl et al., 1998]. The error in estimating this mode number based on the combustion chamber shape alone represents the bias seen in the data. Another source of error is the estimated ideal gas constant, R. Here this is estimated to be a constant of 0.287kJ/kgK, however the mixture gas constant is a function of temperature as well as mixture stoichiometry [Heywood, 1988]. To estimate the ideal gas constant as a function of these parameters an analysis including compositional changes throughout the cycle is required. To fully understand the effects of these compositional changes throughout the combustion event, thermo-kinetic modeling [Kirchen et al., 2007, Kongsereeparp and Checkel, 2007] is required, which is beyond the scope of this work.

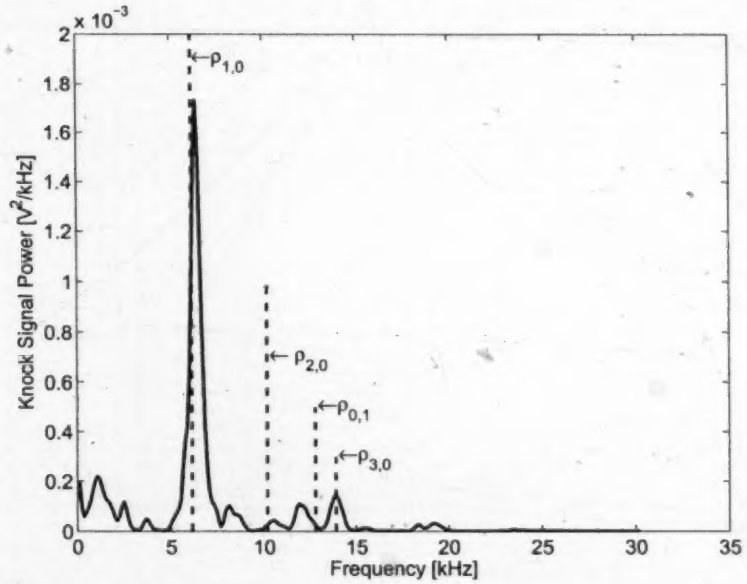

Figure 5.35: Estimated Power Spectral Density of Knock Trace. Test SS27 cycle 155.

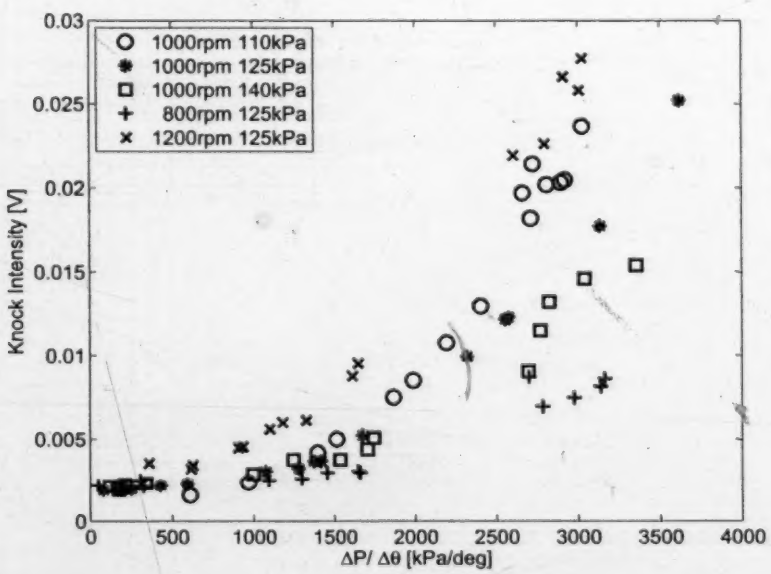

Figure 5.36: Knock Intensity vs. Combustion Pressure Rise Rate. Test Cases D-H.

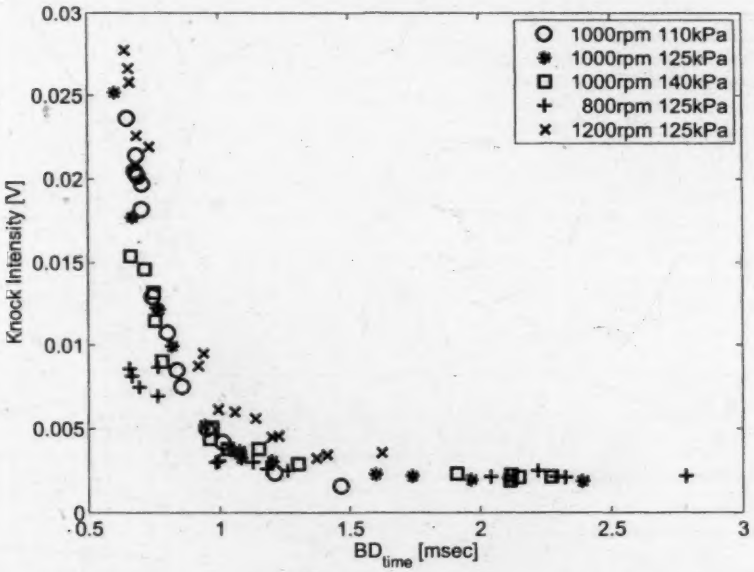

Figure 5.37: Knock Intensity vs. Burn Duration. Test Cases D-H.

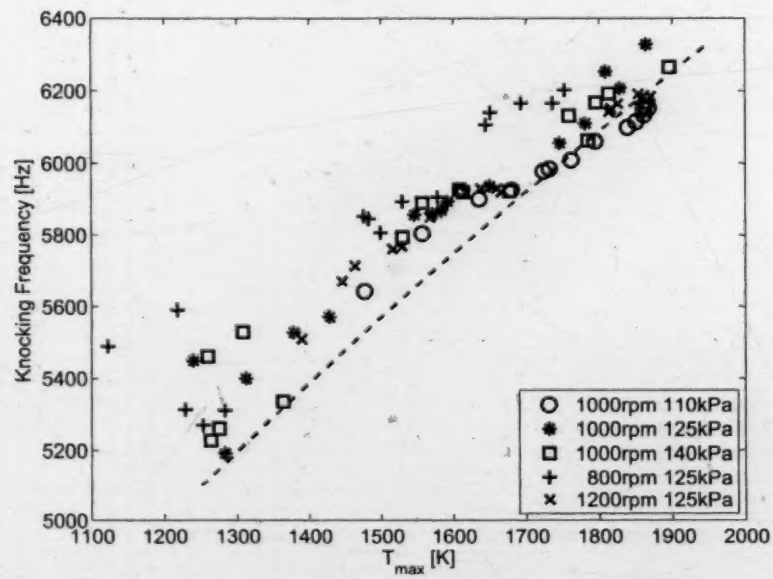

Figure 5.38: Knocking Frequency vs. T_{max}. Test Cases D-H.

5.4 Transient Results

The results of the step and pulse load transient tests are presented in this section. The transient tests are analyzed using the same analysis techniques shown in Section 4.4.

In Figure 5.39 the HCCI step load transients of test points TR33 and TR34 is shown with some important measured, and estimated parameters. A zoomed in version of the transients is also shown in Figure 5.40. All load transients are summarized in Table 4.6. Additional tests in Table 4.6 are shown in Appendix A. The SOC measured by $CA5_{HTR}$, $\frac{\Delta P}{\Delta \theta}$, T_{TDC}, HR_{LTR}, T_{IVC}, IMEP, and λ for each cycle is plotted. $CA5_{HTR}$ and λ are shown with the same scaling on all figures in order to compare the effect of the transient with different operating conditions while the other parameters are scaled appropriately for the particular case. For the step tests in Figures 5.39 and 5.40 the load transient occurs at engine cycle zero. Both the minimum to intermediate and minimum to maximum load transients are shown in each figure.

Figure 5.40 is a magnified view of the step change from the minimum load to the maximum load shown in Figure 5.39, showing the transient. Figure 5.40 is used as as example transient which will be used as an example to describe the transient response.

For the engine cycles less than zero (indicating they are before the transient occurs) the $CA5_{HTR}$ is constant with some cycle to cycle variation. At engine cycle zero, the load is increased by simultaneously decreasing $\mathrm{PW}_{heptane}$ and increasing PW_{octane} to the values known to give the setpoint combustion timing in the steady state. $CA5_{HTR}$ then increases from the initial setpoint value through a transient, and then $CA5_{HTR}$ converges to the new steady state value after several hundred engine cycles, as shown in Figure 5.39. The value of $\frac{\Delta P}{\Delta \theta}$ follows a similar trend through the transient, with very low combustion rise rates before the transient of ~20kPa/deg (indicative of the low load condition), a 15 cycle transient state value, and then convergence toward

the higher load steady state value.

Analysis indicates that the fueling transient is causing a delay in the proper fueling to the cylinder. This effect would be similar that noted in load transients in SI engines, in which the fuel has wall wetting dynamics [Fekete, 1995]. This effect occurs during a transient, where less fuel enters the cylinder due to wall wetting, which is often modeled as a first ordered response that is temperature dependent [Heywood, 1988, Maloney, 1999]. If the fueling in the cylinder follows a first order response then IMEP.

In Figure 5.40 IMEP does not follow a first order response, but rather makes a sharp step indicating the proper fueling is indeed entering the cylinder. Wall wetting dynamics seem unimportant for this case of a warm engine and relatively low engine speed. In Figure 5.40 the dip in IMEP between engine cycles 0-10 is due to the retarded combustion timing that occurs over this period of cycles.

The effect of the fuel puddle transient is also likely to be small, as the T_{int} for many of the test cases is at or near the boiling point of the fuels, of approximately $99°C$ shown in Table 4.1. As the fuel is injected well before the intake stroke, the fuel is likely nearly all vaporized as it enters the cylinder and thus less susceptible to the fuel puddling phenomena. Indeed in [Stone et al., 2000] for intake port surface temperatures exceeding $\sim 90°C$ even a stoichiometric quantity of iso-octane vaporizes at an engine speed of 1000rpm. While there is significant deposition of fuel droplets on the port surface, nearly complete vaporization occurs during the cycle.

A test in SI mode is done with pure iso-octane fueling to determine whether the vaporization effect is significant at HCCI relevant conditions, but without the sensitivity of the HCCI combustion to contend with. This test is shown in Figure 5.41 where the engine conditions are: T_{int} of $73°C$, MAP of 86kPA in SI mode. The fueling is stepped from rich of stoichiometric (λ =0.91) to lean of stoichiometric (λ =1.07) to determine if wall wetting dynamics are significant at these conditions. The transient response of IMEP is sharply defined with the stepped values of PW_{octane}. Aside from

the cycle to cycle variations typical of SI mode, the changes in IMEP occur within one engine cycle, indicating that an immediate step in fueling occurs. With the stepped values of PW_{octane} the value of λ can be seen to exhibit a similar response time as for HCCI transient tests, with a time constant of several engine cycles. This is due to the response time of the UEGO sensor mounted in the engine exhaust.

A look into the thermal effect of the residual and the LTR region, and their potential effects on the HTR combustion phasing shows a different mechanism is likely responsible for the transient behavior. The progression of the estimated cylinder temperature through each cycle is shown, through the values of T_{IVC}, the magnitude HR_{LTR}, and T_{TDC}. Immediately following the increase in load, the T_{IVC} can be seen to increase for several cycles. Physically this is attributed to a late combustion phasing resulting in a slightly increased residual temperature, due to a lower expansion by the piston. The incoming charge (assumed at a constant temperature) therefore mixes with residual at a higher temperature, resulting in T_{IVC} being increased. This effect alone would result in a T_{TDC} that is higher than that of the previous cycles due to the amplification of the pressure by the compression stroke. However, in these tests the opposite actually occurs, with the T_{TDC} reduced from the previous cases, even though T_{IVC} is increased. A look at the HR_{LTR} shows the reason for this reduced temperature, as in these same cycles there is a reduction in the HR_{LTR}. The reduced HR_{LTR} results in a T_{TDC} that is reduced from the previous cycles despite the increased T_{IVC}.

Similar behavior in the transient SOC (as measured by $CA50$) for a dual fuel commercial diesel engine operated in HCCI using n-heptane and ethanol as a fuel is documented [Bengtsson, 2004, Wilhelmsson et al., 2005]. These studies attribute the transient behavior of the SOC to a vaporization effect during the intake stroke reducing the temperature of the in-cylinder charge for these few cycles. The increased vaporization during the transient should cause a reduction in the P_{IVC} for these cycles

during the transient. In this thesis, since the in-cylinder temperature at TIVC is based on the Ideal Gas Law and P_{IVC}, any fuel vaporization effect on P_{IVC} is included in the estimation of T_{IVC}. Here T_{IVC} is seen to increase during the initial load transient and the measurement of $\dot{m}_{air}$ indicates no significant change in air flow rate through these transients. Thus this study contradicts the previous work, indicating these transient effects are due to fuel vaporization.

The cause for the reduction in HR_{LTR} during the load transient is not readily apparent from current investigation. An experimental study by [Sjoberg et al., 2007] shows that the LTR's involved in combustion of n-heptane (in particular PRF of ON 80) show a particular sensitivity to the concentration of O_2, as well as H_2O. A further analysis of the cycle to cycle coupling of the residual with inclusion of the compositional effects of the residual is required to determine the cause of the reduced HR_{LTR} seen in Figure 5.40.

Pulse tests are performed in a similar manner to Step tests; however, the fueling is returned to the low load condition after 200 engine cycles. An example of this type of test is shown in Figure 5.42. A zoomed in plot of the increasing load step is shown in Figure 5.43. The increasing load step exhibits a similar behavior to the Step tests already examined. The decreasing load step shows the inverse behavior of the increasing load step. A close up of this area of the test is shown in Figure 5.44. As the load is decreased the combustion timing advances, increasing the combustion pressure rise rate from that of the steady state case. The value of T_{IVC} is also lower than that of the steady state low load case.

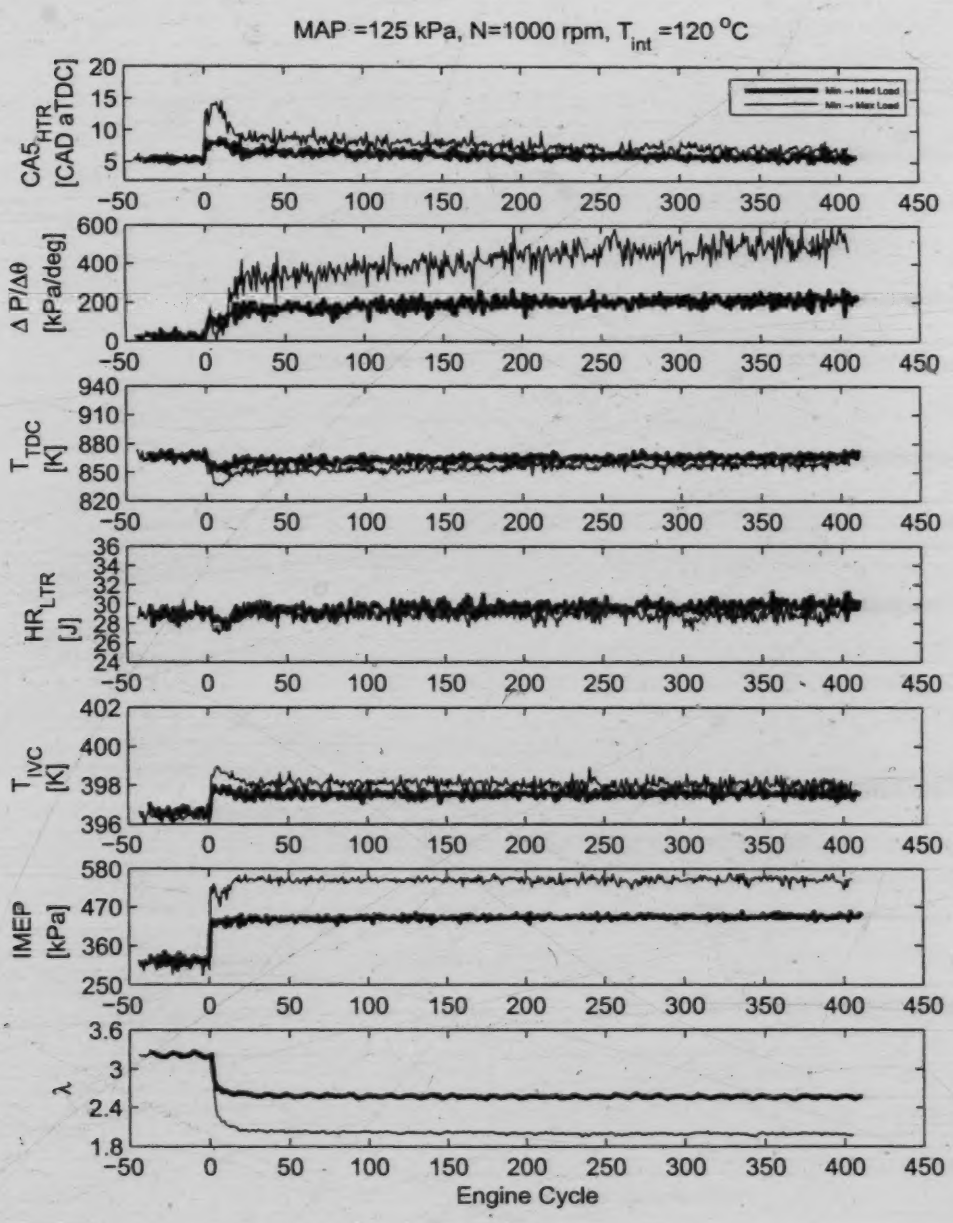

Figure 5.39: Combustion Metrics Through a Step Load Transient. Test Cases TR33 and TR34.

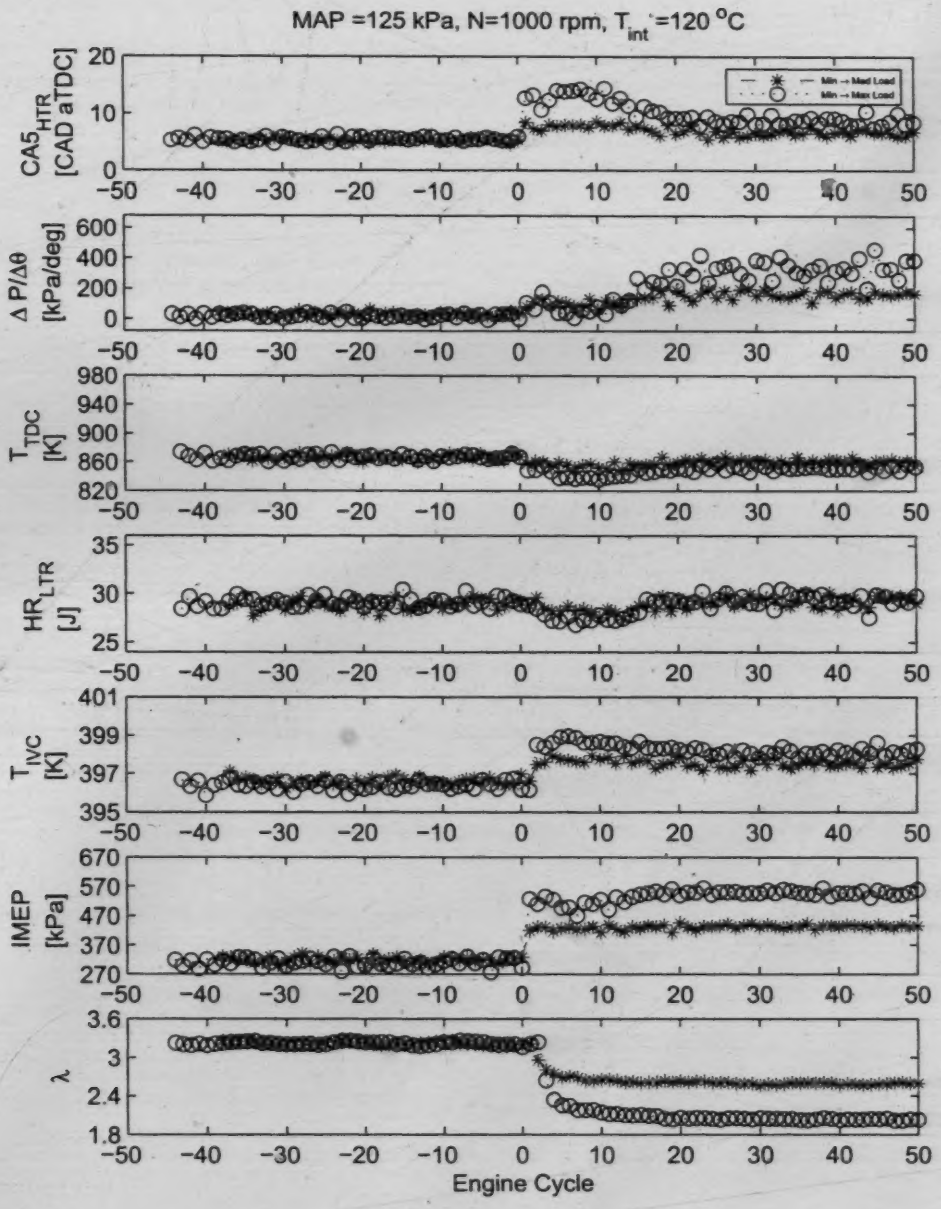

Figure 5.40: Close Up of Figure 5.39. Combustion Metrics Through a Step Load Transient. Test Cases TR33 and TR34.

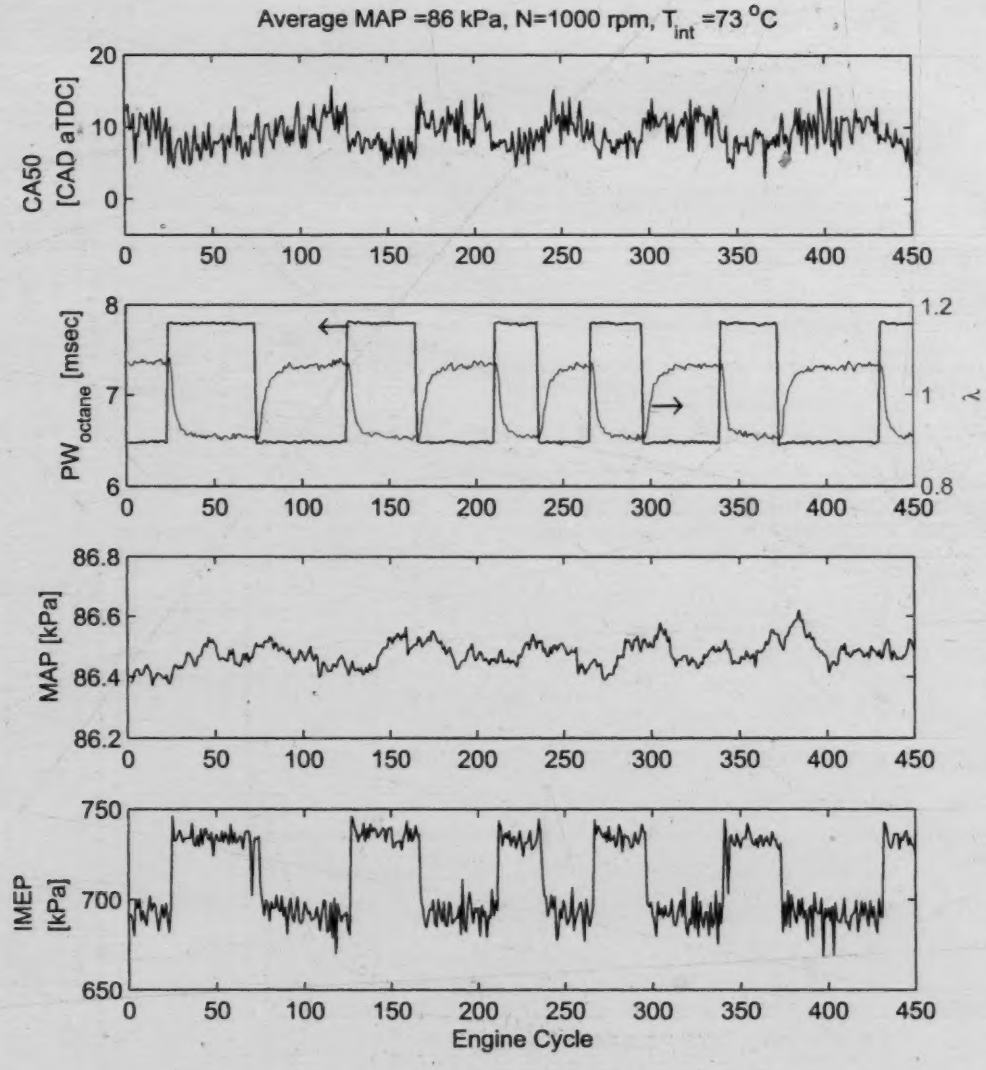

Figure 5.41: Perturbation of Iso-octane Fueling in SI Mode

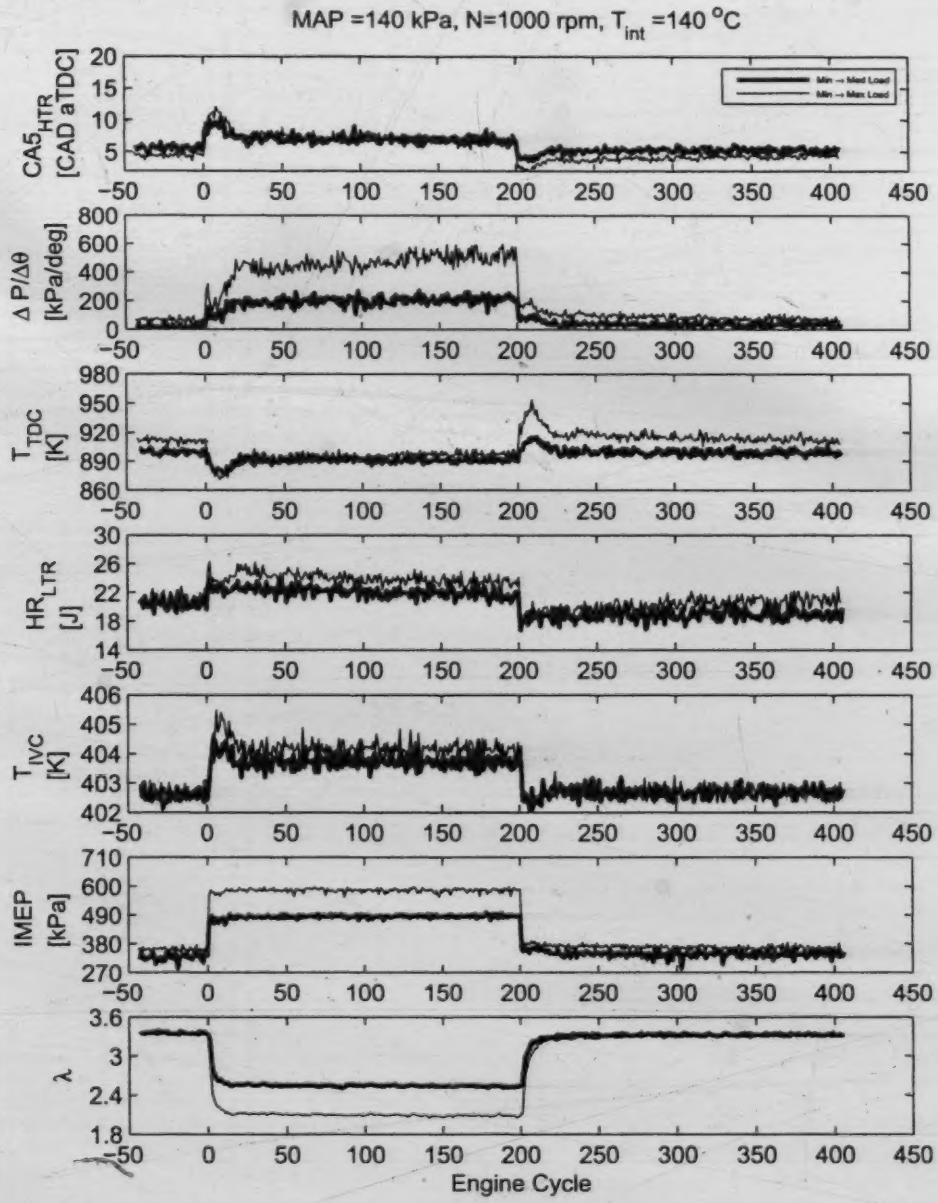

Figure 5.42: Combustion Metrics Through a Pulse Load Transient. Test points TR59 and TR60.

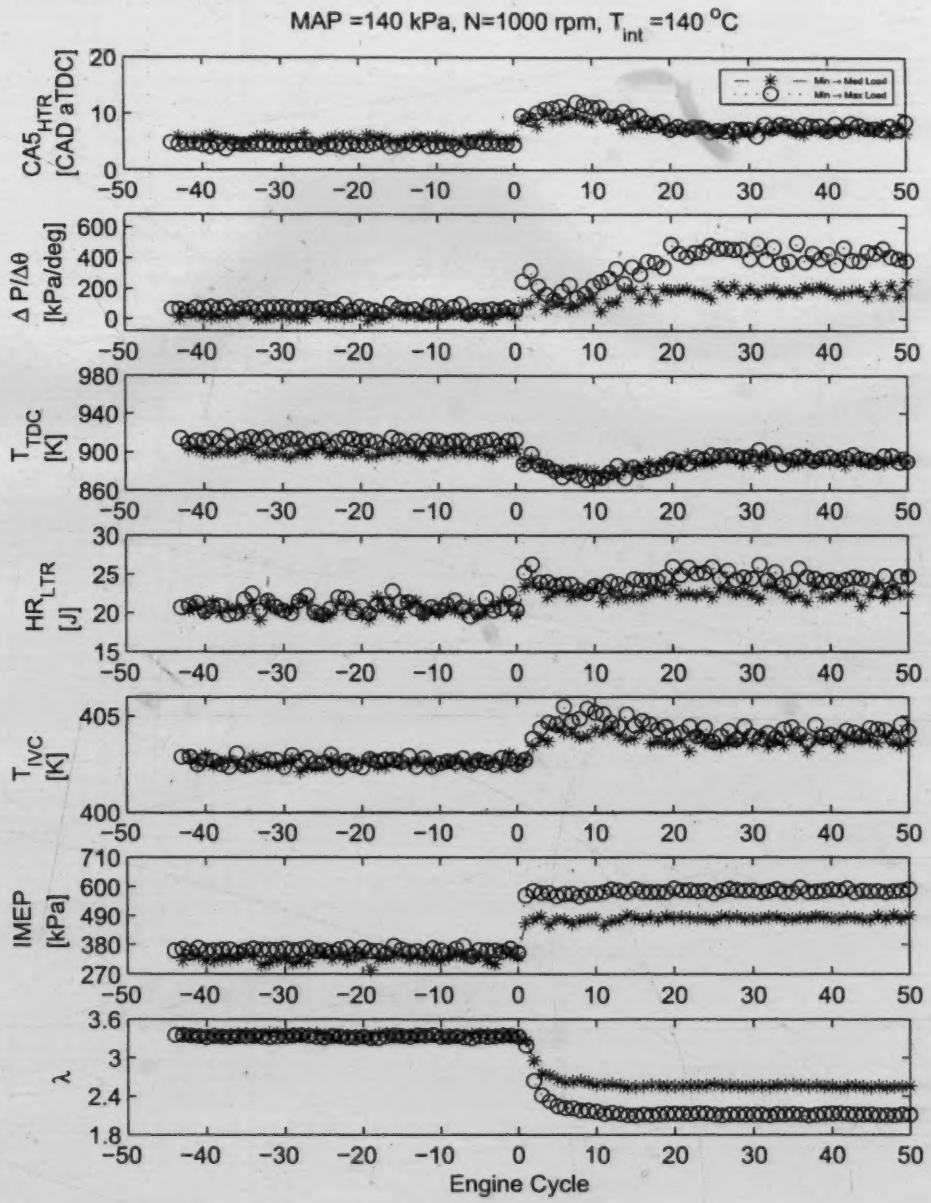

Figure 5.43: Combustion Metrics Through a Pulse Load Transient. Test points TR59 and TR60.

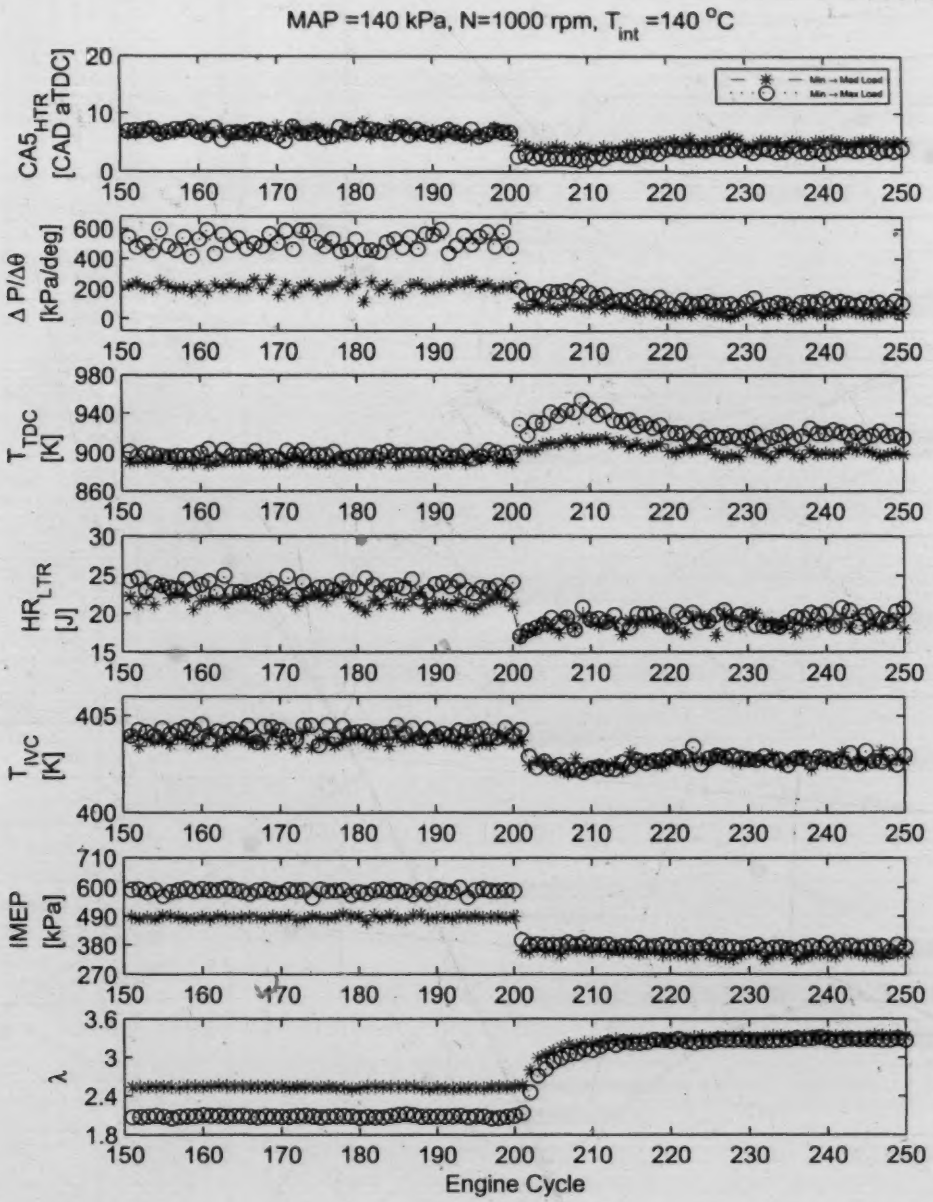

Figure 5.44: Combustion Metrics Through a Pulse Load Transient. Test points TR59 and TR60.

5.5 HCCI to SI Mode Transitions

Mode transitions between SI and HCCI combustion are presented in this section. This mode transition is crucial to real applications since HCCI is not viable over the entire load-speed range [Kulzer et al., 2007].

With the relatively low compression ratio engine used in this study (10:1), HCCI is only viable for relatively low ON's, as shown in Figure 5.7 and Figure 5.8. Supplying the engine with n-heptane (ON of 0) which promotes auto-ignition and allows HCCI, along with a separate supply of iso-octane (ON of 100) allowing SI operation without knock, the possibility exists for SI-HCCI mode transitions using fuel actuation. In addition, since for the operating conditions tested in this study (fully warm engine with above ambient values of T_{int}) fuel film dynamics are insignificant (see previous section), the two fuel strategy can effectively be used to control the combustion.

To enable SI-HCCI transitions the ECU is programmed with an open loop look-up table for fueling, in both SI and HCCI modes. A software switch is used to command the engine from stoichiometric SI mode, to HCCI mode, and to determine which mode (HCCI or SI) to utilize.

An engine speed of 1000rpm is used for the mode switching testing as it matches the majority of the steady state test cases in Table 4.3. The quantity of n-heptane is used to control combustion timing, while the total quantity of n-heptane and iso-octane is used to control the engine load [Tanaka et al., 2003b]. As shown in Section 5.3 the mass of n-heptane is nearly constant when going from the minimum load to the maximum load condition, at a given operating point when the combustion timing is maintained. To determine the necessary n-heptane quantity to maintain the fixed combustion timing ($CA5_{HTR}$ of 7 CAD aTDC) at a given T_{int} and MAP at 1000rpm, a mapping of the steady state tests performed is done. Shown in Figure 5.45 are the steady state experimental points marked with an 'o', as well as the generated

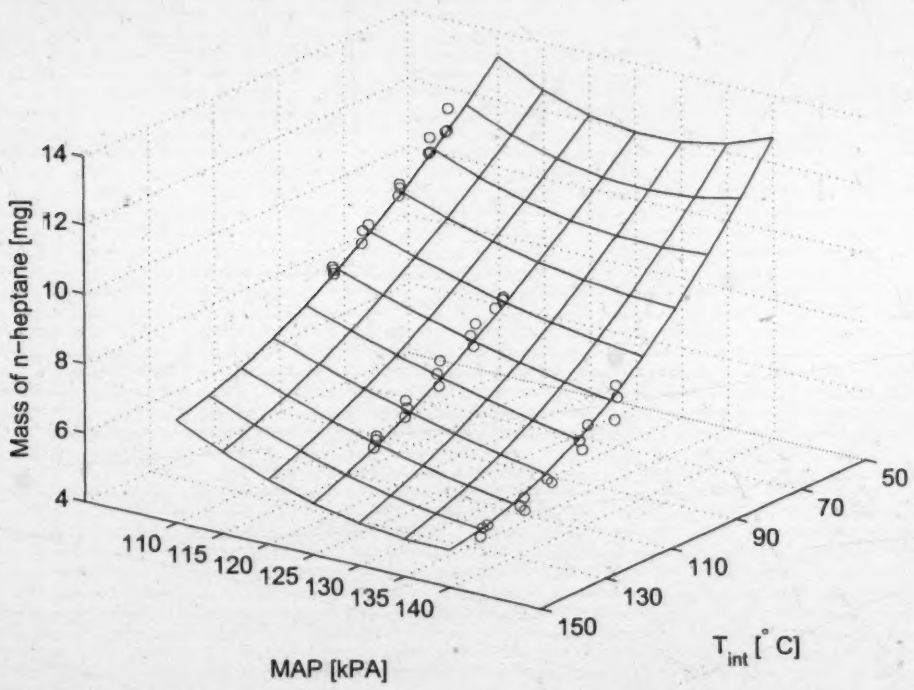

Figure 5.45: Lookup table of mass of n-heptane required as a function of T_{int} and MAP for HCCI combustion with $CA5_{HTR}$ of 7 CAD aTDC. Tests SS1-SS45.

lookup table values. To generate the lookup table values a quadratic fit is performed for each MAP, of the mass of n-heptane vs T_{int} for a 50-150°C of T_{int}. Then each quadratic fit is interpolated along the MAP direction with another quadratic from 110kPa to 140kPa, to fill in the 2-D lookup table. The final lookup table has resolution of 10°C in the T_{int} direction and 5kPa in the MAP direction, giving a final table size of 7x11. Linear interpolation is used for points within the map, and linear extrapolation is used for points outside of the lookup table boundaries. With the two-dimensional lookup table based on MAP and T_{int}, no compensation for changes in engine speed (off of the 1000rpm setpoint) is made.

Speed-Density is used to schedule fueling for the engine in SI mode. This method

of engine control assumes the Volumetric Efficiency (VE) of the engine is strictly a function of MAP and N (albeit N is constant for this study). To calculate the quantity of fuel to inject the algorithm uses Eqn. 5.9 and Eqn. 5.10. The desired mass of fuel (in this case solely iso-octane) to inject, m_f, is determined from the desired AFR is AFR_{des}, which here is the stoichiometric AFR of iso-octane of 15.1:1. An experimentally tuned lookup table of VE=f(MAP,N) is used to maintain the value of λ of 1. Stoichiometric operation is used in SI mode to meet the requirements of modern three-way catalytic converters, which require stoichiometric operation to maintain optimum efficiency of simultaneously reducing CO, UHC, and NO_x emissions [Heywood, 1988]. The SI fueling is:

$$m_{int} = \frac{VE \times V_{disp} \times MAP}{R \times T_{int}} \tag{5.9}$$

$$m_f = \frac{m_{int}}{1 + AFR_{des}} \tag{5.10}$$

The SI and HCCI lookup tables are programmed with Matlab/Simulink into the dSpace ECU. The final values of the injector pulse widths are determined by using Eqn. 3.1 with injector flow rate constants determined in Appendix B.2.3. With the engine operating in SI mode, the throttle angle and the supercharger speed can be controlled (through the ADAPT software) to control the MAP of the engine. The load of the engine, with the Speed-Density algorithm maintaining the the AFR at stoichiometric, is thus actuated by varying MAP. In HCCI mode, the values of T_{int} and MAP can be changed with the ECU using the n-heptane table to adjust the $PW_{heptane}$ to maintain the maintain proper combustion timing. To control the load of the engine in HCCI mode a setpoint for the total fuel energy (in terms of LHV) of fuel to be injected to the engine can be set in the ECU according to:

$$Q_{total} = Q_{hep} + Q_{oct} = LHV_{heptane} \times m_{heptane} + LHV_{octane} \times m_{octane} \quad (5.11)$$

The ECU uses the value of the required n-heptane (determined by the lookup table), to maintain proper combustion timing, and the operator specified value of Q_{total} for total fuel quantity to be delivered, to calculate $\mathrm{PW}_{heptane}$ and PW_{octane}.

5.5.1 Mode Transitions at Constant MAP

To evaluate combustion stability through a mode switch the engine is switched from HCCI to SI and back to HCCI at constant MAP. Recorded in Figure 5.46 as a function of engine cycle is the complete record of the mode switching process. A close up of the mode transitions from SI-HCCI and HCCI-SI are shown in Figure 5.47. By switching between SI and HCCI fueling, the fuel injector PW's are determined using the lookup table appropriate for the combustion mode by the ECU. In Figure 5.46 it is apparent from $\mathrm{PW}_{heptane}$ and PW_{octane} when the mode switching is actuated. PW_{octane} is used exclusively in SI mode, while a combination of $\mathrm{PW}_{heptane}$ and PW_{octane} can be used in HCCI mode (although pure n-heptane is used in the case of Figure 5.46). The combustion timing (determined by $CA50$ rather than $CA5_{HTR}$ as there is no LTR combustion in SI mode) can be seen to change when the combustion mode is switched. The combustion timing in SI mode is at 10CAD aTDC which is 3CAD retarded from HCCI. The SI $CA50$ is set to this value by the spark angle, to prevent knock at this relatively high load condition (IMEP=8bar). The $CA50$ can be seen to advance on the first HCCI cycle, and then stabilize after approximately 15 cycles. The advanced combustion timing for the first HCCI cycle is attributed to the increased residual temperature, with the stabilization after switching from SI (over approximately 15 cycles) due to the same mechanisms as shown in Section 5.4.

The value of MAP can be seen to stay relatively constant through the mode transitions, with small fluctuations at the transitions, attributed to changes in back-flow of residuals into the intake manifold at the instant of IVO due to the different residual temperatures from SI and HCCI modes. The settling time of the UEGO measurement of λ occurs over approximately 3 engine cycles for the mode transitions. The response time of the UEGO sensor is listed as <150msec, or approximately 1 engine cycle at this engine speed. A wall wetting fueling dynamic is not likely, as found in Section 5.4. Dynamics associated with the transport of exhaust gases down the exhaust port and the cyclic nature of the engine also influence the response of the UEGO. The last SI cycle leaves exhaust residual with virtually no O_2 content (due to the stoichiometric operation) for the first HCCI cycle, the total stoichiometry of the first HCCI cycle is slightly richer than that of a steady state HCCI cycle. The opposite occurs when going from lean HCCI to stoichiometric SI, where a much larger quantity of O_2 is present in the residual fraction of the first SI cycle. Although the residual fraction is relatively small, on the order of 10% for this operating condition, this effect influences the value measured by the UEGO when drastically changing stoichiometry (such as at engine cycle 40 and 126). A dynamic model accounting for the previous combustion is needed to fully compensate for this effect.

A difference in IMEP from 800kPa in SI mode, to 400kPa in HCCI mode is apparent in Figure 5.46. The injected fuel energy for stoichiometric SI and lean HCCI are correspondingly large, while other operating conditions are held constant. The jump in IMEP shows that immediate changes in load can be achieved through SI-HCCI-SI modes. For both SI-HCCI and HCCI-SI transitions a small overshoot of IMEP is apparent which is attributed to the residual fraction dynamic as previously discussed. This type of mode transition would be useful to change from partial load (HCCI) to full load (SI) and back. No throttle movement or change in MAP is required for this transient.

The cylinder pressure traces going through a switch from HCCI to SI, are shown in Figure 5.48. The cylinder pressure traces for Figure 5.48 are taken from test MS8 shown in Figure 5.46, engine cycle 41 and 42. As MAP remains constant, and λ changes from $\sim$2 in HCCI mode, to $\sim$1 in SI mode, the injected fuel energy approximately double for SI mode, compared with HCCI. This results in a significantly higher IMEP for the SI cycle, and thus the noticeable change in area under the pressure traces. It should be noted that even the first SI cycle exhibits a good combustion cycle, without significantly retarded combustion, or misfire. The cylinder pressure traces of a switch from SI mode to HCCI mode, are shown with cycles 127 and 128 from test MS8 in Figure 5.49. The cylinder pressure traces are from Figure 5.46 with the engine cycles corresponding for both plots. There is a difference in IMEP over the transition, the first HCCI cycle also exhibits good combustion (albeit a small amount of knock is present). This knocking is attributed to higher cylinder wall temperatures from the SI operation at higher load, as well as increased residual gas fraction temperature for the first HCCI cycle.

5.5.2 SI-HCCI Mode Transitions at Constant Load

Another interesting mode transition case is one in which the load stays constant. To achieve this mode transition on this engine, the operating condition has to go from wide open throttle (and possibly possibly supercharged operation) for HCCI to a throttle position (and MAP) that achieves the equivalent load in SI operation, and back. The throttle angle and the supercharger speed are controlled by the dynamometer test bench (ADAPT RTP) and not the ECU. A logic gate is implemented in the ECU software which switches to HCCI if the conditions allow the energy of the n-heptane mass as derived from the HCCI lookup table, to be below the desired total injected fuel energy, and below a threshold value to prevent knock. The Matlab/Simulink representation of this logic condition is shown in Figure 5.50. This

logic allows HCCI only if the manually set value of the desired load is obtainable at the current engine operating condition. Otherwise the logic switches to SI mode at the given engine condition. To invoke an HCCI to SI mode transition the throttle is closed to reduce the MAP. As the MAP is reduced, the quantity of n-heptane required to maintain proper combustion timing increases, see Figure 5.9. Once the required energy of n-heptane exceeds the manually set limit, which is labeled 'Q_{total}' in Figure 5.50, the ECU reverts to SI mode using iso-octane fueling as derived from the Speed-Density algorithm. Once in SI mode, the load is determined exclusively by the value of MAP, as this dictates the stoichiometric fueling. The total fuel quantity allowed in HCCI mode is heuristically found to be 0.625kJ, as shown in Figure 5.50 under variable '$MaxHCCIQtotal$'. The multiport switch in Figure 5.50 is used to control whether the ECU is forced into either SI or HCCI modes, or is allowed to switch based on the logic structure. The ECU is programmed to turn on the spark at a fixed, but manually adjustable, spark angle in SI mode, and to turn the spark off in HCCI mode

Three tests where this mode switching technique is used are shown In Figures 5.51, 5.53, and 5.55. In each test the throttle is manually closed at arbitrary times to induced SI mode operation. For this experimental setup, at an engine speed of 1000rpm, the lowest value of MAP that can be obtained is approximately 65kPa. By fully closing the throttle, the engine produces approximately the same load in SI as an intermediate-high load HCCI point, this is caused by the throttle being over sized for the size of the single cylinder. This limits the effect of throttle valve, not allowing lower values of MAP to be achieved. The electronic throttle actuator is able to achieve a new throttle setting in under 0.1sec, or less than one engine cycle for N=1000rpm.

Shown in Figure 5.51 is test MS3, starting in HCCI mode at a MAP of 100kPa until cycle 50, where the throttle is closed, and the MAP begins to decrease. A close up of this portion of the test is shown in Figure 5.52. As the MAP decreases with the

closed throttle, the ECU switches to SI mode on the next cycle, as seen by the values of PW_{octane} and the turning off of $PW_{heptane}$. As the MAP on the first SI cycle is not at the steady state value, the Speed-Density algorithm supplies the fueling to achieve a λ of 1. This is visible by the initial peak in PW_{octane}, and the slow reduction in MAP. The value of λ can be seen to quickly approach a value of 1 after switching to SI mode. The value of $CA50$ throughout this transient remains relatively constant. By engine cycle 70 the value of MAP has approached the steady value, and the IMEP has achieved a value equivalent to that in the HCCI mode. To switch from SI to HCCI mode, at engine cycle 125 the throttle is once again opened, causing MAP to increase. The ECU remains in SI mode for several cycles, indicated by the value of PW_{octane} increasing as MAP increases and the delay in λ increasing compared with the value of MAP. At cycle 130, the first cycle where the energy of n-heptane is lower than the threshold value, the ECU switches back to HCCI mode. A zoomed in view is shown in Figure 5.52. A similar cycle repeats at engine cycles 220 and 295. While the value of $CA50$ stays constant throughout this test, the IMEP noticeably increases during the SI-HCCI and HCCI to SI transitions. This can be attributed to the long transient in MAP for this experimental setup.

Another mode transition test with a higher value of T_{int} is shown in Figure 5.53, where T_{int}=89°C and the MAP for HCCI is also higher at 115kPa. The throttle is closed, and the value of MAP begins to decreases at cycle 60. For this test, as the MAP decreases, an increase in $PW_{heptane}$ and a decrease in PW_{octane} can be seen before the transition to SI mode, as the ECU maintains HCCI mode for several cycles. Finally by cycle 68 the ECU commands a transition to SI mode and the injection changes to purely PW_{octane}. For this test the value of $CA50$ is slightly retarded from optimum in SI mode; however, the combustion remains stable. During this initial transition in HCCI mode, a small decrease in IMEP can be seen. Finally by cycle 65 the ECU switches to SI mode, and a similar transition occurs as in the previous case. On

cycle 190 as the throttle is opened once again, the ECU maintains SI mode for a few cycles before switching to HCCI mode. As the ECU switches to HCCI mode, again a peak in $PW_{heptane}$ before assuming the steady state value can be seen, as the ECU recognizes conditions favorable for HCCI. A more noticeable dip in IMEP can be seen as the transition is made back to HCCI mode. A similar cycle repeats at cycles 280 and 350 and is shown in Figure 5.54. A similar test is shown in Figure 5.55 with an initial HCCI MAP of 120kPa, with a T_{int} of $81°C$. A close up of the SI-HCCI and HCCI-SI mode transitions are shown in Figure 5.56.

A notable difference between the mode transitions in Figure 5.51, 5.53, and 5.55 is the smoothness of the SI-HCCI transition. For test MS3, in Figure 5.51 and Figure 5.52, the SI-HCCI transition creates a sharp rise in IMEP over approximately 10 cycles. This occurs as the mode switching logic of the ECU determines that HCCI is not possible until the MAP nearly reaches the steady value of 100kPa, which takes several cycles. For test MS7, shown in Figure 5.53 and Figure 5.54, the SI-HCCI shows a significantly smoother transition in IMEP. Within 4 cycles, the ECU determines that HCCI is possible, and commands HCCI fueling. The transition to a MAP of 115kPa in HCCI allows the transition to occur more smoothly. Assisting the SI-HCCI transition for test MS7 compared with MS3 is the increased value of T_{int} of case MS7. The higher value of T_{int} in MS7 causes the ECU to transition to HCCI more quickly, as less n-heptane is required for HCCI to occur with higher T_{int}, see Figure 5.45. The case with the least disturbance in IMEP in SI-HCCI mode transition is case MS1, despite the fact that T_{int} is lower in case MS1 than MS7. The higher MAP commanded in HCCI mode of case MS1, compared with tests MS3 and MS7, results in the smoother transition occurring in 3 cycles. The ability to supercharge in HCCI mode allows an SI-HCCI mode transition to occur more quickly than would be possible with natural aspiration.

The purpose of the open loop control system is to understand the dynamics of

mode transition, not necessarily to achieve a smooth transition. Thus the slow changes in MAP result in the ECU providing stoichiometric SI mode for several cycles before the MAP achieves its steady value. The duration of the MAP transient is related to the volume of the intake system between the throttle and the engine. Due to packaging constraints in the test cell, as well as the necessary duct work to supply air to the engine through the supercharger, the total intake volume between the throttle and the intake valve is approximately 10 times the displacement of the engine (whereas in a typical production engine the manifold volume is on the order of one engine displacement). An estimate of the duration of the time to reach 63% of the steady state value, the time constant, associated with the changes of MAP is 0.5sec for increasing MAP, and 0.9sec for decreasing MAP. The difference in time constants is due to the manifold filling (on throttle opening) being dominated by the throttle flow rate from atmosphere along with the intake manifold capacitance. The throttle flow rate is typically large, and is open to a constant pressure source (atmosphere), allowing filling to happen rapidly. For supercharged operation, manifold filling is a combination of throttle opening (supplying the inlet of the supercharger) as well as the ability of the supercharger to pressurize the manifold. By contrast the manifold emptying on throttle closing is dominated by the flow rate of air into the intake port of the engine, and the intake manifold capacitance. Since the engine only provides flow for one quarter of its cycle, and has a limited volume capacity it's ability to empty the manifold is reduced. [Chang, 1993] observes time constants ranging from 7-14msec for throttle opening, and 14-15msec for throttle closing on a single cylinder CFR engine at 1200rpm with an intake manifold of 40% engine displacement.

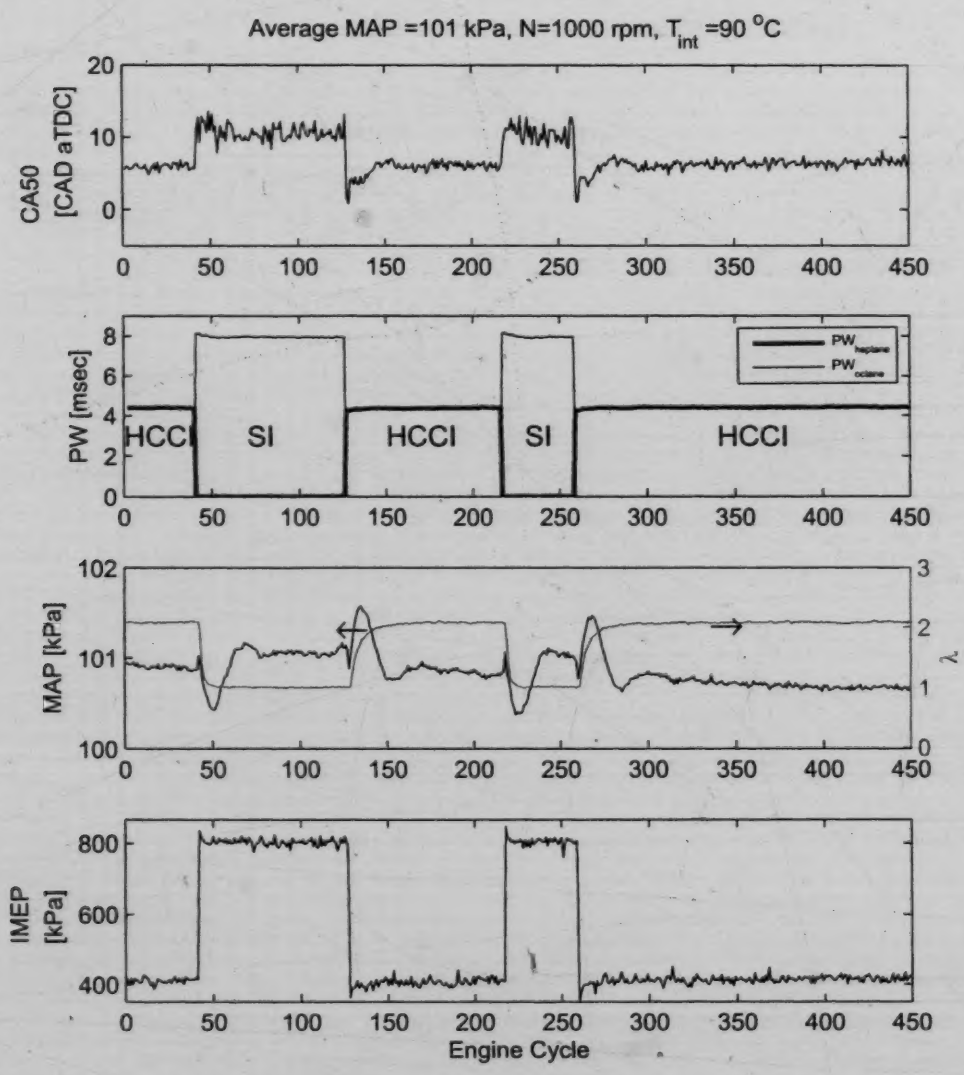

Figure 5.46: HCCI-SI Mode Switching with Constant MAP. Test MS8.

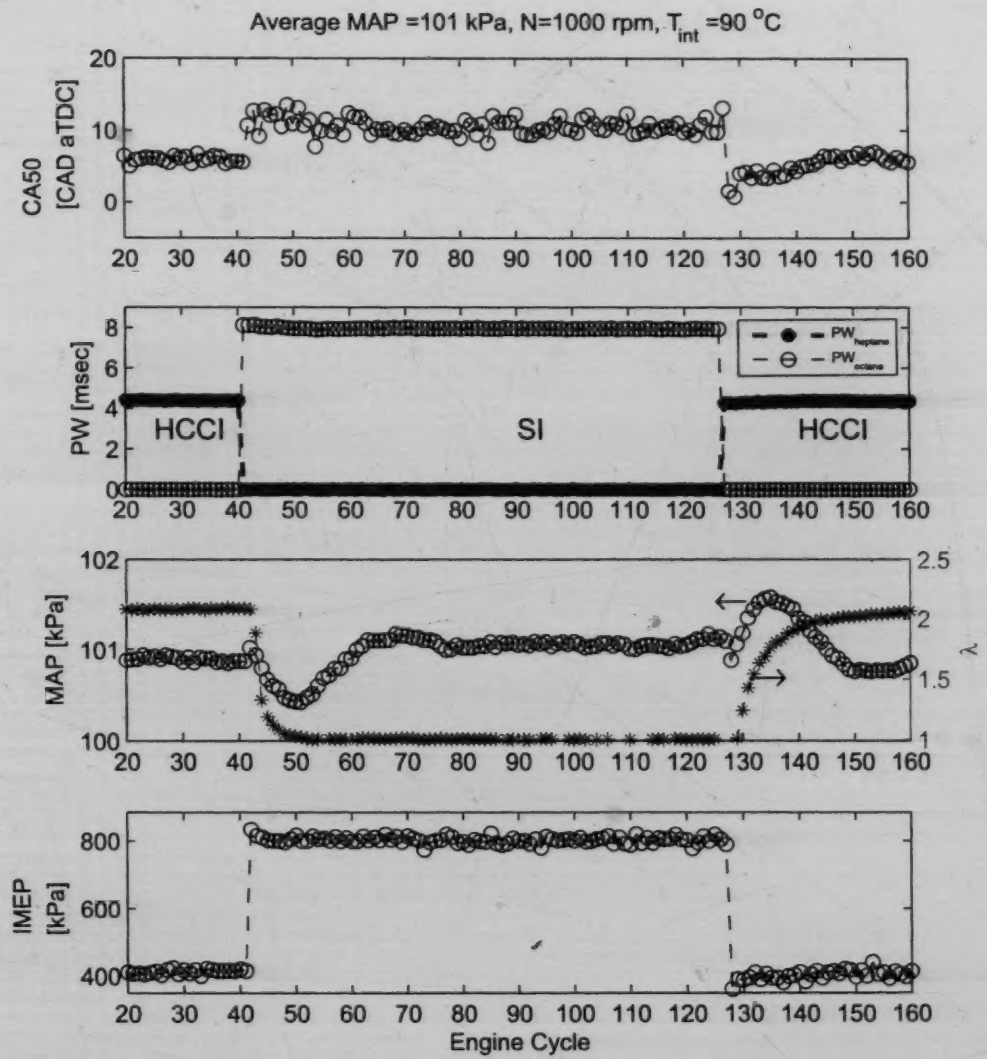

Figure 5.47: Close up of HCCI-SI Mode Switching with Constant MAP. Test MS8.

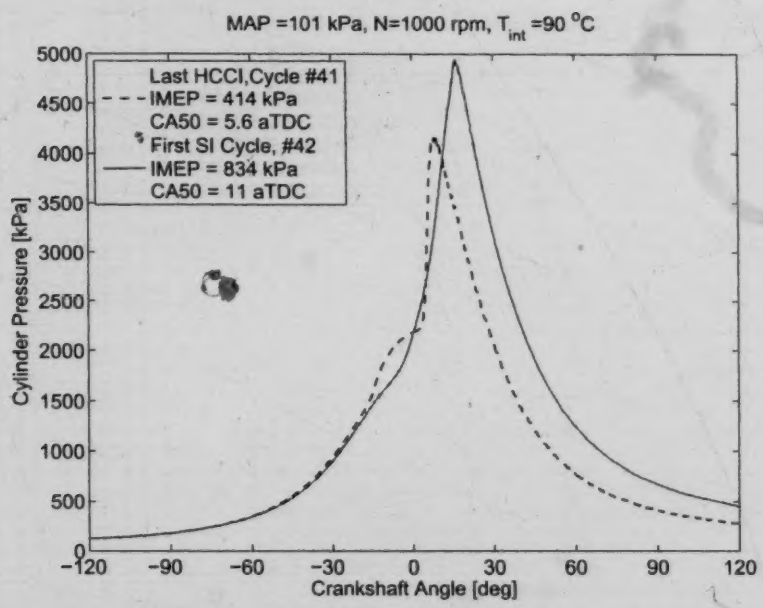
MAP =101 kPa, N=1000 rpm, T_int =90 °C
Last HCCI,Cycle #41
IMEP = 414 kPa
CA50 = 5.6 aTDC
First SI Cycle, #42
IMEP = 834 kPa
CA50 = 11 aTDC
Cylinder Pressure [kPa]
Crankshaft Angle [deg]

Figure 5.48: Last HCCI Cycle and First SI Cycle During a Mode Switch. Test MS8.

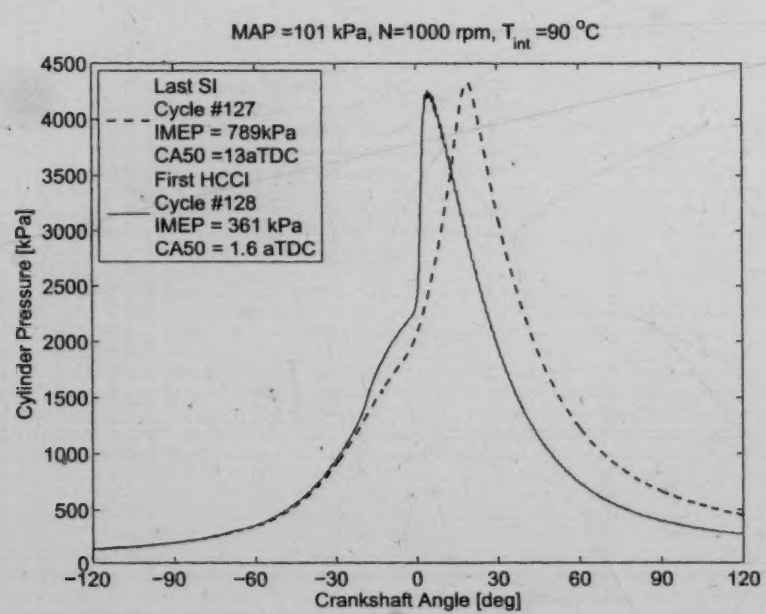

Figure 5.49: Last SI Cycle and First HCCI Cycle During a Mode Switch. Test MS8.

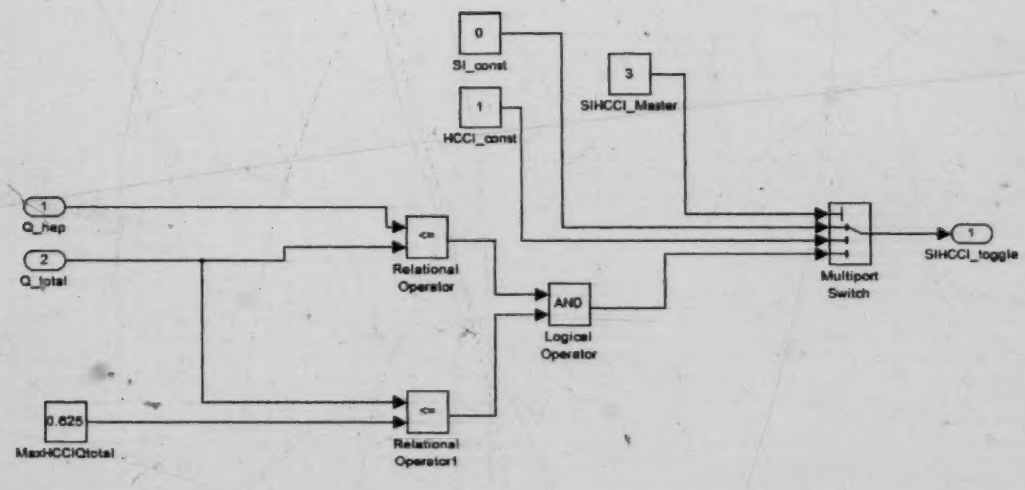

Figure 5.50: Simulink Block Diagram of HCCI to SI Switching Logic

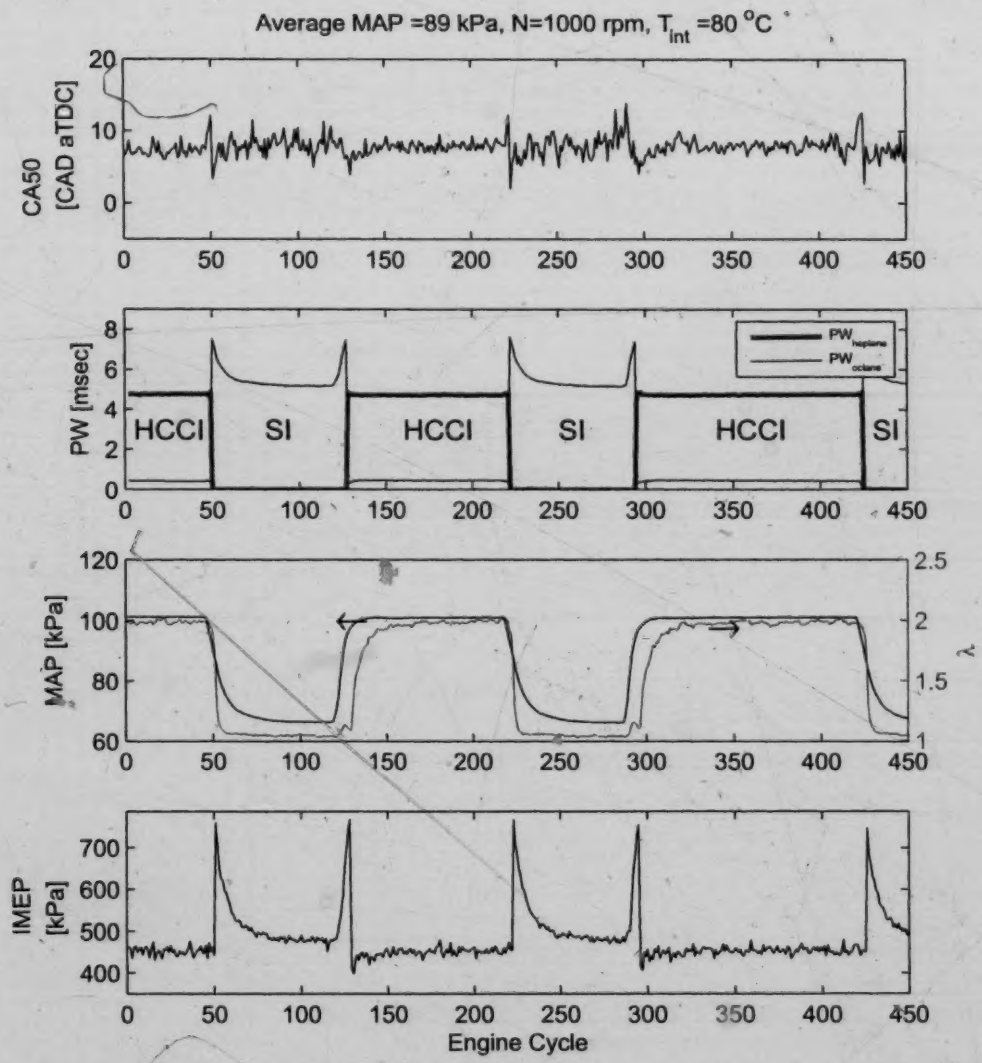

Figure 5.51: HCCI-SI Mode Switch with Similar Steady State Loads, HCCI MAP 100kPa. Test MS3.

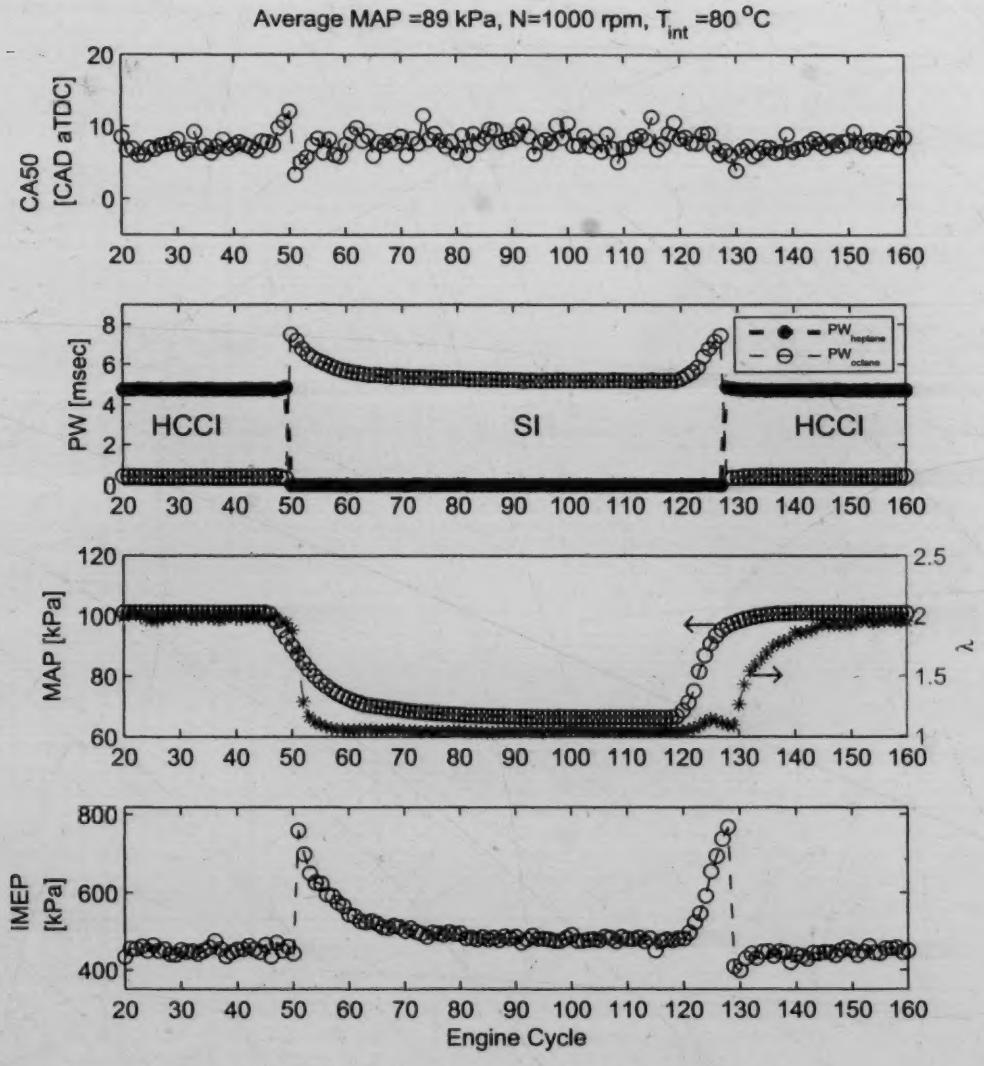

Figure 5.52: Close Up of HCCI-SI Mode Switch with Similar Steady State Loads, HCCI MAP 100kPa. Test MS3.

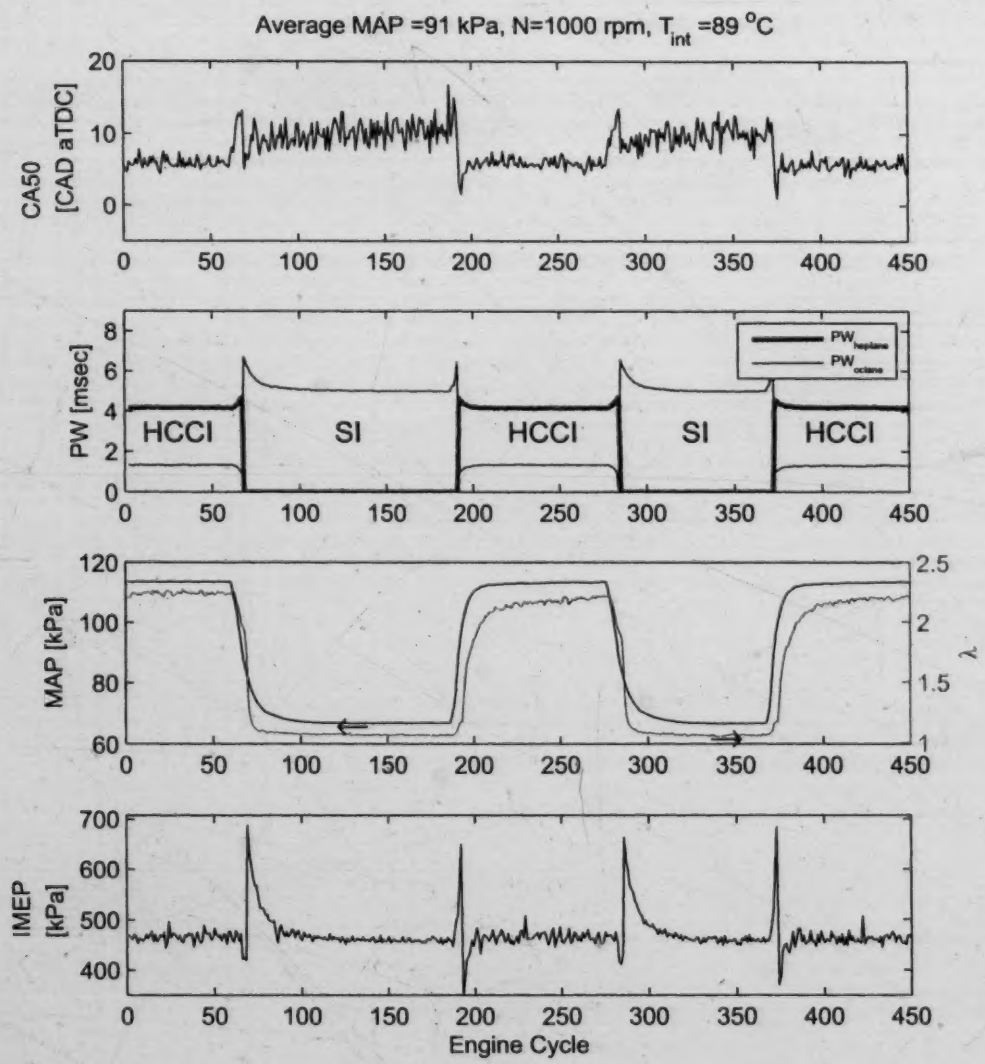

Figure 5.53: HCCI-SI Mode Switch with Similar Steady State Loads, HCCI MAP 115kPa. Test MS7.

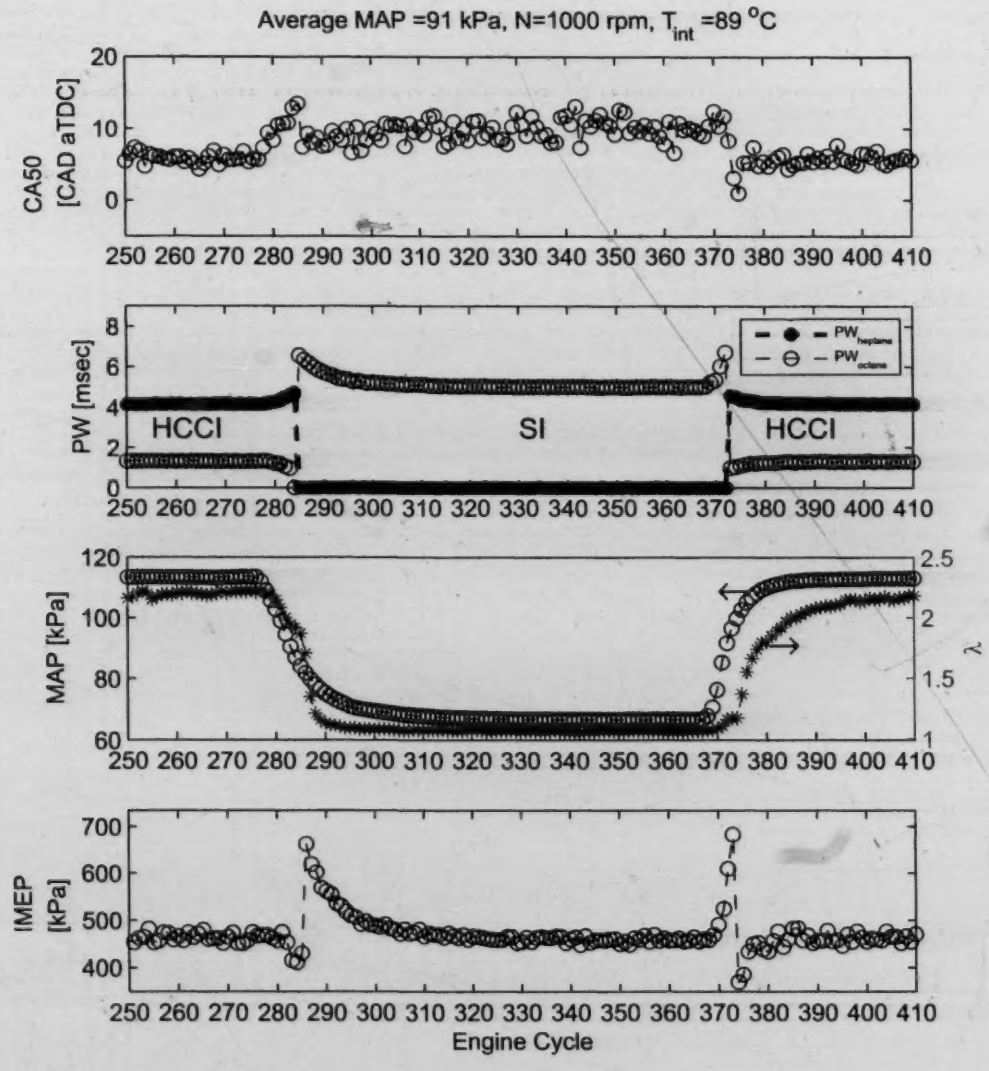

Figure 5.54: Close Up of HCCI-SI Mode Switch with Similar Steady State Loads, HCCI MAP 115kPa. Test MS7.

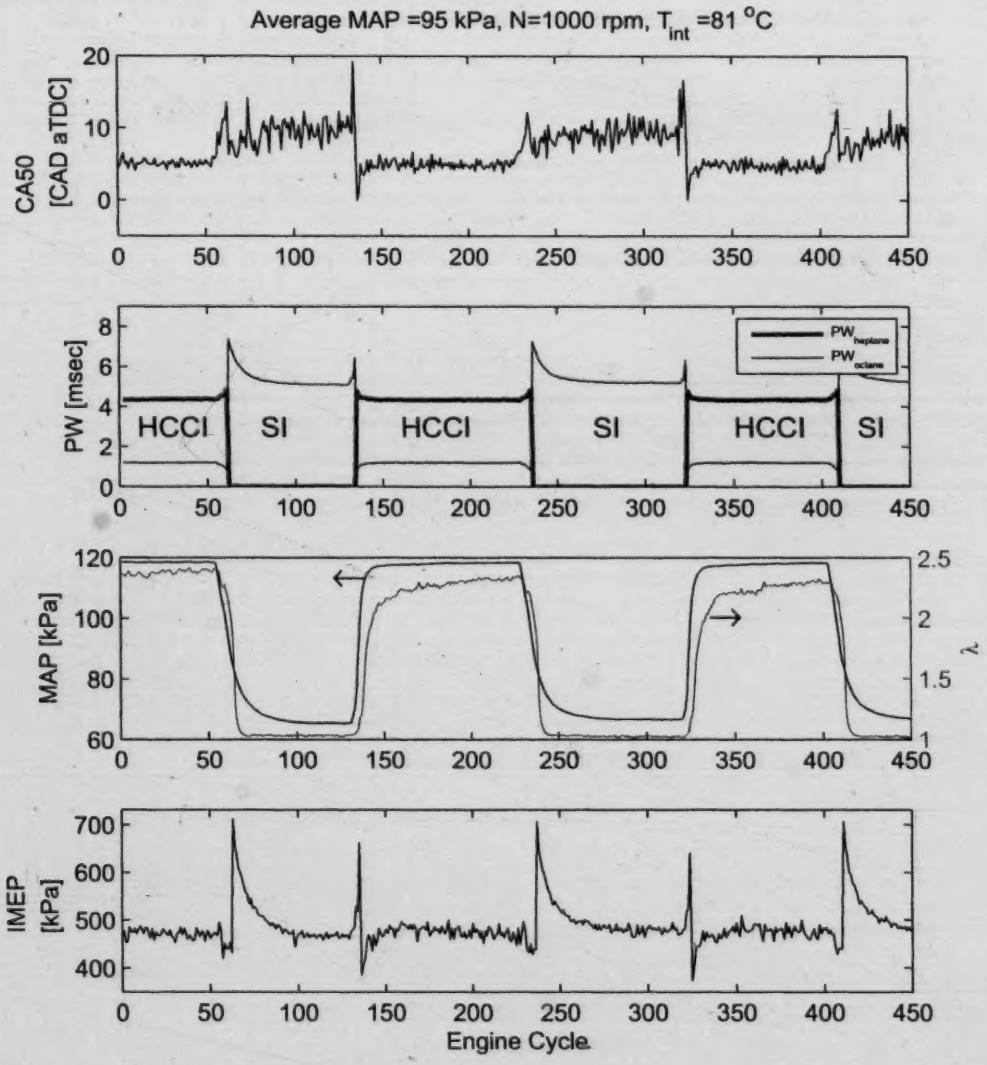

Figure 5.55: HCCI-SI Mode Switch with Similar Steady State Loads, HCCI MAP 120kPa. Test MS4.

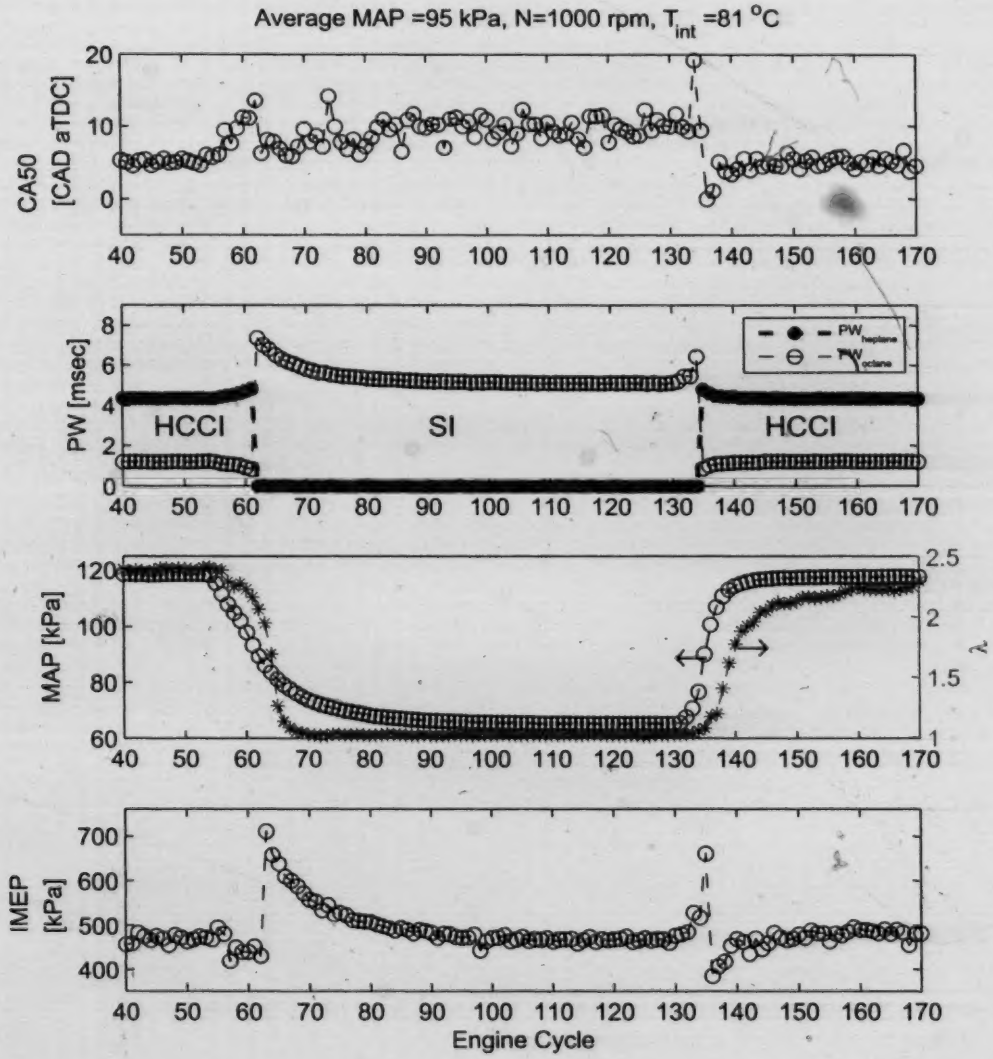

Figure 5.56: Close Up of HCCI-SI Mode Switch with Similar Steady State Loads, HCCI MAP 120kPa. Test MS4.

Chapter 6

Conclusion

In this chapter the main conclusions from this work are presented and put into context for an automotive application. Future work is also outlined.

6.1 Conclusions

In this work a single cylinder engine with properties typical of a modern spark ignition engine has been used to examine HCCI combustion experimentally. A range of intake manifold pressures, intake manifold temperatures and engine speeds have been investigated. Mechanical supercharging is used to increase the intake manifold pressure above atmospheric and electrical heating is used to increase the intake manifold temperature. The increased manifold pressure and temperature are used to expand the range of HCCI. Load control on this engine is performed by using two separate port fuel injection systems to supply n-heptane and iso-octane to the engine independently. The main results of this work are summarized below.

- Combustion timing which maximizes IMEP retards as engine speed increases. For 800rpm, 5 CAD aTDC was found to be optimum, at 1000rpm, 7 CAD aTDC was optimum, and at 1200rpm, 9 CAD aTDC was optimum.
- The range of IMEP expands with increases in MAP. The low load limit reduces

with increasing T_{int} and low MAP. The maximum IMEP increases with MAP at a constant engine speed of 1000rpm, as: 500kPa at a MAP of 110kPa, to an IMEP of 550kPa at a MAP of 125kPa, up to a maximum of 600kPa at a MAP of 140kPa.

- Lower ON is required at low values of MAP and higher engine speed. As MAP is increased the increased oxygen content advances the combustion timing for a given amount of n-heptane. Increasing engine sped reduces the time available for combustion, and therefore a mixture which has a lower induction time for auto-ignition is required.

- The heat released during the LTR region of combustion was within a relatively narrow range for all cases tested. HR_{LTR} values of 20-50J combustion were found for all tests. The mass of n-heptane injected in the cylinder has the most direct effect on this LTR region for a given operating condition. Changes in the MAP and engine speed alter the mass of n-heptane required for the HR_{LTR} to be within the viable range.

- Only small changes to the n-heptane mass injected are required to achieve the entire load range at a given operating condition. Changes to engine load can be made by varying the quantity of iso-octane injected, while using the n-heptane to set combustion timing.

- Carbon monoxide and unburned hydrocarbon emissions were found to be most strongly influenced by changes in λ . Larger values of λ result in increased CO and UHC due to the lower combustion temperatures. Conversely NO_x emissions remain exceptionally low for almost the entire range of λ , except as the high load limit is approached. At $\lambda = 2$, NO_x emissions sharply increase as combustion temperatures enter the range where thermal NO_x is formed.

- The BSFC in HCCI mode remains lower than that for the same engine in SI mode at the same load.

- The occurrence of HCCI knock increases as combustion event length decreases. Knock intensity measured with an engine structure mounted accelerometer is related to the value of $\frac{\Delta P}{\Delta \theta}$, but the amplitude appears to be sensitive to engine speed. Estimates of the knocking frequency correlate with cylindrical modes of oscillation combined with an estimated in-cylinder temperature. However the estimation of the in-cylinder temperature from the knocking frequency loses sensitivity for slow combustion events, as signal to noise deteriorates.

- Load transients of both pulse and step types result in deviations in the combustion timing during the transient. For increases in load, the combustion timing retards through the transient, and for decreases in load the combustion timing advances. Fuel wall wetting on the intake port surfaces appears to be negligible. The transient appears to affect the LTR region of combustion significantly, which is the presumed cause of the combustion timing variations.

- Using the dual fuel actuation strategy, SI-HCCI mode transitions are performed using open loop techniques. During the mode transition, no knocking or misfiring cycles were noticed. Switching modes at constant load is hindered by a long transient in MAP; however this is an artifact of the experimental setup.

- Two fuels provide a simple and effective actuation method for implementing mode transition between SI and HCCI modes of combustion. The use of two fuels does, however, add to the engine complexity due to the requirement for an additional fuel system.

By uncoupling the effects of fueling into two separate fuels, one of which can be used to control combustion timing (n-heptane), and one that can be used to achieve

the desired load (iso-octane), a simplified control strategy for engine management may be possible.

6.2 Future Work

To make HCCI practical for use on production automobile engines, means of expanding the load-speed operating range are needed to allow the benefits of HCCI to be maintained over the largest range of operation. For the current experimental setup two significant additional actuation parameters can be investigated. By adding a throttled line from the exhaust system to the intake plenum external EGR can be metered into the engine. [Atkins, 2004] shows that EGR is more effective at controlling the combustion than ON in steady state operation. To understand the effects of using EGR during transients, a fast response measurement of EGR would be required.

The other possible actuation mechanism is varying the fuel injection timing. By altering the phasing of the fuel injection pulse (or possibly the pulse for each fuel) relative to the engine cycle, the air-fuel mixture preparation is altered. In this work the fuel is injected on the closed intake valves. By injecting fuel during the intake stroke, the fuel has less time to evaporate during the cycle, but is injected into the high velocity air stream as it enters the engine. Changing the timing of the injection, the stratification of air and fuel inside the cylinder can be adjusted. An injection timing resulting in a relatively homogenous charge may be useful in maximizing high load operation, as the inhomogeneities responsible for knock are reduced. Conversely an injection timing resulting in a relatively stratified charge may extend low load limits by providing a locally richer region for the combustion to initiate.

To further investigate the possibilities of HCCI new methods of controlling engine parameters are required. This thesis does not examine the effect of actively changing the amount of residual gas. This has a significant influence on HCCI combustion that

can be realized with variable valve timing. By actively varying the valve timing the amount of residual gas held in the cylinder can be controlled. This actuation strategy has effects similar to that of EGR, but can be potentially controlled from cycle to cycle, whereas external EGR generally suffers from a relatively slow response time.

BIBLIOGRAPHY

[Aceves et al., 2002] Aceves, S. M., Flowers, D. L., Espinosa-Loza, F., Martinez-Frias, J., Dibble, R. W., Christensen, M., Johansson, B., and Hessel, R. P. (2002). Piston-liner crevice geometry effect on HCCI combustion by multi-zone analysis. *Society of Automotive Engineers, Paper No. 2002-01-2869.*

[Aceves et al., 2005] Aceves, S. M., Flowers, D. L., Martinez-Frias, J., Espinosa-Loza, F., Christensen, M., Johansson, B., and Hessel, R. P. (2005). Analysis of the effect of geometry generated turbulence on HCCI combustion by multi-zone modeling. *Society of Automotive Engineers, Paper No. 2005-01-2134.*

[Aceves et al., 2001] Aceves, S. M., Flowers, D. L., Martinez-Frias, J., Smith, J. R., Dibble, Au, M., and Girard, J. (2001). HCCI combustion: analysis and experiments. *Society of Automotive Engineers, Paper No. 2001-01-2077.*

[A&D Technologies, 2001a] A&D Technologies (2001a). *ADAPT 4.6 User Manual.*

[A&D Technologies, 2001b] A&D Technologies (2001b). *BaseLine CAS Manual.*

[Andreae et al., 2007] Andreae, M. M., Cheng, W. K., Kenney, T., and Yang, J. (2007). On HCCI engine knock. *Society of Automotive Engineers, Paper No. 2007-01-1858.*

[Atkins, 2004] Atkins, M. (2004). Experimental examination of the effects of fuel octane and diluent on HCCI combustion. M.Sc. thesis, University of Alberta.

[Atkins and Koch, 2005] Atkins, M. J. and Koch, C. R. (2005). The effect of fuel octane and diluent on HCCI combustion. *Proc. IMechE, Part D*, 219:665 – 675.

[Babajimopoulos et al., 2003] Babajimopoulos, A., Lavoie, G. A., and Assanis, D. N. (2003). Modeling HCCI combustion with high levels of residual gas fraction a comparison of two VVA strategies. *Society of Automotive Engineers, Paper No. 2003-01-3220.*

[Bengtsson, 2004] Bengtsson, J. (2004). *Closed-Loop Control of HCCI Engine Dynamics.* PhD thesis, Lund Institute of Technology.

[Berntsson and Denbratt, 2007] Berntsson, A. W. and Denbratt, I. (2007). HCCI combustion using charge stratification for combustion control. *Society of Automotive Engineers, Paper No. 2007-01-0210.*

[Bhave et al., 2005] Bhave, A. N., Kraft, M., Mauss, F., Oakley, A. J., and Zhao, H. (2005). Evaluating the EGR-AFR operating range of a HCCI engine. *Society of Automotive Engineers, Paper No. 2005-01-0161.*

[Blair, 1999] Blair, G. P. (1999). *Design and Simulation of Four-Stroke Engines.* Society of Automotive Engineers.

[Cairns and Blaxill, 2007] Cairns, A. and Blaxill, H. (2007). The effects of two-stage cam profile switching and external EGR on SI-CAI combustion transitions. *Society of Automotive Engineers, Paper No. 2007-01-0187.*

[Chang, 1993] Chang, C.-F. (1993). *Air-fuel ratio control in an IC engine using an event-based observer.* PhD thesis, Stanford University.

[Chang et al., 2004] Chang, J., Gralp, O., Filipi, Z., Assanis, D., Kuo, T.-W., Najt, P., and Rask, R. (2004). New heat transfer correlation for an HCCI engine de-

rived from measurements of instantaneous surface heat flux. *Society of Automotive Engineers, Paper No. 2004-01-2996.*

[Chang et al., 2005] Chang, J., Z Filipi, D. A., T-W Kuo, P. N., and Rask, R. (2005). Characterizing the thermal sensitivity of a gasoline homogeneous charge compression ignition engine with measurements of instantaneous wall temperature and heat flux. *International Journal of Engine Research*, 6:289–309.

[Chang et al., 2006] Chang, K., Babajimopoulos, A., Lavoie, G. A., Filipi, Z. S., and Assanis, D. N. (2006). Analysis of load and speed transitions in an HCCI engine using 1-D cycle simulation and thermal networks. *Society of Automotive Engineers, Paper No. 2006-01-1087.*

[Christensen et al., 1999] Christensen, M., Hultqvist, A., and Johansson, B. (1999). Demonstrating the multi fuel capability of a homogeneous charge compression ignition engine with variable compression ratio. *Society of Automotive Engineers, Paper No. 1999-01-3679.*

[Dec and Sjoberg, 2003] Dec, J. E. and Sjoberg, M. (2003). A parametric study of HCCI combustion–the sources of emissions at low loads and the effects of GDI fuel injection. *Society of Automotive Engineers, Paper No. 2003-01-0752.*

[Draper, 1935] Draper, C. S. (1935). The physical effects of detonation in a closed cylindrical chamber. Technical Report 493, National Advisory Committee for Aeronautics.

[dSPACE, 2005] dSPACE (2005). *MicroAutoBox Hardware Installation and Configuration.*

[Fekete, 1995] Fekete, N. (1995). *Model-Based Air-Fuel Ratio Control of a Multi-Cylinder Leanburn Engine.* PhD thesis, Stanford University.

[Haraldsson et al., 2004] Haraldsson, G., Hyvonen, J., Tunestal, P., and Johansson, B. (2004). HCCI closed-loop combustion control using fast thermal management. *Society of Automotive Engineers, Paper No. 2004-01-0943.*

[Heywood, 1988] Heywood, J. B. (1988). *Internal combustion engine fundamentals.* McGraw-Hill, New York.

[Hitachi North America, 2003] Hitachi North America (2003). Personal communication.

[Hyvonen et al., 2003] Hyvonen, J., Haraldsson, G., and Johansson, B. (2003). Supercharging HCCI to extend the operating range in a multi- cylinder VCR-HCCI engine. *Society of Automotive Engineers, Paper No. 2003-01-3214.*

[Hyvonen et al., 2006] Hyvonen, J., Wilhelmsson, C., and Johansson, B. (2006). The effect of displacement on air-diluted multi-cylinder HCCI engine performance. *Society of Automotive Engineers, Paper No. 2006-01-0205.*

[Incropera and DeWitt, 2002] Incropera, F. P. and DeWitt, P. (2002). *Introduction to Heat Transfer.* John Wiley and Sons Inc.

[Iverson et al., 2005] Iverson, R. J., Herold, R. E., Augusta, R., Foster, D. E., Ghandhi, J. B., Eng, J. A., and Najt, P. M. (2005). The effects of intake charge preheating in a gasoline-fueled HCCI engine. *Society of Automotive Engineers, Paper No. 2005-01-3742.*

[Kirchen et al., 2007] Kirchen, P., M.Shahbahkti, and Koch, C. (2007). A skeletal kinetic mechanism for PRF combustion in HCCI engines. *Combustion Science and Technology,* 179:1059–1083.

[Kongsereeparp and Checkel, 2007] Kongsereeparp, P. and Checkel, M. D. (2007). Novel method of setting initial conditions for multi-zone HCCI combustion modeling. *Society of Automotive Engineers, Paper No. 2007-01-0647.*

[Kulzer et al., 2007] Kulzer, A., Hathout, J.-P., Sauer, C., Karrelmeyer, R., Fischer, W., and Christ, A. (2007). Multi-mode combustion strategies with CAI for a GDI engine. *Society of Automotive Engineers, Paper No. 2007-01-0214.*

[MacLean and Lave, 2003] MacLean, H. L. and Lave, L. B. (2003). Evaluating automobile fuel/propulsion system technologies. *Progress in Energy and Combustion Science*, 29:1–69.

[Maloney, 1999] Maloney, P. J. (1999). An event-based transient fuel compensator with physically based parameters. *Society of Automotive Engineers, Paper No. 1999-01-0553.*

[Martinez-Frias et al., 2000] Martinez-Frias, J., Aceves, S. M., Flowers, D., Smith, J. R., and Dibble, R. (2000). HCCI engine control by thermal management. *Society of Automotive Engineers, Paper No. 2000-01-2869.*

[Milovanovic et al., 2005a] Milovanovic, N., Blundell, D., Gedge, S., and Turner, J. (2005a). SI-HCCI-SI mode transition at different engine operating conditions. *Society of Automotive Engineers, Paper No. 2005-01-0156.*

[Milovanovic et al., 2005b] Milovanovic, N., Turner, J. W. G., Kenchington, S. A., Pitcher, G., and Blundell, D. W. (2005b). Active valvetrain for homogeneous charge compression ignition. *International Journal of Engine Research*, 6:377–397.

[Moffat, 1988] Moffat, R. J. (1988). Describing the uncertainties in experimental results. *Experimental Thermal and Fluid Science*, 1:3–17.

[Najt and Foster, 1983] Najt, P. M. and Foster, D. E. (1983). Compression-ignited homogeneous charge combustion. *Society of Automotive Engineers, Paper No. 830264.*

[Oakley et al., 2001] Oakley, A., hua Zhao, Ladommatos, N., and Ma, T. (2001). Dillution effects on the controlled auto-ignition (CAI) combustion of hydrocarbon and alcohol fuels. *Society of Automotive Engineers, Paper No. 2001-01-3606.*

[Olsson et al., 2004] Olsson, J.-O., Tunestal, P., and Johansson, B. (2004). Boosting for high load HCCI. *Society of Automotive Engineers, Paper No. 2004-01-0940.* Collection.

[Olsson et al., 2001] Olsson, J.-O., Tunestl, P., and Johansson, B. (2001). Closed-loop control of an HCCI engine. *Society of Automotive Engineers, Paper No. 2001-01-1031.*

[Owen and Coley, 1990] Owen, K. and Coley, T. (1990). *Automotive Fuels Handbook.* Society of Automotive Engineers.

[Payri et al., 2006] Payri, F., Molina, S., Martin, J., and Armas, O. (2006). Influence of measurement errors and estimated parameters on combustion diagnosis. *Applied Thermal Engineering*, 26:226236.

[Press et al., 1992] Press, W., Teukolsky, S., Vetterling, W., and Flannery, B. (1992). *Numerical Recipes in C.* Cambridge University Press, Cambridge, UK, 2nd edition.

[Scholl et al., 1998] Scholl, D. J., Davis, C., Russ, S. G., and Barash, T. (1998). The volume acoustic modes of spark-ignited internal combustion chambers. *Society of Automotive Engineers, Paper No. 980893.*

[Shahbakhti et al., 2007a] Shahbakhti, M., Lupul, R., Audet, A., and Koch, C. R. (2007a). Experimental study of HCCI cyclic variations for low-octane PRF fuel

blends. In *The Combustion Institute Canadaian Section 2007 Spring Technical Meeting*, Banff, Alberta, Canada.

[Shahbakhti et al., 2007b] Shahbakhti, M., Lupul, R., and Koch, C. R. (2007b). Cyclic variations of ignition timing in an HCCI engine. pages 405 – 415, Pueblo, CO, United States.

[Shahbakhti et al., 2007c] Shahbakhti, M., Lupul, R., and Koch, C. R. (2007c). Predicting HCCI auto-ignition timing by extending a modified knock-integral method.

[Sjoberg and Dec, 2003] Sjoberg, M. and Dec, J. E. (2003). Combined effects of fuel-type and engine speed on intake temperature requirements and completeness of bulk-gas reactions for HCCI combustion. *Society of Automotive Engineers, Paper No. 2003-01-3173.*

[Sjoberg and Dec, 2007] Sjoberg, M. and Dec, J. E. (2007). EGR and intake boost for managing HCCI low-temperature heat release over wide ranges of engine speed. *Society of Automotive Engineers, Paper No. 2007-01-0051.*

[Sjoberg et al., 2004] Sjoberg, M., Dec, J. E., Babajimopoulos, A., and Assanis, D. (2004). Comparing enhanced natural thermal stratification against retarded combustion phasing for smoothing of HCCI heat-release rates. *Society of Automotive Engineers, Paper No. 2004-01-2994.*

[Sjoberg et al., 2005] Sjoberg, M., Dec, J. E., and Cernansky, N. P. (2005). Potential of thermal stratification and combustion retard for reducing pressure-rise rates in HCCI engines, based on multi-zone modeling and experiments. *Society of Automotive Engineers, Paper No. 2005-01-0113.*

[Sjoberg et al., 2007] Sjoberg, M., Dec, J. E., and Hwang, W. (2007). Thermodynamic and chemical effects of EGR and its constituents on HCCI autoignition. *Society of Automotive Engineers, Paper No. 2007-01-0207.*

[Stanglmaier and Roberts, 1999] Stanglmaier, R. H. and Roberts, C. E. (1999). Homogeneous charge compression ignition (HCCI): Benefits, compromises, and future engine applications. *Society of Automotive Engineers, Paper No. 1999-01-3682.*

[Stone et al., 2000] Stone, C. R., Lim, E. P., Ewart, P., Lloyd, G., and Williams, R. B. (2000). Temperature and heat flux measurements in a spark-ignition engine. *Society of Automotive Engineers, Paper No. 2000-01-1214.*

[Stone, 1999] Stone, R. (1999). *Introduction to Internal Combustion Engines.* Society of Automotive Engineers.

[Tanaka et al., 2003a] Tanaka, S., Ayala, F., , and Keck, J. C. (2003a). A reduced chemical kinetic model for HCCI combustion of primary reference fuels in a rapid compression machine. *Combustion and flame*, 133:467–481.

[Tanaka et al., 2003b] Tanaka, S., Ayala, F., Keck, J. C., and Heywood, J. B. (2003b). Two-stage ignition in HCCI combustion and HCCI control by fuels and additives. *Combustion and Flame*, 132:219–239.

[Tsurushima et al., 2002] Tsurushima, T., Asaumi, Y., and Aoyagi, Y. (2002). The effect of knock on heat loss in homogeneous charge compression ignition engines. *Society of Automotive Engineers, Paper No. 2002-01-0108.*

[Turns, 2000] Turns, S. R. (2000). *An Introduction to Combustion.* McGraw-Hill.

[Wilhelmsson et al., 2005] Wilhelmsson, C., Vressner, A., Tunestal, P., Johansson, B., Sarner, G., and Alden, M. (2005). Combustion chamber wall temperature mea-

surement and modeling during transient HCCI operation. *Society of Automotive Engineers, Paper No. 2005-01-3731.*

[Xu et al., 2004] Xu, H., Rudolph, S., Liu, Z., Wallace, S., Richardson, S., Wyszynski, M., and Megaritis, A. (2004). An investigation into the operating mode transitions of a homogeneous charge compression ignition engine using EGR trapping. *Society of Automotive Engineers, Paper No. 2004-01-1911.*

[Xu et al., 2007] Xu, H. M., Wyszynski, M. L., Megaritis, A., Yap, D., Wilson, T., Qiao, J., Richardson, S., Golunski, S., and Peucheret, S. (2007). Research on expansion of operating windows of controlled homogeneous auto-ignition engines. *International Journal of Engine Research*, 8:29–40.

[Yap et al., 2005a] Yap, D., Megaritis, A., Wyszynski, M., and Xu, H. (2005a). Effect of inlet valve timing on boosted gasoline HCCI with residual gas trapping. *Society of Automotive Engineers, Paper No. 2005-01-2136.*

[Yap et al., 2005b] Yap, D., Wyszynski, M., Megaritis, A., and Xu, H. (2005b). Applying boosting to gasoline HCCI operation with residual gas trapping. *Society of Automotive Engineers, Paper No. 2005-01-2121.*

[Yelvington and Green, 2003] Yelvington, P. E. and Green, W. H. (2003). Prediction of the knock limit and viable operating range for a homogeneous-charge compression-ignition (HCCI) engine. *Society of Automotive Engineers, Paper No. 2003-01-1092.*

Appendix A

Experimental Data Summary

A.1 HCCI Combustion Timing Test Data

Test No.	Speed [rpm]	MAP [kPa]	T_{int} [°C]	λ	$\overline{IMEP}$ [kPa]	$\overline{CA5_{HTR}}$ [CAD ATDC]	$\overline{P_{rise}}$ [bar/CAD]	BSFC [g/kWhr]	BSCO [g/kWhr]	BSUHC [g/kWhr]	BSNOx [g/kWhr]
CT 6	800	125.3	86.1	2.45	483	9.2	1.0	280	22.2	35.4	0.014
CT 7	800	125.6	88.9	2.44	492	8.4	1.5	281	19.3	33.3	0.014
CT 8	800	125.2	94.3	2.40	506	6.4	2.8	265	14.4	28.4	0.013
CT 9	800	125.5	101.9	2.38	504	4.7	4.0	265	11.8	24.8	0.013
CT10	800	125.9	107.0	2.35	505	3.4	5.5	261	10.2	22.8	0.013
CT11	800	125.0	111.4	2.30	501	3.0	6.2	262	9.3	22.2	0.016
CT12	800	125.2	117.3	2.27	494	2.2	7.5	272	8.5	21.9	0.021
CT13	1000	125.2	93.6	2.25	498	9.5	1.5	254	-0.2	0.0	0.008
CT14	1000	125.5	96.1	2.24	513	7.7	2.5	244	11.7	23.9	0.012
CT15	1000	125.1	100.6	2.22	515	6.7	3.3	243	10.2	22.0	0.012
CT16	1000	125.3	105.5	2.20	507	6.1	3.8	249	9.4	21.5	0.015
CT17	1000	125.6	109.6	2.19	505	4.8	4.9	249	8.1	18.6	0.019
CT18	1000	125.8	112.9	2.16	501	4.0	6.2	254	7.5	17.9	0.021
CT19	1200	125.3	100.2	2.05	507	10.8	1.4	258	11.4	26.1	0.012
CT20	1200	125.7	102.0	2.04	517	9.6	2.1	252	9.4	22.4	0.018
CT21	1200	126.4	106.5	2.03	517	8.0	3.2	253	7.8	18.6	0.024
CT22	1200	125.5	110.6	2.00	507	6.9	4.1	259	7.3	17.7	0.029

A.2 HCCI Steady State Data

Test No.	Speed [rpm]	MAP [kPa]	T_{int} [°C]	λ	$\overline{IMEP}$ [kPa]	$\overline{CA5_{HTR}}$ [CAD ATDC]	$\overline{P_{rise}}$ [bar/CAD]	BSFC [g/kWhr]	BSCO [g/kWhr]	BSUHC [g/kWhr]	BSNOx [g/kWhr]
SS1	1000	109.4	64.0	2.07	486	6.3	3.6	272	8.7	20.4	0.014
SS2	1000	109.5	64.6	1.90	515	6.6	4.8	266	6.4	18.5	0.063
SS3	1000	109.5	65.1	1.91	514	6.5	4.8	269	6.5	18.6	0.058
SS4	1000	109.5	69.8	2.15	467	6.1	3.3	271	10.1	21.5	0.011
SS5	1000	109.6	70.0	1.94	503	6.5	4.5	263	6.9	19.0	0.031
SS6	1000	109.6	70.5	1.93	504	6.4	4.6	269	6.6	18.4	0.057
SS7	1000	109.6	79.6	2.31	429	6.1	2.3	277	14.1	23.2	0.011
SS8	1000	109.7	79.7	2.02	482	6.3	4.0	264	8.0	20.1	0.015
SS9	1000	109.8	80.5	1.91	494	6.2	5.0	264	6.7	18.7	0.054
SS10	1000	109.8	89.9	2.48	392	5.9	1.6	290	21.0	25.8	0.012
SS11	1000	109.4	90.6	2.13	451	6.4	3.1	267	10.1	22.0	0.016
SS12	1000	109.5	91.3	1.90	489	6.9	4.4	264	6.4	18.3	0.141
SS13	1000	109.6	100.6	2.65	354	6.0	1.0	308	32.3	29.5	0.017
SS14	1000	109.7	100.5	2.23	426	6.3	2.5	269	12.7	24.0	0.010
SS15	1000	109.9	101.1	1.92	474	6.5	4.5	268	6.6	19.0	0.089
SS16	1000	124.7	89.9	2.79	416	5.8	1.0	268	42.7	28.6	0.022
SS17	1000	124.7	90.2	2.50	479	5.7	2.3	250	18.2	23.6	0.017
SS18	1000	124.2	91.2	2.12	550	6.8	3.8	245	8.1	19.5	0.020
SS19	1000	124.7	98.6	2.95	383	5.3	0.7	289	63.7	32.0	0.023
SS20	1000	124.2	98.9	2.49	471	5.6	2.3	246	16.8	23.3	0.017
SS21	1000	124.4	98.5	2.06	554	7.0	4.2	244	7.2	18.9	0.023
SS22	1000	124.4	108.8	3.16	317	5.7	0.1	359	130.5	44.9	0.025
SS23	1000	124.4	109.7	2.55	449	6.3	1.8	256	18.4	24.0	0.014
SS24	1000	124.6	109.8	2.02	552	6.3	5.2	246	6.6	18.4	0.050
SS25	1000	124.6	120.3	3.21	322	5.1	0.3	344	138.1	46.7	0.025

continued on next page

Test No.	Speed [rpm]	MAP [kPa]	T_{int} [°C]	λ	$\overline{IMEP}$ [kPa]	$\overline{CA5_{HTR}}$ [CAD ATDC]	$\overline{P_{rise}}$ [bar/CAD]	BSFC [g/kWhr]	BSCO [g/kWhr]	BSUHC [g/kWhr]	BSNOx [g/kWhr]
SS26	1000	124.7	120.1	2.56	447	5.6	2.1	255	18.7	25.0	0.018
SS27	1000	124.4	119.7	1.97	541	6.1	6.0	255	6.2	18.3	0.193
SS28	1000	124.4	128.6	3.17	326	5.2	0.4	315	90.5	40.4	0.027
SS29	1000	124.5	129.0	2.33	473	6.5	2.8	251	11.5	22.5	0.017
SS30	1000	124.7	130.6	2.00	536	7.7	4.3	253	6.5	18.5	0.165
SS31	1000	140.3	99.4	3.07	411	5.4	0.6	295	94.4	45.3	0.002
SS32	1000	140.3	98.9	2.70	491	5.9	1.6	252	25.0	25.4	0.004
SS[illegible]	1000	140.5	100.3	2.19	605	6.5	4.5	237	8.7	20.2	0.004
SS34	1000	140.8	109.4	3.22	370	5.1	0.3	317	151.2	44.9	0.003
SS35	1000	140.3	110.4	2.46	527	5.9	2.9	247	14.7	24.1	0.004
SS36	1000	140.4	109.9	2.14	597	6.5	4.7	242	8.4	22.2	0.006
SS37	1000	140.4	120.6	2.56	353	5.7	0.2	340	32.3	45.2	0.012
SS38	1000	140.4	120.6	2.56	504	5.8	2.5	246	17.9	25.0	0.007
SS39	1000	140.6	119.8	2.10	592	6.6	5.0	246	7.6	22.2	0.009
SS40	1000	141.2	130.3	3.32	342	5.1	0.3	326	135.6	46.5	0.015
SS41	1000	141.3	130.4	2.60	484	6.3	2.1	254	23.3	27.1	0.012
SS42	1000	140.8	130.1	2.11	584	7.2	4.6	252	7.2	22.4	0.020
SS43	1000	140.4	139.3	3.32	338	5.3	0.3	330	107.5	43.1	0.015
SS44	1000	139.8	139.3	2.50	498	5.8	2.8	252	14.1	24.5	0.006
SS45	1000	140.1	140.7	2.05	576	6.5	5.6	254	6.7	21.1	0.110
SS46	800	125.3	72.6	3.21	372	4.2	0.6	336	103.9	39.9	0.021
SS47	800	125.0	75.5	2.62	487	4.3	3.0	267	20.7	27.1	0.015
SS48	800	125.3	77.6	2.26	554	4.3	5.7	258	11.2	24.8	0.019
SS49	800	125.4	89.3	3.31	339	4.0	0.5	338	99.6	37.7	0.024
SS50	800	125.4	88.5	2.69	457	4.2	2.7	269	22.4	27.3	0.017

continued on next page

Test No.	Speed [rpm]	MAP [kPa]	T_{int} [°C]	λ	$\overline{IMEP}$ [kPa]	$\overline{CA5_{HTR}}$ [CAD ATDC]	$\overline{P_{rise}}$ [bar/CAD]	BSFC [g/kWhr]	BSCO [g/kWhr]	BSUHC [g/kWhr]	BSNOx [g/kWhr]
SS51	800	125.1	89.0	2.27	532	4.2	5.5	261	11.3	23.8	0.013
SS52	800	125.2	99.3	3.52	275	4.2	0.1	459	327.9	67.7	0.029
SS53	800	125.3	99.7	2.69	451	3.1	3.4	263	21.1	27.3	0.012
SS54	800	125.4	100.4	2.28	520	3.5	6.4	263	10.6	24.1	0.010
SS55	800	125.1	108.6	3.46	307	3.7	0.4	367	136.3	45.1	0.033
SS56	800	125.2	109.7	2.70	441	3.1	3.4	267	22.6	27.4	0.019
SS57	800	125.3	110.6	2.28	508	3.7	6.1	267	10.7	24.8	0.018
SS58	800	125.1	120.4	3.51	305	3.0	0.7	344	96.5	38.8	0.026
SS59	800	124.9	119.8	2.81	408	4.1	2.2	279	26.6	29.4	0.012
SS60	800	125.2	120.6	2.23	501	3.8	6.5	274	9.8	25.3	0.018
SS61	1200	124.9	92.3	2.50	437	7.2	1.3	275	23.3	25.1	0.018
SS62	1200	124.8	91.8	2.20	496	7.9	2.3	254	11.9	21.7	0.015
SS63	1200	124.9	91.7	1.93	551	8.5	3.6	246	7.5	18.3	0.039
SS64	1200	125.6	99.3	2.65	404	7.0	0.9	283	33.6	27.8	0.019
SS65	1200	125.6	99.1	2.38	457	7.8	1.5	267	17.0	23.8	0.017
SS66	1200	125.8	99.0	1.95	543	8.1	3.9	248	7.1	18.1	0.041
SS67	1200	125.2	109.0	2.48	427	7.5	1.3	280	20.7	26.7	0.019
SS68	1200	125.6	109.1	2.22	481	7.9	2.2	257	11.8	23.4	0.017
SS69	1200	126.0	110.4	1.95	531	7.8	4.0	253	7.1	19.4	0.043
SS70	1200	125.6	120.4	2.64	391	7.3	0.9	297	31.1	31.5	0.021
SS71	1200	125.1	121.2	2.27	458	8.3	1.8	262	13.8	25.8	0.017
SS72	1200	125.2	120.3	1.88	531	8.3	4.2	253	6.7	19.4	0.124
SS73	1200	125.8	128.2	2.79	356	7.3	0.5	329	44.3	36.0	0.028
SS74	1200	126.0	127.8	2.29	452	8.6	1.6	266	14.1	27.0	0.018
SS75	1200	126.0	127.8	2.29	530	8.7	4.2	316	14.2	27.1	0.018

A.3 HCCI Repeated Trials Data

Test No.	Speed [rpm]	MAP [kPa]	T_{int} [°C]	λ	$\overline{IMEP}$ [kPa]	$\overline{CA5_{HTR}}$ [CAD ATDC]	$\overline{P_{rise}}$ [bar/CAD]	BSFC [g/kWhr]	BSCO [g/kWhr]	BSUHC [g/kWhr]	BSNOx [g/kWhr]
RT 1	800	125.4	121.2	3.51	287	3.6	0.3	441	209.5	57.8	0.027
RT 2	800	125.2	122.1	2.77	424	3.8	2.4	289	19.9	23.2	0.011
RT 3	800	124.9	122.4	2.21	528	4.4	5.8	271	6.8	16.0	0.012
RT 4	1000	124.7	112.0	3.18	343	3.7	0.7	334	56.8	25.7	0.020
RT 5	1000	124.6	111.2	2.50	465	5.2	2.6	256	13.4	17.3	0.013
RT 6	1000	124.7	110.4	1.99	569	6.2	5.9	247	6.7	13.3	0.079
RT 7	1200	124.9	94.1	2.64	428	6.6	1.2	284	23.9	19.2	0.016
RT 8	1200	124.9	94.7	2.48	462	6.7	1.8	284	20.3	17.6	0.015
RT 9	1200	125.0	95.2	2.07	553	7.9	3.5	251	8.3	13.4	0.014
RT10	1000	109.8	100.8	2.71	360	4.7	1.5	299	22.4	20.8	0.016
RT11	1000	109.9	100.5	2.53	391	5.0	2.0	354	19.8	19.8	0.015
RT12	1000	110.0	99.7	2.02	489	6.3	4.5	262	5.9	13.3	0.019
RT13	1000	140.1	141.5	3.45	330	4.3	0.3	337	134.0	46.7	0.025
RT14	1000	140.2	142.2	2.60	496	5.4	2.7	250	14.0	26.8	0.013
RT15	1000	140.1	141.5	2.12	550	6.8	4.3	242	7.8	24.5	0.011
RT16	800	124.9	120.6	3.21	363	2.7	1.3	317	34.4	14.4	0.028
RT17	800	124.8	119.9	2.62	460	3.6	3.2	273	16.5	10.4	0.020
RT18	800	125.2	120.2	2.10	551	3.3	8.5	270	4.6	7.0	0.078
RT19	1000	124.5	108.2	2.91	387	4.1	1.3	276	14.2	7.3	0.023
RT20	1000	124.4	106.7	2.33	508	4.4	4.3	238	5.4	5.4	0.016
RT21	1000	124.5	106.2	1.95	584	6.3	6.5	242	2.5	4.0	0.174
RT22	1200	124.9	89.2	2.57	457	6.2	1.6	271	11.8	6.7	0.020
RT23	1200	125.2	89.8	2.26	525	6.6	3.0	250	5.9	5.1	0.016
RT24	1200	124.9	90.4	2.08	582	6.1	7.0	262	2.4	3.6	0.136
RT25	1000	109.7	97.8	2.57	395	3.5	2.6	282	9.1	6.3	0.019

continued on next page

Test No.	Speed [rpm]	MAP [kPa]	T_{int} [°C]	λ	$\overline{IMEP}$ [kPa]	$\overline{CA5_{HTR}}$ [CAD ATDC]	$\overline{P_{rise}}$ [bar/CAD]	BSFC [g/kWhr]	BSCO [g/kWhr]	BSUHC [g/kWhr]	BSNOx [g/kWhr]
RT26	1000	109.6	96.1	2.21	459	4.4	4.4	300	4.8	5.0	0.016
RT27	1000	109.6	94.7	1.91	523	6.8	5.1	248	3.1	4.3	0.063
RT28	1000	139.5	139.9	3.20	388	3.5	1.2	267	22.3	9.6	0.024
RT29	1000	139.2	139.3	2.46	523	4.7	3.8	237	7.3	9.9	0.016
RT30	1000	139.2	139.7	2.06	605	5.8	6.7	243	4.0	13.9	0.047
RT31	800	124.8	120.5	3.38	322	3.5	0.5	351	70.9	21.1	0.036
RT32	800	124.9	120.5	2.75	432	4.4	2.1	281	15.9	12.2	0.022
RT33	800	125.0	119.4	2.20	542	5.0	5.3	264	6.1	8.5	0.020
RT34	1000	124.7	108.4	2.93	400	3.4	1.7	267	17.2	9.1	0.022
RT35	1000	124.8	108.8	2.43	489	4.5	3.6	240	6.6	6.5	0.017
RT36	1000	124.9	109.1	2.00	573	5.9	6.2	241	3.0	4.9	0.097
RT37	1200	125.3	90.9	2.62	445	6.5	1.3	281	13.9	7.4	0.021
RT38	1200	125.5	91.5	2.31	516	6.7	2.7	254	6.2	5.4	0.017
RT39	1200	125.6	91.8	2.01	581	7.5	4.4	239	3.8	4.2	0.020
RT40	1000	110.0	98.2	2.63	385	3.8	2.2	287	11.0	7.2	0.022
RT41	1000	110.0	97.3	2.25	449	4.5	3.9	306	5.5	5.5	0.018
RT42	1000	110.1	97.2	1.94	504	5.5	6.1	253	3.0	4.2	0.052
RT43	1000	140.1	138.8	3.19	405	2.8	1.6	255	16.6	8.3	0.023
RT44	1000	140.1	140.1	2.44	537	3.8	4.8	232	5.3	6.3	0.017
RT45	1000	139.4	139.5	2.03	607	5.5	7.4	245	2.7	5.8	0.156
RT46	800	124.7	121.7	3.41	291	3.9	0.2	446	35.0	4.3	0.027
RT47	800	124.9	120.4	2.79	419	5.1	1.5	308	7.4	2.1	0.016
RT48	800	125.1	120.2	2.23	535	5.0	4.7	277	2.7	1.2	0.014
RT49	1000	125.0	111.0	3.11	364	3.3	1.0	309	54.7	27.7	0.024
RT50	1000	124.8	109.8	2.47	478	4.7	3.0	252	14.8	19.9	0.019

continued on next page

Test No.	Speed [rpm]	MAP [kPa]	T_{int} [°C]	λ	$\overline{IMEP}$ [kPa]	$\overline{CA5_{HTR}}$ [CAD ATDC]	$\overline{P_{rise}}$ [bar/CAD]	BSFC [g/kWhr]	BSCO [g/kWhr]	BSUHC [g/kWhr]	BSNOx [g/kWhr]
RT51	1000	124.9	108.9	1.98	577	6.0	6.2	245	5.3	14.0	0.159
RT52	1200	125.3	90.3	2.60	444	6.6	1.2	282	30.4	25.1	0.021
RT53	1200	125.1	91.5	2.35	496	6.8	2.2	273	15.4	19.5	0.019
RT54	1200	125.3	92.1	2.03	571	7.7	3.9	249	8.2	15.0	0.021
RT55	1000	109.7	100.5	2.63	380	3.7	2.2	288	21.9	22.2	0.023
RT56	1000	109.4	98.5	2.39	420	4.5	2.9	330	14.4	19.7	0.020
RT57	1000	109.5	97.9	1.95	501	5.7	5.6	258	5.8	13.9	0.100
RT58	1000	140.0	140.4	3.29	360	4.0	0.6	294	77.8	36.4	0.028
RT59	1000	139.9	139.1	2.51	513	5.1	3.1	241	13.5	24.3	0.019
RT60	1000	140.1	139.2	2.07	605	6.0	6.2	241	6.2	16.3	0.063

A.4 HCCI Transient Results

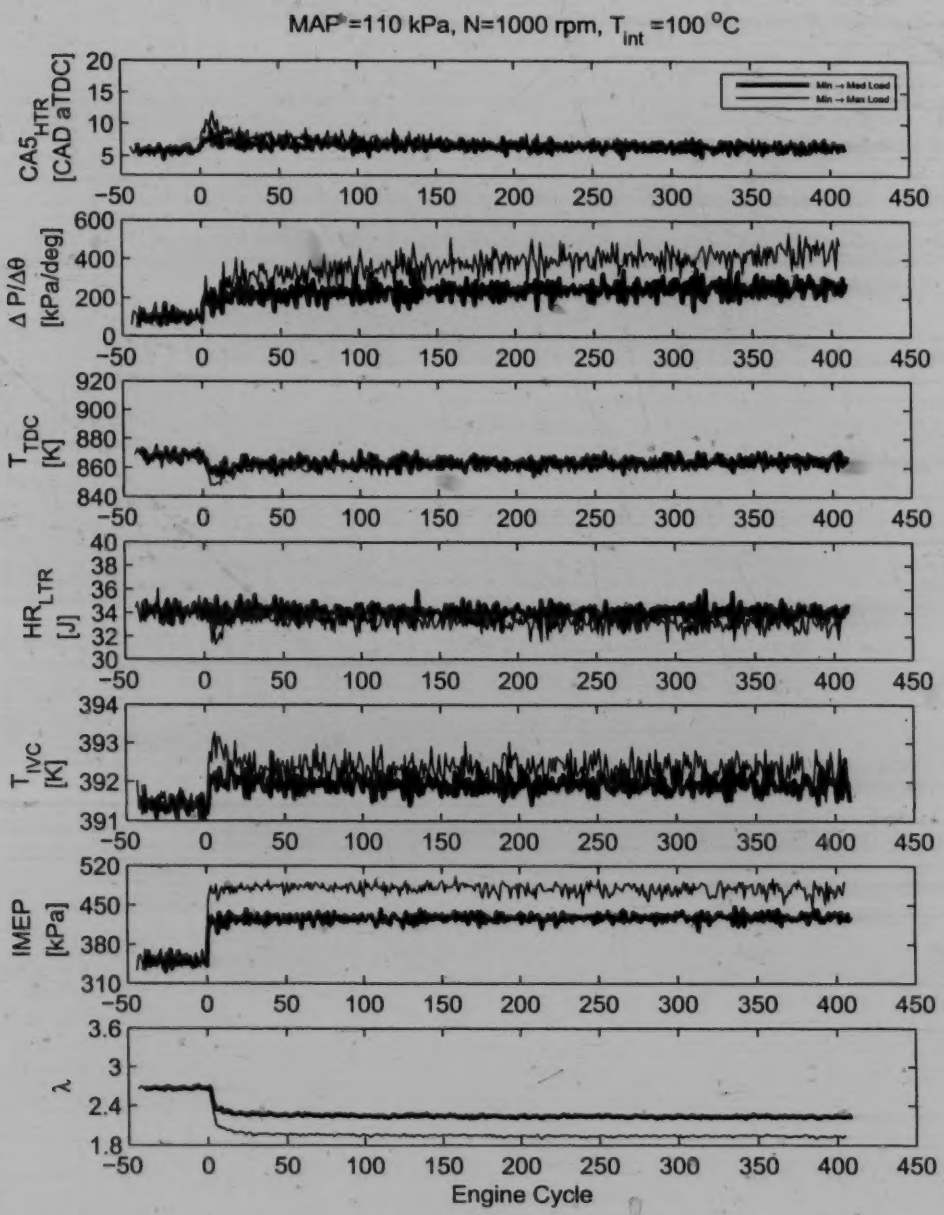

Figure A.1: Combustion Metrics Through a Step Load Transient. Tests TR17 and TR18.

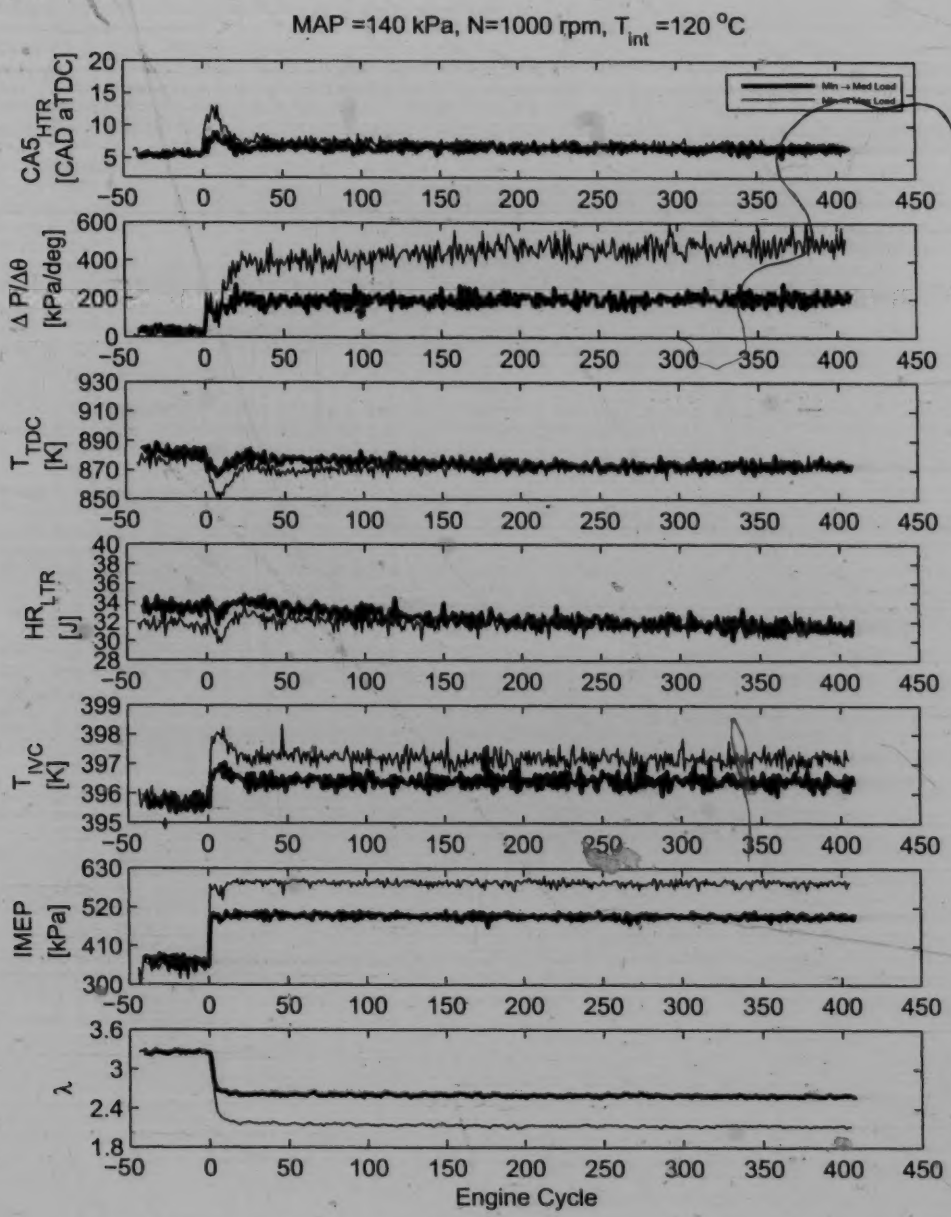

Figure A.2: Combustion Metrics Through a Step Load Transient. Tests TR49 and TR50.

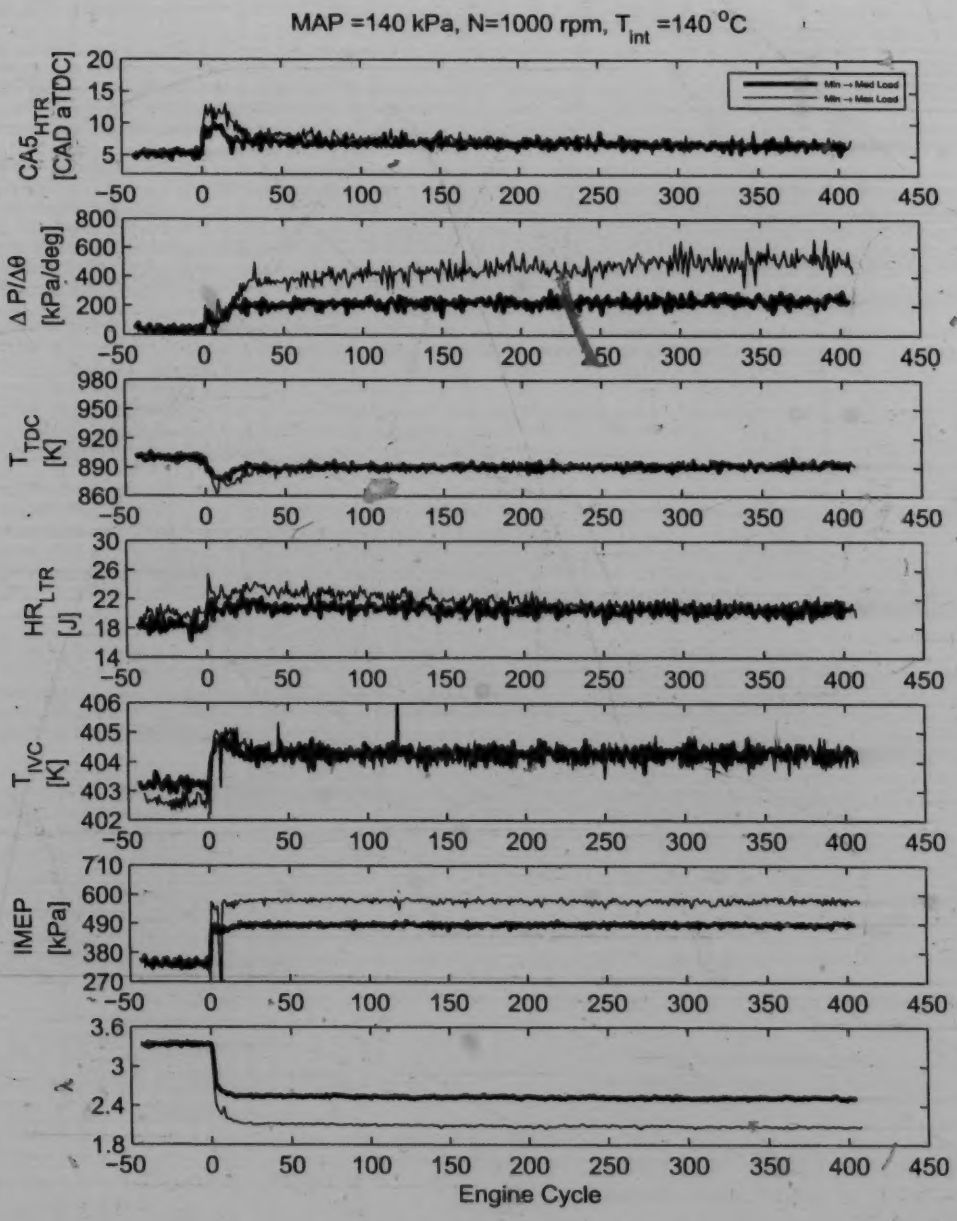

Figure A.3: Combustion Metrics Through a Step Load Transient. Tests TR57 andTR58.

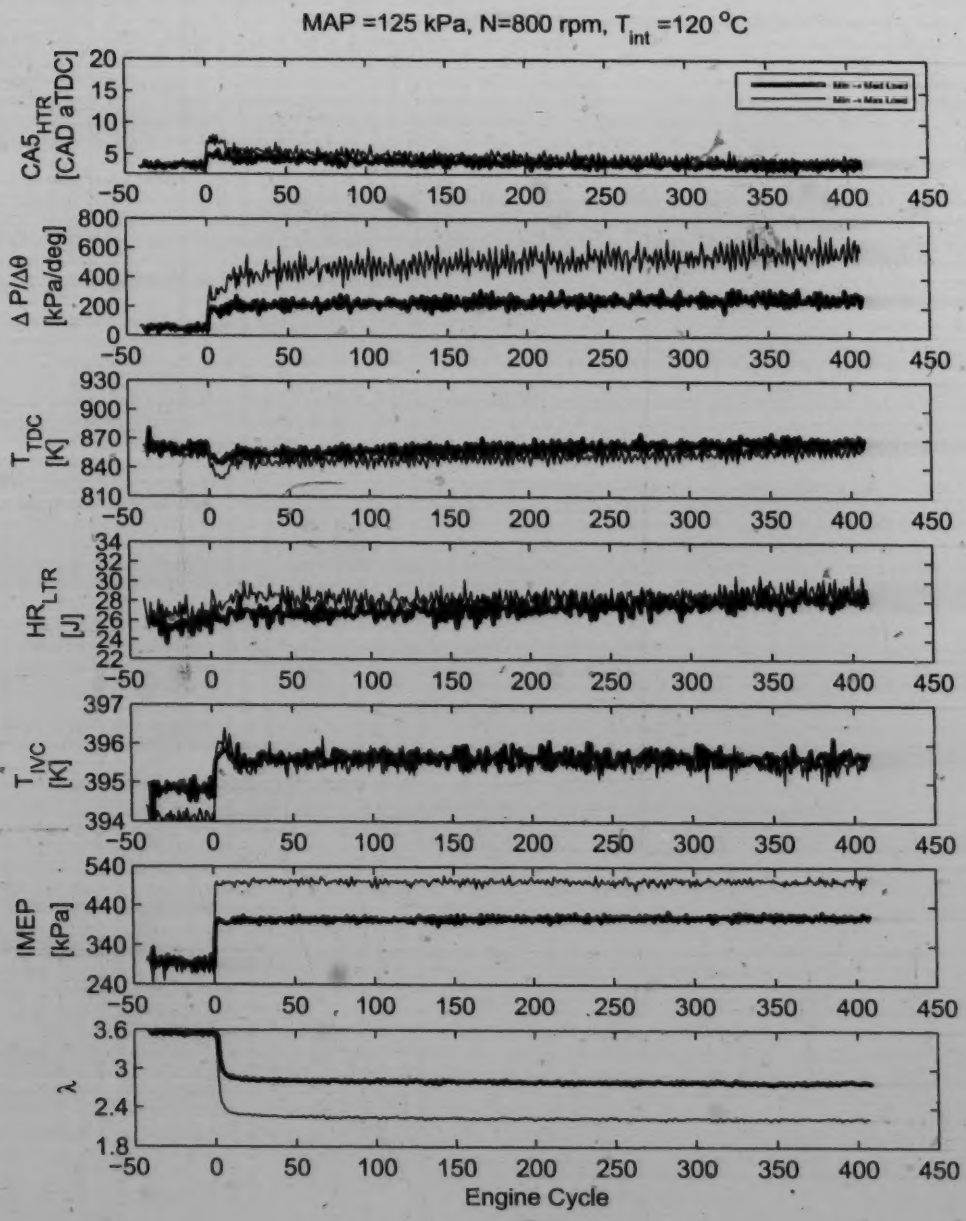

Figure A.4: Combustion Metrics Through a Step Load Transient. Tests TR77 and TR78.

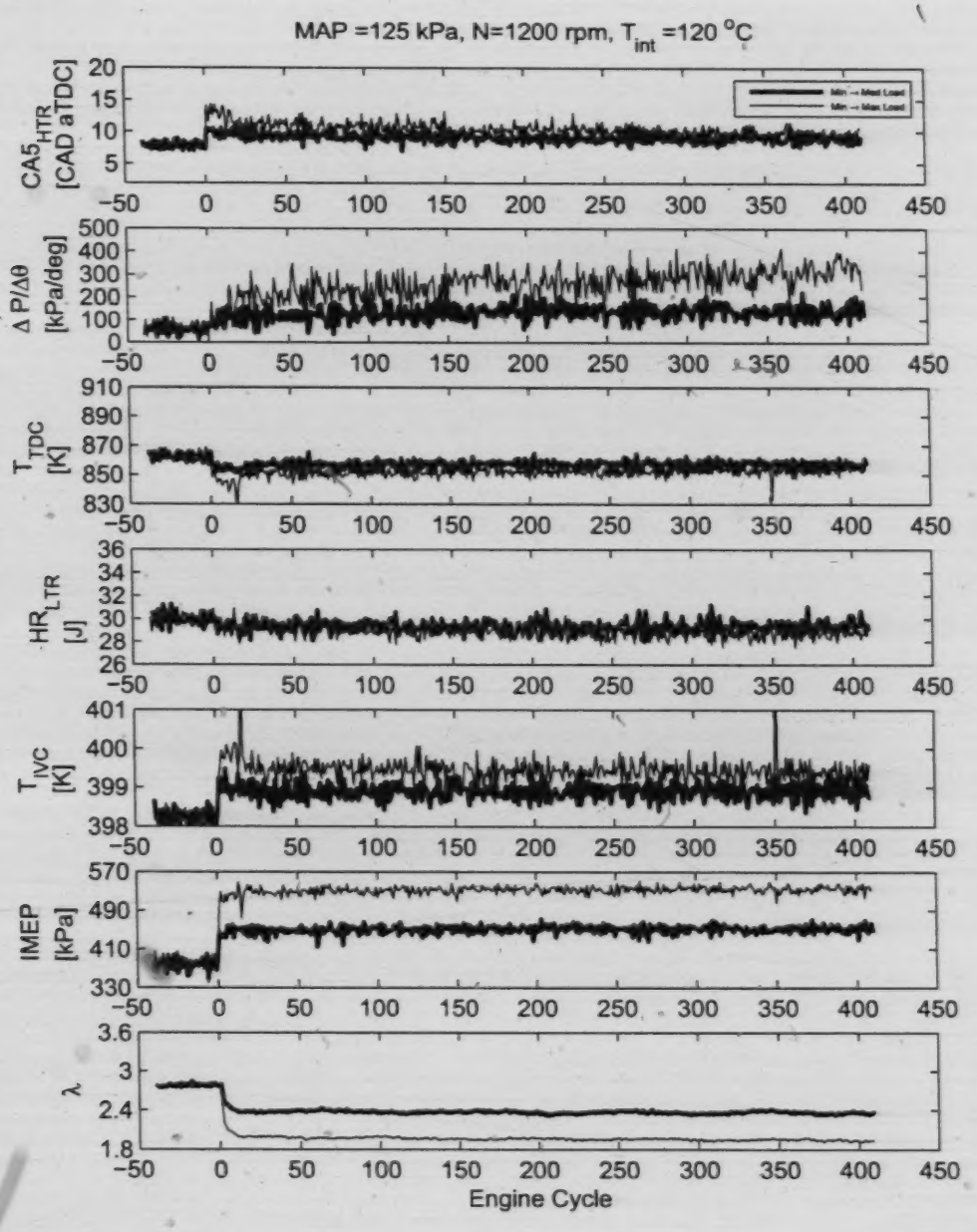

Figure A.5: Combustion Metrics Through a Step Load Transient. Tests TR93 and TR94.

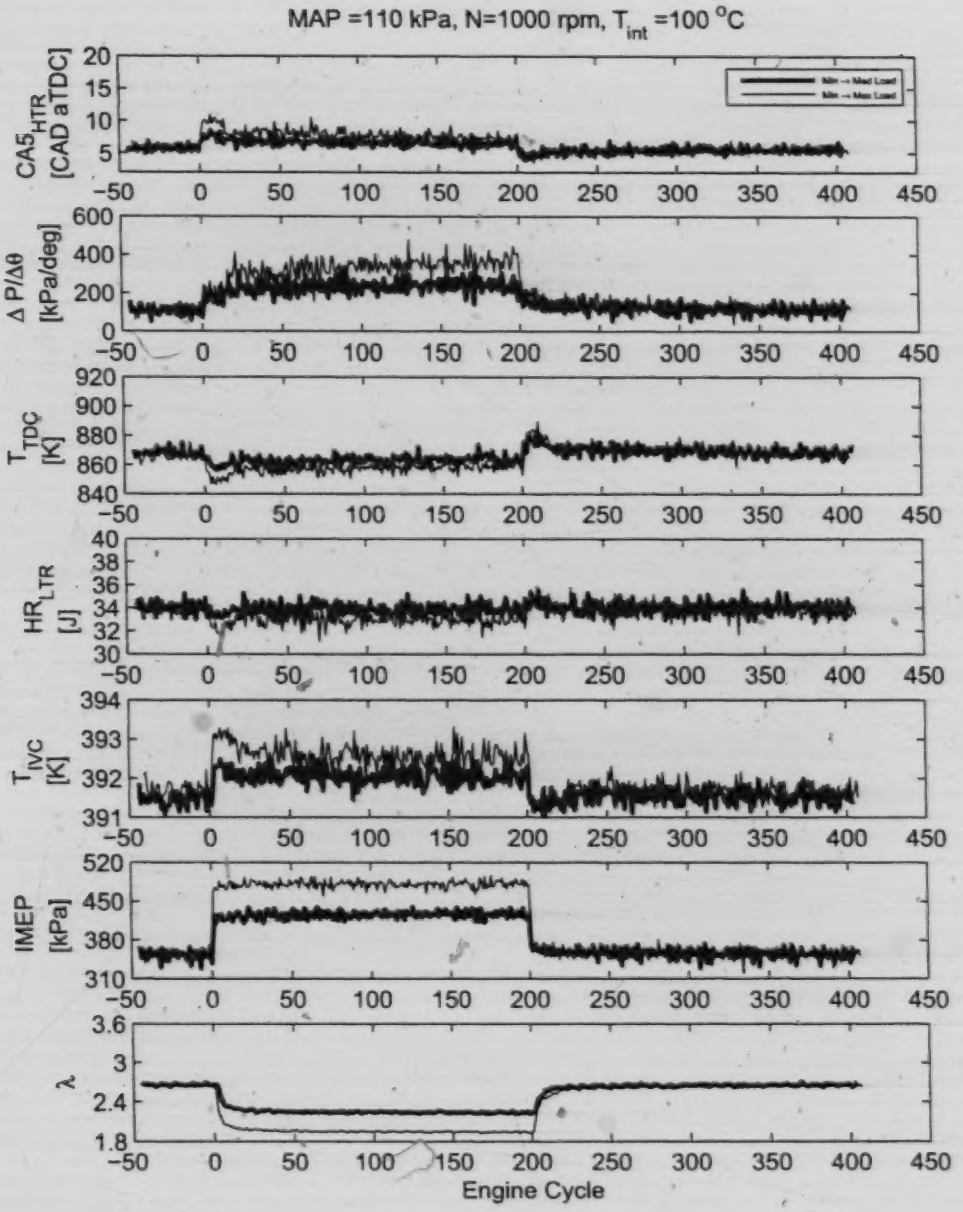

Figure A.6: Combustion Metrics Through a Pulse Load Transient. Tests TR19 and TR20.

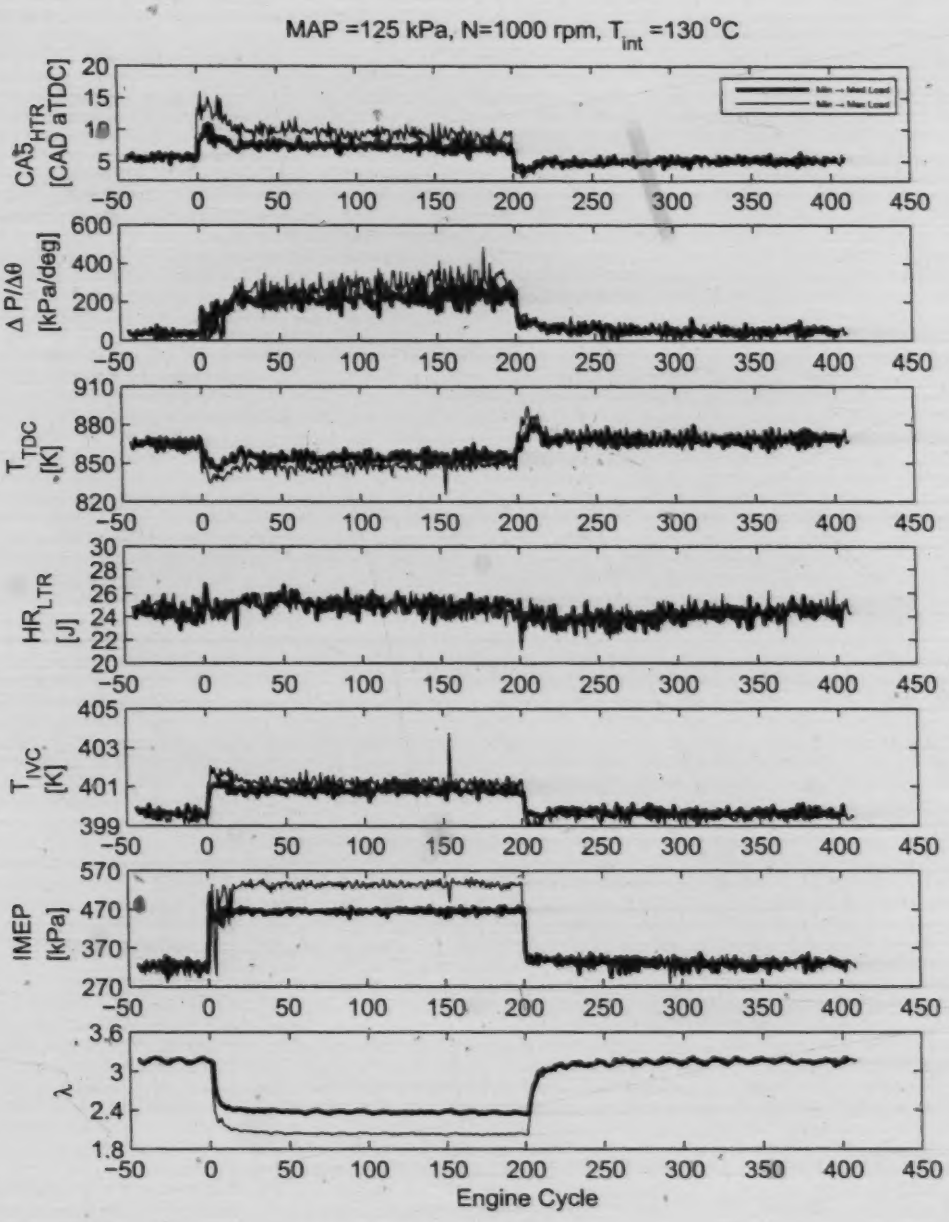

Figure A.7: Combustion Metrics Through a Pulse Load Transient. Tests TR39 and TR40.

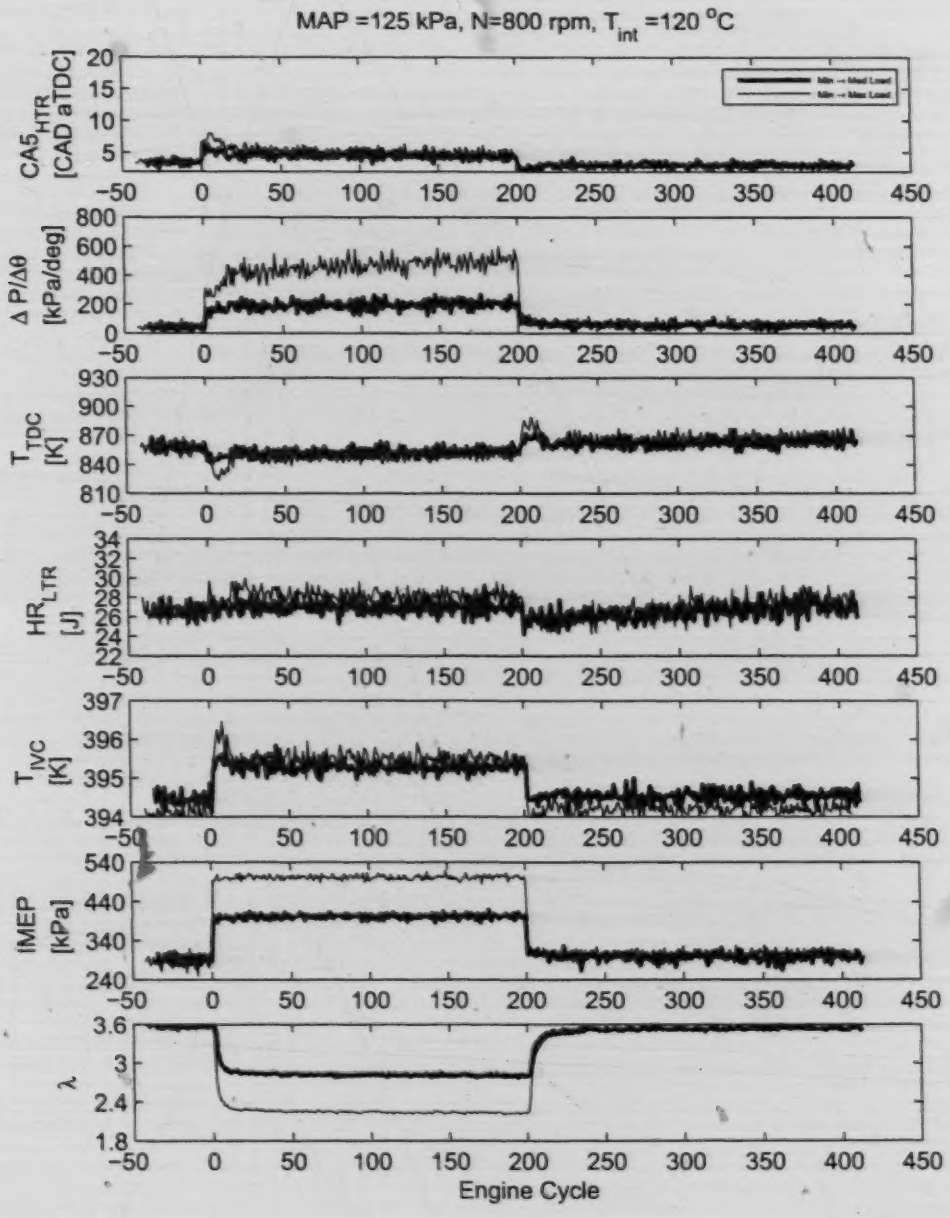

Figure A.8: Combustion Metrics Through a Pulse Load Transient. Tests TR89 and TR90.

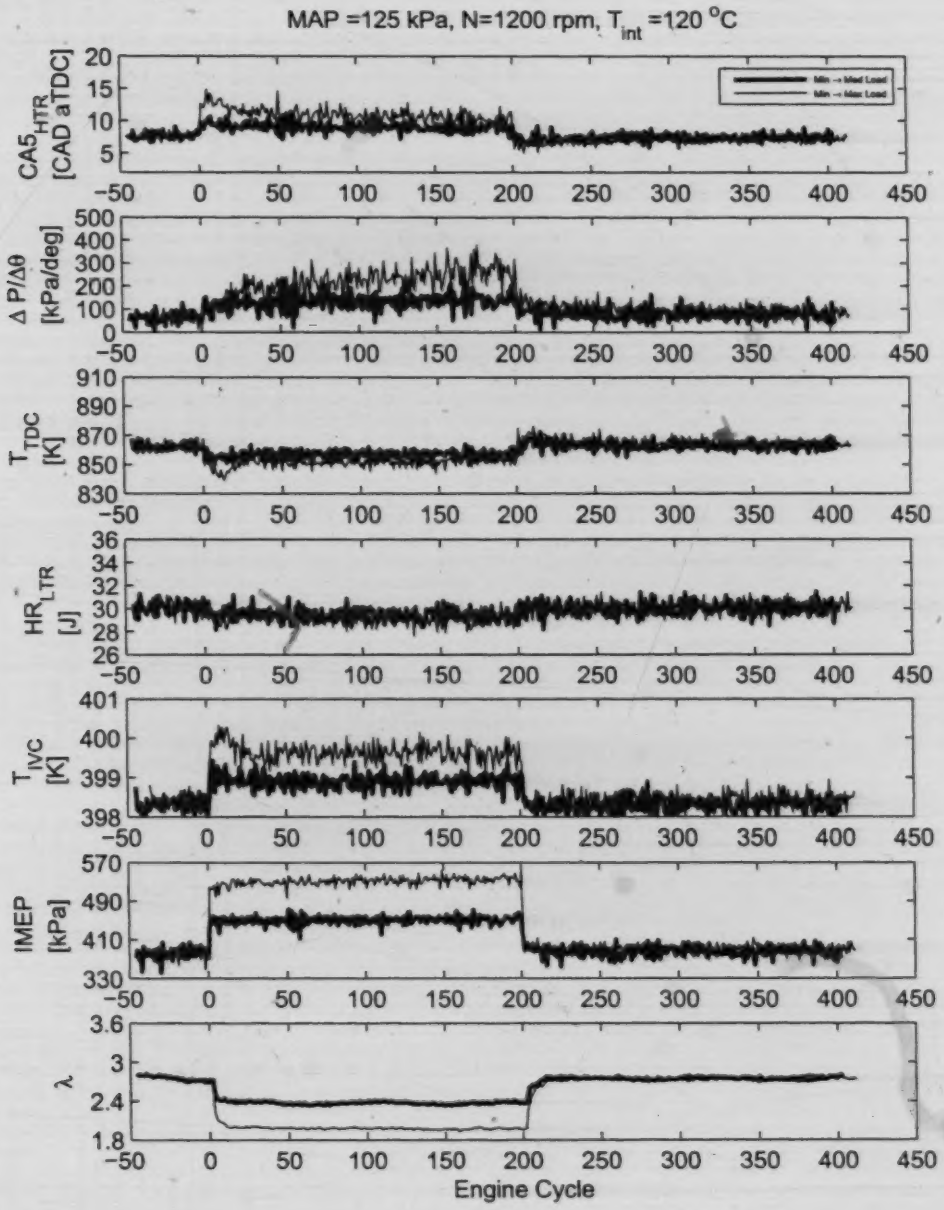

Figure A.9: Combustion Metrics Through a Pulse Load Transient. Tests TR95 and TR96.

A.5 Spark Ignition Experimental Data

To form a basis of comparison, the Ricardo engine was run in SI mode in order to determine the performance characteristics of SI compared with HCCI combustion modes. A map of test points for the SI tests is shown in Table A.4. All SI test points were run with pure iso-octane run as fuel (ON 100). Fueling for all tests was adjusted to be stoichiometric and the spark timing was adjusted to give CA50 of $\sim 8°$ ATDC. One difficulty in running this series of tests, was the high load operating points, at an engine speed of 800rpm. For these cases the engine was knock limited, to where the combustion timing could not be advanced to the desired value, before knock was encountered. These particular tests of the matrix were not run.

Parameter	Operating Condition
Engine Speed [rpm]	800,1000,1200,1400,1600,1800,2000
Intake Manifold Pressure [kPa]	60,70,80,90,100,110,120
Intake Manifold Temperature [$\circ C$]	80,90,100
EGR Rate [%]	0
Coolant Temperature [$\circ C$]	80
Oil Temperature [$\circ C$]	70
Liquid Fuel Temperature [$\circ C$]	$\sim$ 25 to 30

Table A.4: Operating Conditions for Spark Ignition Engine Tests

Test No.	Speed [rpm]	MAP [kPa]	$\overline{IMEP}$ [kPa]	BMEP [kPa]	$\overline{CA50}$ [CAD ATDC]	$\overline{BD}$ [CAD]	BSFC [g/kWhr]	BSCO [g/kWhr]	BSUHC [g/kWhr]	BSNOx [g/kWhr]
SI 1	800	73.0	673	460	9.5	16.2	322	33.1	51.6	11.92
SI 7	1000	66.2	596	436	9.2	17.2	311	36.1	58.3	10.72
SI 8	1000	69.8	635	475	9.4	16.8	302	54.2	76.4	23.52
SI 9	1000	79.6	752	587	9.6	16.6	272	19.4	29.6	10.56
SI10	1000	89.6	866	689	9.8	16.1	272	20.3	27.9	10.27
SI11	1000	99.3	958	773	10.1	15.7	267	27.9	31.7	10.41
SI12	1000	109.6	1065	869	13.2	15.0	269	30.1	38.2	10.07
SI14	1200	60.1	526	376	9.4	18.4	325	12.0	39.8	10.21
SI15	1200	69.9	647	492	9.2	17.8	295	53.7	72.2	23.21
SI16	1200	79.9	761	600	9.1	17.3	278	45.5	30.5	10.24
SI17	1200	89.6	861	690	9.3	17.0	274	28.6	26.5	9.92
SI18	1200	99.2	975	798	9.7	17.0	268	26.4	24.3	9.88
SI19	1200	109.3	1097	909	10.1	15.4	259	17.5	34.3	9.71
SI20	1200	120.1	1185	997	14.1	15.7	257	15.9	27.9	9.39
SI21	1400	59.8	528	373	9.4	19.4	325	42.8	31.6	9.76
SI22	1400	69.4	649	491	9.0	18.6	295	57.7	67.2	23.12
SI23	1400	80.0	774	611	9.5	18.6	277	18.2	27.8	10.69
SI24	1400	89.6	890	719	9.1	18.2	264	17.1	24.7	10.08
SI25	1400	99.0	1001	816	9.2	18.2	258	22.8	23.6	9.78
SI26	1400	109.5	1130	940	9.7	16.9	250	19.2	23.0	9.25
SI27	1400	119.2	1201	1014	14.9	18.2	252	24.8	25.4	9.39
SI28	1600	59.8	544	386	9.2	20.1	320	13.2	24.6	9.57
SI29	1600	68.5	648	487	9.1	19.4	293	43.8	64.0	23.38
SI30	1600	80.4	780	613	9.5	18.8	274	18.7	24.8	9.89
SI31	1600	89.5	890	717	9.5	18.4	264	23.2	25.9	10.37

continued on next page

Test No.	Speed [rpm]	MAP [kPa]	$\overline{IMEP}$ [kPa]	BMEP [kPa]	$\overline{CA50}$ [CAD ATDC]	$\overline{BD}$ [CAD]	BSFC [g/kWhr]	CO [g/kWhr]	UHC [g/kWhr]	NOx [g/kWhr]
SI32	1600	99.4	1021	836	9.2	18.4	256	26.9	23.0	9.94
SI33	1600	109.9	1149	955	9.2	17.5	249	23.1	20.4	9.22
SI34	1600	119.5	1238	1037	10.9	16.6	247	26.4	22.0	9.27
SI35	1800	61.0	544	385	9.4	21.1	319	23.8	25.4	9.26
SI36	1800	70.1	666	501	9.3	20.3	291	51.4	69.3	25.24
SI37	1800	79.8	770	594	9.0	19.4	276	17.4	25.9	10.94
SI38	1800	88.6	886	705	9.0	18.9	265	25.2	23.9	10.17
SI39	1800	100.6	1039	848	9.1	18.6	253	24.3	21.4	9.51
SI40	1800	110.2	1150	950	9.3	18.6	249	24.6	20.7	9.25
SI41	1800	120.0	1254	1054	11.5	18.6	246	28.2	20.1	9.13
SI42	2000	59.6	525	365	9.4	21.4	326	22.6	22.6	9.03
SI43	2000	71.2	685	508	9.7	20.7	293	17.4	25.9	10.93
SI44	2000	80.2	803	623	9.6	19.9	275	25.2	23.9	10.16
SI45	2000	90.6	936	743	9.2	19.4	263	24.3	21.4	9.50
SI46	2000	100.1	1059	859	9.3	19.2	254	24.6	20.7	9.24
SI47	2000	110.6	1176	965	9.5	18.9	250	28.2	20.1	9.13
SI48	2000	121.2	1280	1065	10.5	18.5	245	22.6	22.6	9.02

Appendix B

Experimental Equipment Setup

B.1 Emissions Calculations

Engine out exhaust is sampled by the emissions bench to determine the concentrations of the 5 analyzed gases in the exhaust. After being sampled in the engine exhaust pipe, the sample is cooled in a room temperature water bath, and the water separated using an erlenmeyer flask. The water is removed to prevent damage to the emissions analyzers from condensing water as the sample cools. To determine the engine out emissions, the values measured at the emissions analyzers are used, with corrections made for the water removed from the sample. Here the same technique shown by Atkins is used [Atkins, 2004] . The analysis of the exhaust emissions is done with the following goals and assumptions:

- Correct 'dry' emissions measurements to engine out, 'wet' measurments
- Account for absolute humidity present in the air
- Assume sample gas after cooler is water saturated at the temperature of the cooler
- Assume all NO_x is measured as NO, and UHC is measured as CH_4
- Assume negligible hydrogen present in exhaust sample

- Assumes the fuel hydrogen:carbon ratio is the same in the reactants and products of combustion

The basic unbalanced combustion equation can be written as shown in Eqn. B.1.

$$C_xH_y + \underline{n}(O_2 + \underline{A}N_2 + \underline{B}CO_2 + \underline{C \cdot Habs}H_2O) \rightarrow$$
$$\underline{a}CO_2 + \underline{b}CO + \underline{d}H_2O + \underline{e}O_2 + \underline{f}N_2 + \underline{g}NO_x + \underline{h}C_{x'}H_{y'} \quad \text{(B.1)}$$

Where the constants A, B, C, and H_{abs} are defined as follows, with the square brackets, '[ ]', indicating volume concentration:

$$A = \frac{[N_2]_{amb}}{[O_2]_{amb}} \approx 3.774 \qquad B = \frac{[CO_2]_{amb}}{[O_2]_{amb}} \approx 1.8 \cdot 10^{-3}$$
$$H_{abs} = \frac{n_{H_2O} \cdot 18.016}{n_{air} \cdot 28.96} \cdot 10^3 \qquad C = \frac{1.6076 \cdot 10^{-3} H_{abs}}{[O_2]_{amb}} \quad \text{(B.2)}$$

By using the known values of a, b, e, g, h as measured by the emissions analyzers, and balancing the combustion equation for carbon, hydrogen, oxygen, as well as an overall mole balance, the unknown quantity of water in the 'wet' exhaust can be determined. Balancing these equations also allow the value of λ to be determined. To compare the measurements of the emissions bench with the measurements made by the UEGO in the exhaust, the calculated values of λ for both the emissions bench and the UEGO are compared. The results of this comparison for all of the steady state HCCI data points are shown in Figure B.1. A linear fit to the data is also shown. The average residual of λ of the linear fit is 0.029, and the maximum residual is 0.16.

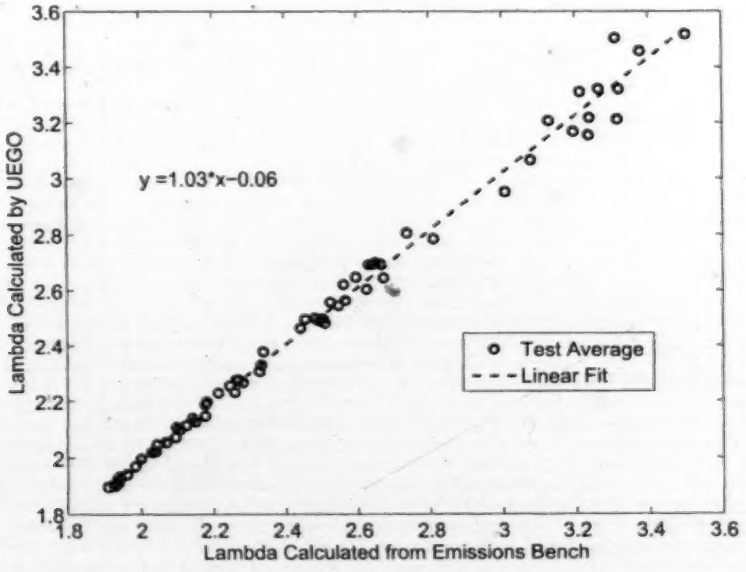

Figure B.1: Comparison of Lambda Calculated by UEGO and by Emissions Bench

B.2 Equipment Calibration

B.2.1 Determining TDC Offset

An accurate method to determine the relative offset of the crankshaft encoder with respect to the location of TDC is required for the in-cylinder pressure measurement analysis. To measure actual piston position, the spark plug is removed, and a 1/8" steel rod is slid down into the cylinder, so it rests on the piston top. An LVDT displacement transducer is fixed to the engine valve cover, to measure the relative location of the steel rod. An oscilloscope is used to measure the signals produced by the LVDT displacement transducer, as well as the 1 pulse/rev, and 3600 pulse/rev outputs of the crankshaft encoder. The engine is then motored for a few revolutions, with the oscilloscope set to capture the three measured signals. Figure B.2 shows the signals of the 1pulse/rev signal, and the measured LVDT signal after re-sampling the

LVDT signal at the locations of the rising edges of the 3600pulse/rev signal. This re-sampling transforms the LVDT signal from the time domain to the crankshaft angle domain. The 3600pulse/rev signal is left out for clarity, although it is a similar square wave signal to the 1pulse/rev signal.

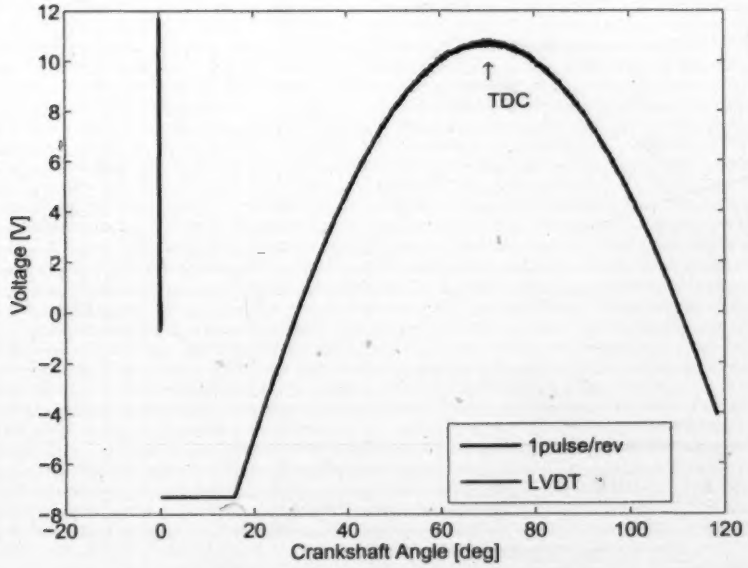

Figure B.2: Raw Data Collected from Oscilloscope from Motored Engine

To determine the location of TDC, the raw encoder signals are processed to determine the number of rising edges of the 3600pulse/rev signal, between the 1pulse/rev signal, and the measured location of TDC. A rising edge of the 3600pulse/rev signal is determined by a threshold value. To determine TDC from the LVDT measurement, several methods have been tested with similar results. In particular, finding the location where the first derivative of the LVDT signal crosses zero, is used to find the maximum LVDT signal (and thus where the piston is at TDC). Another method used to is find TDC, is by finding points of constant voltage of the LVDT signal, for ascending and descending piston motion. The midpoint between these two values

will also be TDC. Finally by taking a polynomial fit of the LVDT data, and finding the location of the maximum value of this function, TDC can be determined. For all of these methods, for the case shown here TDC is determined to be at 69.9deg, as shown in Figure B.2 to within 0.04deg of each other (this value is interpolated as the resolution of the encoder is 0.1deg).

B.2.2 Fuel Injector Flow Rate Calibration

The mass of fuel injected per engine cycle is determined by the pulse width the injector is activated for. To calibrate the iso-octane fuel injector a series of tests were run with the Pierburg fuel flow measurement system measuring the iso-octane fuel delivery. The mass of fuel injected per cycle is calculated using the fuel flow, and the engine speed with the engine at steady state. The results of this calibration is shown in Figure B.3. Also in Figure B.3 is a linear fit to the data. The equation of the linear fit can be used to determine the necessary PW required to deliver a desired quantity of fuel. The equation can also be inverted to give the injected fuel mass for a given PW. For the smallest PW_{octane} in Figure B.3 of 1.15msec, a distinct deviation from the linear trend can be seen. For slightly larger PW_{octane} of 1.3msec, the data point lies nearly on the linear fit line. Since the fuel injector becomes non-linear at small PW's the minimum value (that which is greater than zero) is taken as 1.3msec. For a PW smaller than this results in unpredictable behavior of the actual injected fuel mass. For the n-heptane injector, the $PW_{heptane}$ required to deliver a given fuel mass is shown in Figure B.4. The data shown in this plot is from the steady state HCCI operating points.

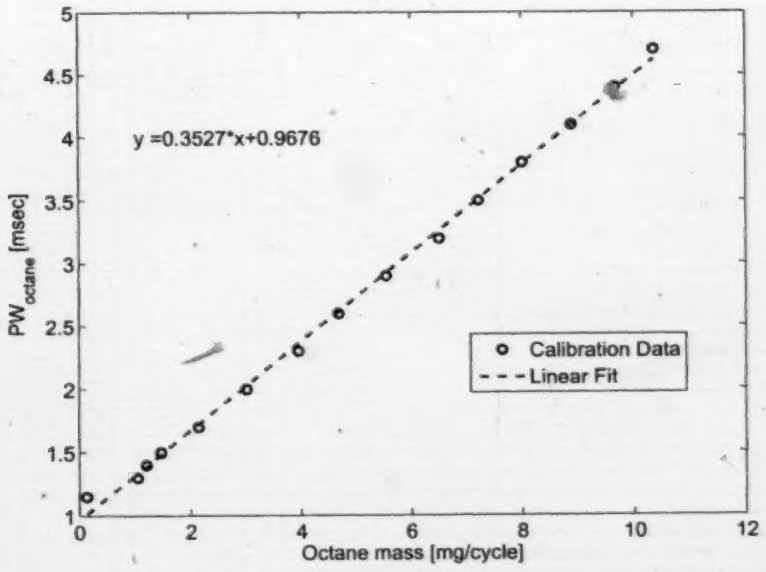

Figure B.3: Octane Fuel Injector Pulse Width vs. Injected Octane Mass per Cycle

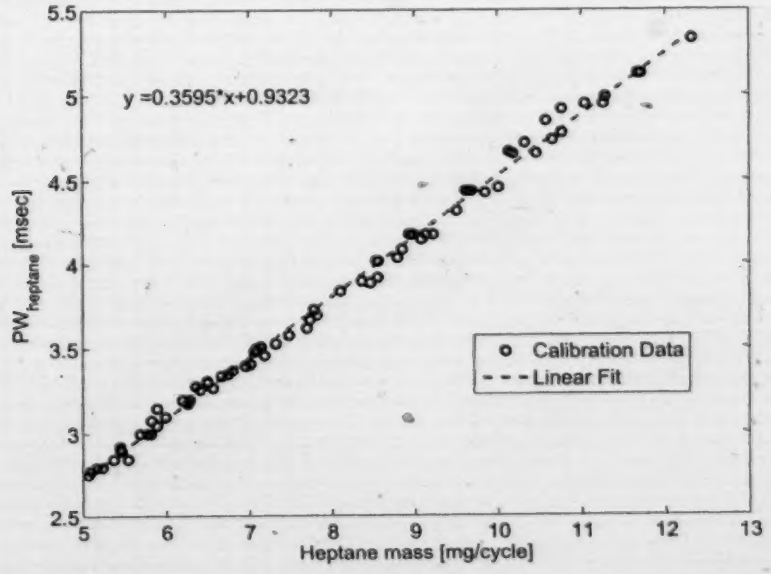

Figure B.4: Heptane Fuel Injector Pulse Width vs. Injected Heptane Mass per Cycle

B.2.3 Laminar Air Flow Meter Calibration

Measurement of the air flow rate into the engine is done with a Cussons laminar air flow element. A calibration of this element was performed by Labcal Ltd using methods traceable to national standards. The results of the calibration are shown in Figure B.5. with the air volume flow rate plotted against the differential pressure across the flow element. Labcal estimates the uncertainty of the measured differential pressure across the flow element at $\pm 0.47\% + 0.012$in of H_2O. A linear fit to the data is also shown in Figure B.5, as in the laminar flow regime the pressure drop across the element is proportional to the flow rate. The error in the linear fit compared with the actual data, as a function of the differential pressure across the flow element is shown in Figure B.6.

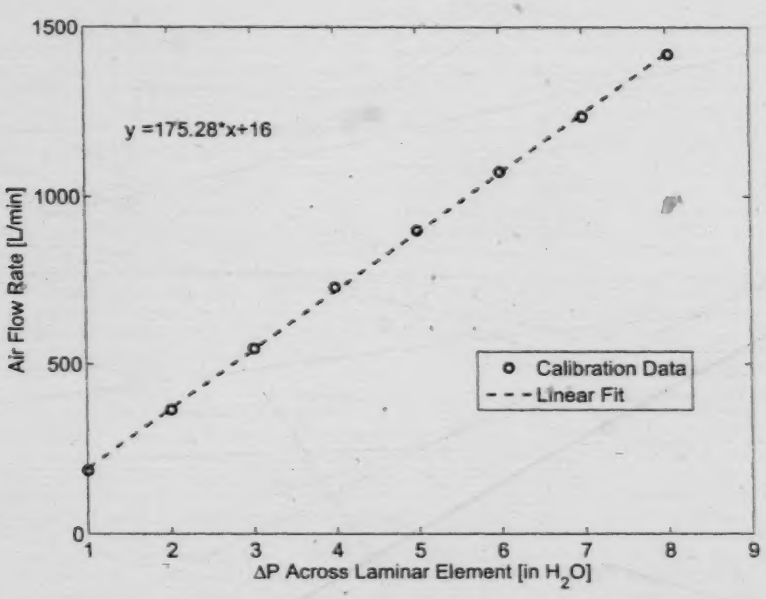

Figure B.5: Air Volume Flow Rate vs. Differential Pressure Across Laminar Flow Element

To measure the differential pressure across the laminar flow element in the engine

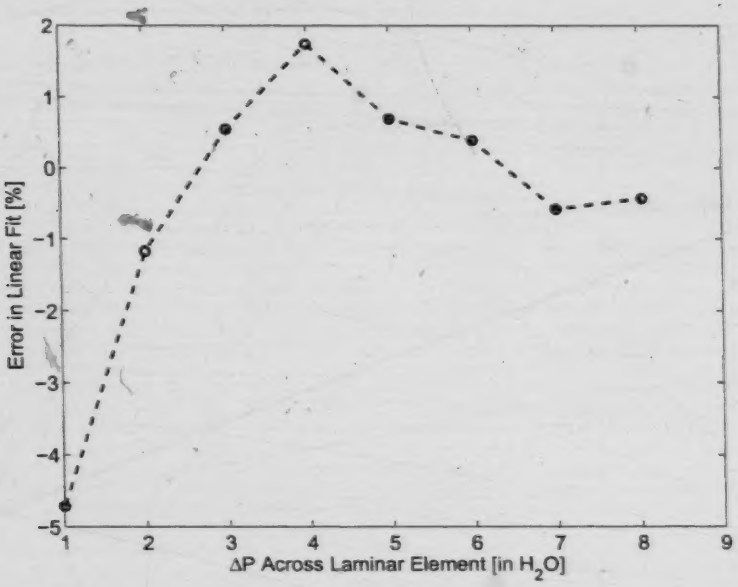

Figure B.6: Error in Linear Fit of Volume Flow Rate Compared with Actual Data vs. Differential Pressure

test cell, a Validyne P305D pressure transducer is used. The Validyne transducer is calibrated in zero and span with a micromanometer with a resolution of 0.001".

B.3 Data Collection and Analysis Programs

This section gives a list of computer programs used in data collection and analysis of the data. The files and programs used in the Baseline ADAPT DAC, Baseline CAS, and MicroAutobox are listed together, as they are necessary to run the engine. Programs used for data analysis, post-processing and plotting are listed together. Screen shots of the software files are also shown. Examples of the signals measured by the data acquisition system are also shown for values of λ, MAP, and in-cylinder pressure.

B.3.1 Baseline ADAPT, Baseline CAS, and MicroAutobox Programs

File Name	System	Description
test_aug23_07.tst	ADAPT	File loaded onto Baseline ADAPT RTP
Single Cylinder4.ini	ADAPT	Layout screen for ADAPT software
cas.CASConfiguration.xml	CAS	Configuration file for both CAS RTP and layout screen for PC
ricardo.mdl	dSpace	Simulink file to generate .sdf file to use on MicroAutobox
ricardo.sdf	dSpace	Real time application compiled from Simulink model
Ricardo Experiment.cdx	dSpace	Experiment file for dSpace Controldesk includes PC layout

Table B.1: PC and RTP Files for Running Engine and Collecting Data

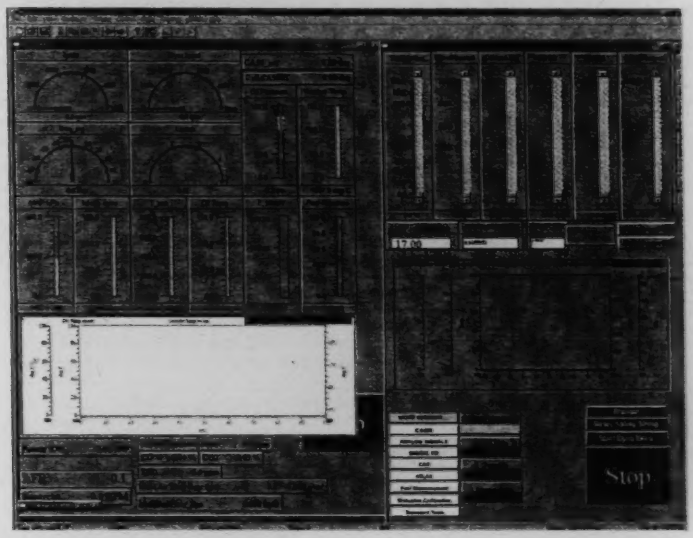

Figure B.7: Screenshot of the ADAPT Software Layout

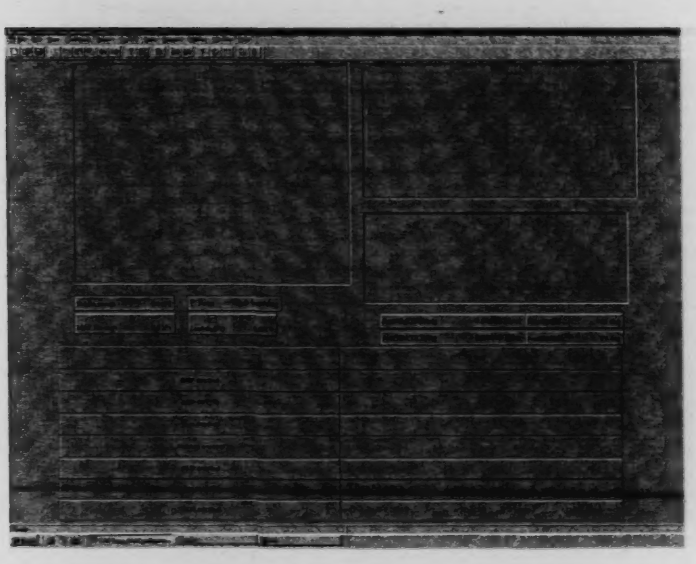

Figure B.8: Screenshot of the CAS Software Layout

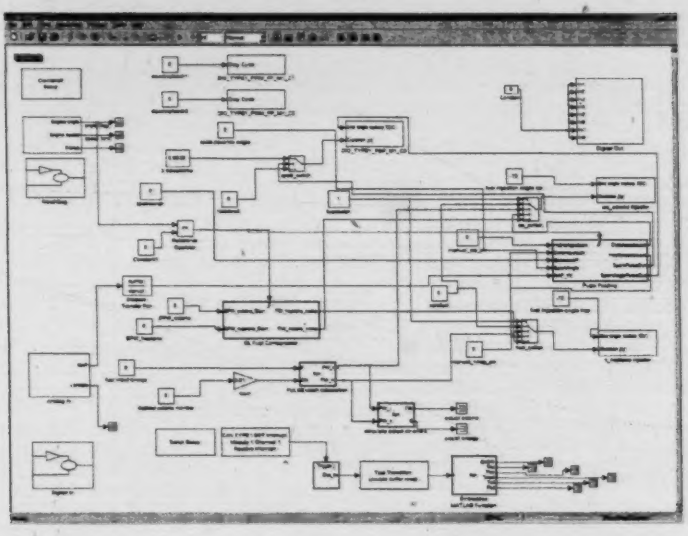

Figure B.9: Screenshot of Simulink Block Diagram of ECU Software

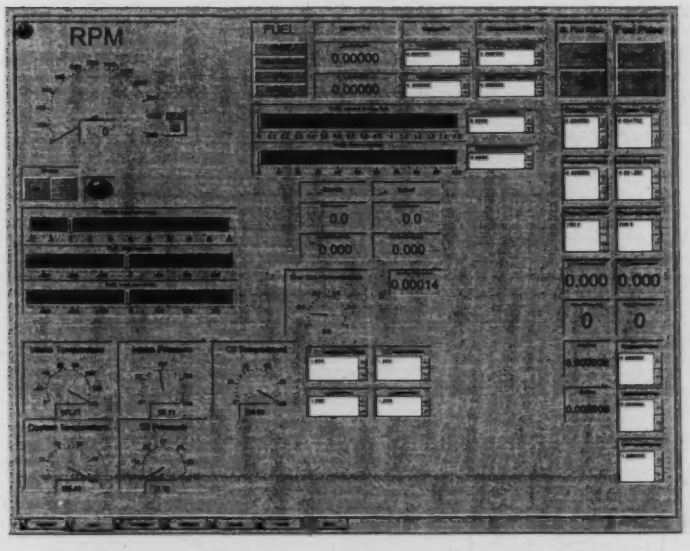

Figure B.10: Screenshot of the dSpace Controldesk Layout

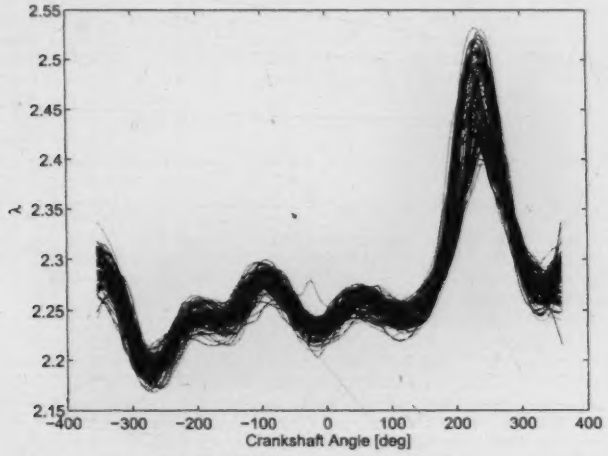

Figure B.11: Measured Value of λ vs. Crankshaft Angle for 450 cycles. Test SS54

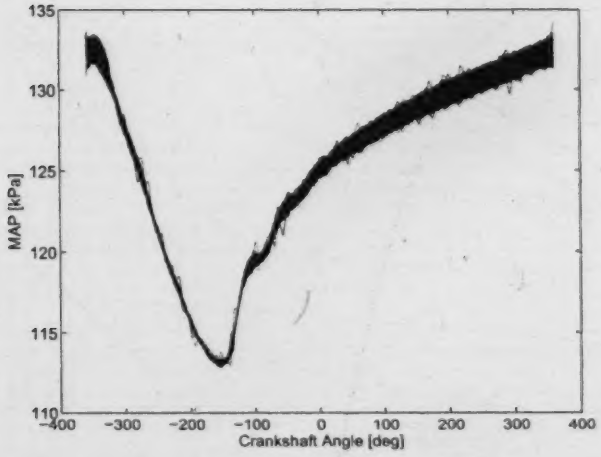

Figure B.12: Measured Value of MAP vs. Crankshaft Angle for 450 cycles. Test SS54

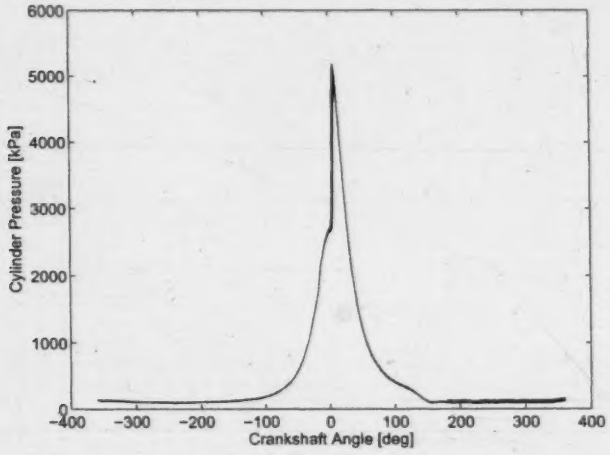

Figure B.13: Measured Value of In-cylinder Pressure vs. Crankshaft Angle for 450 cycles. Test SS54

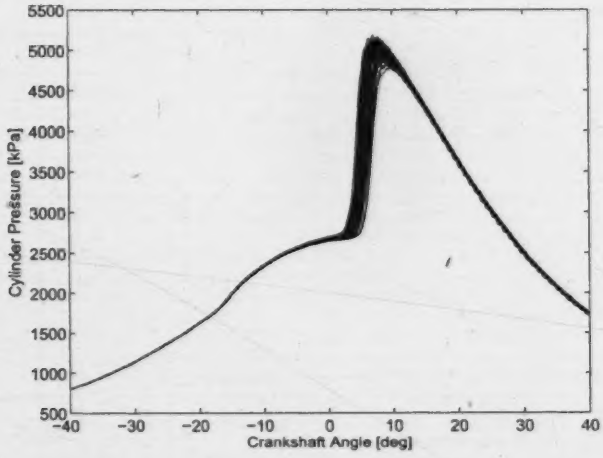

Figure B.14: Measured Value of In-cylinder Pressure near combustion vs. Crankshaft Angle for 450 cycles. Test SS54

B.3.2 Data Analysis Programs

File Name	Function	Description
AdaptDataRead3.m	Data formatting	Format ADAPT .csv files into Matlab
cyclesim10_mat	Post-processing	Determine cycle based parameters
SSTableMake.m	Data Summary	Summarize average data for HCCI tests
SITableMake.m	Data Summary	Summarize average data for SI tests
GeneralPlots.m	Plotting	Generates several misc. plots
KnockPlots.m	Plotting	Generates knock related plots
HRPlots.m	Plotting	Generates heat release related plots
EmissionsPlots.m	Plotting	Generates emissions plots
CombTimPlots.m	Plotting	Generates plots for comb. timing tests
TransientPlotting.m	Plotting	Generates plots of transient tests
ModeSwithPlots.m	Plotting	Generates plots of mode switching tests
Calibrations.m	Plotting	Generates plots for calibrations
Trials.m	Data Summary	Summarizes results of repeated trials

Table B.2: Matlab Files for Post Processing Data and Generating Plots

B.4 List of Equipment Used

Item	Make / Model	Relevant Specifications
Laminar Flow Element	Cusson's Technology P7200/108	Range: 0-1500 L/min Output: 0-8 inH_2O
Laminar Flow Pressure Transducer	Validyne P305D	Range: 0-0.5 psig Output: 0-5 V Accuracy: ±0.25%
Intake Manifold Pressure	Setra 280E	Range: 0-50 psia Output: 0-5 V Accuracy: ±0.11 % FS
Knock Sensor	Bosch A261 230 260	Frequency Range: 3-10 kHz Sensitivity: 40 mV/g Resonance Freq.: >25 kHz Engine block accelerometer
Cranshaft Encoder	BEI Industries XH25D-SS-3600-T2-ABZC-7272-SM18	Outputs: ABZ @5 V A/B-3600 pulses/rev Z-1 pulse/rev
Wideband oxygen sensor	ECM Inc. AFRecorder 1200	Range: 0.4-10 λ Output: 0-5 V Accuracy: ±0.9% Response Time: <150 ms
Cylinder Pressure Transducer	Kistler 6043A60	Range: 0-250 bar Sensitivity: 20 pC/bar Linearity: <+/-0.5 % FSO Natural Frequency: ~70 kHz
Charge Amplifier	MTS Powertrain 1108	Amplifies electrical charge of cylinder pressure transducer to high impedance analog output
Combustion Analysis System (CAS)	Baseline CAS	Crank angle based data acquisition system
Dynamometer load cell	Interface Inc. SSM-AJ-200N	Range: 0-200 N Linearity: < ±0.05 % FSO 12 V supply, full bridge output
Camshaft Position Sensor	MG Rover NSC-100-612	Supply: 12 V Hall effect sensor
Crankshaft Position Sensor	Siemens PA66-GF20	Supply: 12 V Hall effect sensor

continued on next page

Item	Make / Model	Relevant Specifications
ADAPT Data Aqcuisition	MTS Powertrain Baseline ADAPT DAC	Main data logging processor with analog and digital I/O and built in thermocouple amplifiers.
Dynamometer AC Motor Drive	Eurotherm Drives 590+	Controller for dynamometer motor to maintain constant engine speed

Table B.3: Instrumentation List

Purpose	Manufacturer and Model	Specifications
Engine Control Unit (ECU) Processor	dSpace MicroAutobox 1401/1501	Simulink models complied to run in real time
ECU Power electronics	custom electronics	Power drivers for fuel injectors and ignition. Hitachi North America design Power: 12V $\sim$ 1A
Intake Air Heater	Omega 4020600T	600W electrical heater Power: 240V
Supercharger	Eaton Automotive MP45	Speed range: 0-16000rpm Discharge pressure: < 15psig
Supercharge drive motor	WER Industrial 21900420F01	Brake Power: 10hp Max Speed: 1750rpm Variable speed DC motor
Fuel injectors	Bosch 0-0280-155-844	Flow rate: 18lbs/hr @ 45psig
Throttle	Woodward Flo-Tech ITB 8235-132	Supply: 9-32Vdc Bore size: 33mm Input: 500-2000Hz PWM Drive by wire butterfly throttle

Table B.4: Equipment List